

EFFECTS OF SUBSTRATE TEMPERATURE, ANNEALING  
TEMPERATURE AND CARBON DOPING ON SURFACE  
MORPHOLOGICAL, WETTING AND MECHANICAL PROPERTIES OF  
IRON DISILICIDE FILMS



A THESIS SUBMITTED IN PARTIAL FULFILLMENT OF THE REQUIREMENT FOR THE  
DEGREE OF DOCTOR OF PHILOSOPHY IN APPLIED PHYSICS  
DEPARTMENT OF PHYSICS SCHOOL OF SCIENCE  
KING MONGKUT'S INSTITUTE OF TECHNOLOGY LADKRABANG

2021

This material is reserved for educational use only. It is not allowed for commercial use.  
Forbidden to modify the content, and cite the document when use.

KMITL-2021-SC-D-030-041



COPYRIGHT 2021

SCHOOL OF SCIENCE

This material is reserved for educational use only, not allowed for commercial use.  
KING MONGKUT'S INSTITUTE OF TECHNOLOGY LADKRABANG  
Forbidden to modify the content, and cite the document when use.

Thesis Title	Effects of Substrate Temperature, Annealing Temperature and Carbon Doping on Surface Morphological, Wetting and Mechanical Properties of Iron Disilicide Films
Student Name	Mr. Peerasil Charoenyuenyao
Student ID	61605016
Degree	Doctor of Philosophy (Applied Physics)
Department	Physics
Year	2021
Thesis Advisor	Asst.Prof.Dr. Nathaporn Promros

### Abstract

The aim of this study is to form orthorhombic ( $\beta$ ) and nanocrystalline (NC) iron disilicide ( $\text{FeSi}_2$ ) films via sputtering under the variations of substrate temperature ( $T_{\text{sub}}$ ), annealing temperature ( $T_{\text{ann}}$ ) and carbon (C) doping concentration to modify their surface morphological, wetting and mechanical properties. The results showed that the variations of  $T_{\text{sub}}$  influenced a wetting property for the  $\beta$ - $\text{FeSi}_2$  films, where the average contact angle ( $\theta_{\text{CA}}$ ) for the  $\beta$ - $\text{FeSi}_2$  films formed at 500 °C was changed from 99.25° to 102.00° after providing a higher  $T_{\text{sub}}$  of 600 °C. By variation of  $T_{\text{ann}}$ , the  $\theta_{\text{CA}}$  unannealed  $\beta$ - $\text{FeSi}_2$  was 93.25°, which decreased to 82.15° after annealed at 600 °C. The hardness and reduced elastic modulus for the  $\beta$ - $\text{FeSi}_2$  were 37.55 GPa and 643.72 GPa, which improved to 37.55 GPa and 756.50 GPa, respectively, by annealing at 600 °C. For the NC- $\text{FeSi}_2$ , the surface held an  $\theta_{\text{CA}}$  of 102.35°, which decreased to 41.70° after annealing at 500 °C. For C-doping concentration, the undoped  $\beta$ - $\text{FeSi}_2$  film's surface presented a  $\theta_{\text{CA}}$  of 108.35°, while it was slightly decreased to 103.65° after increasing the C-doping concentrations of 3.0 at.%. The results presented that the  $\beta$ - $\text{FeSi}_2$  formed different  $T_{\text{sub}}$  and C-doping concentration, together with the NC- $\text{FeSi}_2$  with a  $T_{\text{ann}}$  less than 500 °C, displayed a performance for employing in hydrophobic coating. Moreover, the as-deposited and annealed  $\beta$ - $\text{FeSi}_2$  films showed a performance for a hard coating application.

## Acknowledgements

I would like to express my sincere gratitude to my advisor, Asst.Prof.Dr. Nathaporn Promros for all of his support, advice and kindness that he always gave to me and the others research member. Asst.Prof.Dr. Nathaporn Promros always provides the opportunities to improve my skills while I study at King Mongkut Institute of Technology Ladkrabang (KMITL).

I am sincerely appreciated Dr. Mati Horprathum, the chairperson, for his support and valuable research advice to improve the quality of this research. It was an honor to receive his support whether at KMITL and National Electronics and Computer Technology Center (NECTEC).

I would like to give my thankfulness to Assc.Prof.Dr. Pattareeya Damrongsak, Asst.Prof.Dr. Pisan Sukwisute and Dr. Pichanan Teesetsopon, who are the honourable examiner as well as the skillful lecturers of Department of Physics, KMITL for their valuable research and study advice, which they always provide to all their students.

I would like to acknowledge Prof.Dr. Tsuyoshi Yoshitake and his research student for all the advice and research supportance in many ways.

Furthermore, I would like to appreciate Ms. Rawiwan Chaleawpong and Mr. Natthakorn Borwornmetee, including Mr. Phongsaphak Sittimart for all of their help while I conducted the research.

At last, I would like to give all my thankfulness to my parents for their support and encouragement in many kinds.

Mr. Peerasil Charoenyuenyao

# Table of contents

	Page
Abstract	i
Acknowledgements	ii
Table of contents	iii
List of tables	vi
List of figures	vii
<b>Chapter 1 Introduction</b> .....	<b>1</b>
1.1 Research motivation.....	1
1.2 Objectives of the study.....	2
1.3 Scopes of the study.....	2
1.4 Research procedure.....	3
1.5 Benefits of the study.....	3
<b>Chapter 2 Theory and literature reviews</b> .....	<b>4</b>
2.1 Fe-Si system.....	4
2.2 Semiconducting $\beta$ -FeSi <sub>2</sub> .....	5
2.3 Properties of NC-FeSi <sub>2</sub> .....	8
2.4 Magnetron sputtering.....	9
2.4.1 FTDCS system.....	11
2.4.2 RFMS system.....	12
2.5 Advantages of T <sub>sub</sub> on thin film deposition.....	14
2.6 Heat treatment.....	14
2.7 Influence of C-doping on $\beta$ -FeSi <sub>2</sub> films.....	15
2.8 Characterization techniques.....	15
2.8.1 X-ray diffraction.....	15
2.8.2 Raman spectroscopy.....	16
2.8.3 Scanning electron microscope.....	17
2.8.4 Atomic force microscopy.....	18
2.8.5 Contact angle measurement.....	19
2.8.6 Nanoindentation.....	20
2.9 Related research.....	21

## Table of contents (cont.)

	Page
2.9.1 Influences of $T_{\text{sub}}$ and $T_{\text{ann}}$ on thin film's properties.....	21
2.9.2 Influences of C-doping on thin film's properties.....	23
<b>Chapter 3 Research methodology</b> .....	<b>24</b>
3.1 Cleansing procedure for the Si substrates .....	25
3.2 Fabrication process for unannealed $\beta$ -FeSi <sub>2</sub> sample via FTDCS .....	25
3.2.1 Annealing procedure .....	26
3.3 Preparation of $\beta$ -FeSi <sub>2</sub> samples via RFMS at different $T_{\text{sub}}$ .....	27
3.4 Fabrication process for unannealed NC-FeSi <sub>2</sub> sample via RFMS .....	28
3.4.1 Annealing procedure .....	29
3.5 Preparation of undoped and C-doped $\beta$ -FeSi <sub>2</sub> films via RFMS .....	30
3.6 Investigation techniques.....	31
3.6.1 Structural investigation .....	31
3.6.2 Morphology investigation .....	33
3.6.3 Wetting angle investigation .....	34
3.6.4 Mechanical investigation.....	35
3.6.5 Optical investigation .....	36
<b>Chapter 4 Results and discussion</b> .....	<b>37</b>
4.1 Effect of $T_{\text{ann}}$ on the characteristics of $\beta$ -FeSi <sub>2</sub> films prepared via FTDCS .....	37
4.1.1 Raman spectra .....	37
4.1.2 Surface and cross-section morphologies .....	38
4.1.3 Surface roughness .....	40
4.1.4 Wetting angle .....	41
4.1.5 Mechanical property.....	43
4.2 Effect of $T_{\text{sub}}$ on the properties of $\beta$ -FeSi <sub>2</sub> films formed via RFMS...	45
4.2.1 Raman spectra .....	45
4.2.2 Surface and cross-section morphologies .....	46
4.2.3 Surface roughness .....	47
4.2.4 Wetting angle .....	48

## Table of contents (cont.)

	Page
4.3 Effect of $T_{\text{ann}}$ on the characteristics of NC-FeSi <sub>2</sub> films prepared via RFMS .....	50
4.3.1 XRD patterns.....	50
4.3.2 Raman spectra .....	51
4.3.3 Surface morphology .....	52
4.3.4 Surface roughness .....	53
4.3.5 Wetting angle .....	54
4.4 Effect of C-doping concentrations on characteristics of $\beta$ -FeSi <sub>2</sub> films prepared via RFMS.....	56
4.4.1 XRD patterns.....	56
4.4.2 Raman spectra .....	57
4.4.3 Optical property .....	57
4.4.4 Surface morphology .....	59
4.4.5 Surface roughness .....	60
4.4.6 Wetting angle .....	61
<b>Chapter 5 Conclusions and suggestions .....</b>	<b>63</b>
5.1 Effect of $T_{\text{ann}}$ on $\beta$ -FeSi <sub>2</sub> films prepared via FTDCS.....	63
5.2 Effect of $T_{\text{sub}}$ on $\beta$ -FeSi <sub>2</sub> films formed via RFMS.....	64
5.3 Effect of $T_{\text{ann}}$ on NC-FeSi <sub>2</sub> films formed via RFMS.....	64
5.4 Effect of C-doping concentrations on $\beta$ -FeSi <sub>2</sub> films formed via RFMS.....	64
5.5 Suggestions .....	65
References .....	66
Author Biography .....	75

## List of tables

Table	Page
3.1 Fabrication details for $\beta$ -FeSi <sub>2</sub> films via FTDCS before annealing.....	26
3.2 Annealing conditions for the $\beta$ -FeSi <sub>2</sub> films formed via FTDCS .....	26
3.3 Fabrication details for $\beta$ -FeSi <sub>2</sub> films by RFMS at varied T <sub>sub</sub> .....	28
3.4 Fabrication condition for NC-FeSi <sub>2</sub> films via RFMS before annealing .....	29
3.5 Annealing conditions for the as-prepared NC-FeSi <sub>2</sub> films via RFMS .....	29
3.6 Fabrication condition for the undoped and C-doped $\beta$ -FeSi <sub>2</sub> films via RFMS at different C-doping concentrations.....	31
4.1 Surface R <sub>rms</sub> for the $\beta$ -FeSi <sub>2</sub> films after annealing. ....	40
4.2 $\theta_{CA}$ and wetting state for the $\beta$ -FeSi <sub>2</sub> films at different T <sub>ann</sub> .....	42
4.3 Hardness and reduced elastic modulus for $\beta$ -FeSi <sub>2</sub> films at different T <sub>ann</sub> .....	44
4.4 Surface R <sub>rms</sub> for the $\beta$ -FeSi <sub>2</sub> films formed at different T <sub>sub</sub> .....	48
4.5 $\theta_{CA}$ and wetting state for the $\beta$ -FeSi <sub>2</sub> films formed at different T <sub>sub</sub> .....	49
4.6 Surface R <sub>rms</sub> for NC-FeSi <sub>2</sub> films at different T <sub>ann</sub> .....	54
4.7 $\theta_{CA}$ and wetting state for NC-FeSi <sub>2</sub> films at different T <sub>ann</sub> .....	55
4.8 Thickness, transmittance percentage and E <sub>g</sub> for the $\beta$ -FeSi <sub>2</sub> films under different C-doping concentrations .....	58
4.9 Surface R <sub>rms</sub> for $\beta$ -FeSi <sub>2</sub> films at different C-doping concentrations.....	61
4.10 $\theta_{CA}$ and wetting state for $\beta$ -FeSi <sub>2</sub> films at different C-doping concentrations.	62

## List of figures

Figure	Page
2.1 Phase diagram for the Fe-Si systems of FeSi <sub>2</sub> .....	5
2.2 Primitive cell for the $\beta$ structure of FeSi <sub>2</sub> .....	6
2.3 Epitaxial relationships for $\beta$ -FeSi <sub>2</sub> on Si(111) .....	6
2.4 Band diagram of $\beta$ -FeSi <sub>2</sub> .....	7
2.5 Absorption spectrum for $\beta$ -FeSi <sub>2</sub> . The inset presents the interpolate indirect and direct $E_g$ of $\beta$ -FeSi <sub>2</sub> .....	8
2.6 TEM image of NC-FeSi <sub>2</sub> films.....	9
2.7 Diagram for the ejection of the secondary electron due to ion bombarding at target's surface .....	10
2.8 Schematic diagram for the general confinement of plasma for magnetron sputtering system.....	11
2.9 Schematic diagram for the fabrication technique of FTDCS.....	12
2.10 Schematic diagram for the fabrication technique of RFMS.....	13
2.11 Diagram for XRD technique .....	16
2.12 Schematic 2D diagram for Raman spectroscopy.....	17
2.13 2D-diagram for SEM equipment.....	18
2.14 Diagram for general AFM apparatus.....	19
2.15 Schematic diagram for the general wetting state on the solid surface substrate at different ranging of CA.....	20
2.16 Schematic diagram for a nanoindentation apparatus.....	21
2.17 AFM images for as-prepared Ni films at (a) 30 °C (b) 300 °C and (c) 500 °C .....	22
2.18 AFM images for Ni films after annealing at (a) 300 °C and (b) 500 °C .....	22
2.19 The change of surface and wetting angles of TN films at different $T_{ann}$ .....	23
2.20 Plane surface views for the $\beta$ -FeSi <sub>2</sub> films formed via ion implantation in case of (a) without C-doping and (b) with C-doping.....	23
3.1 (a) FTDCS and (b) RFMS systems for sample preparation .....	24
3.2 Thermal annealing apparatus for annealing of the as-prepared $\beta$ -FeSi <sub>2</sub> samples at different $T_{ann}$ of 200 °C, 400 °C and 600 °C.....	27
3.3 Annealing furnace for the as-prepared NC-FeSi <sub>2</sub> films.....	30

## List of figures (cont.)

Figure	Page
3.4 The as-deposited and annealed NC-FeSi <sub>2</sub> films at different T <sub>ann</sub> of 100 °C, 300 °C and 500 °C .....	30
3.5 XRD diffractometer (Rigaku, model TTRAX III) .....	32
3.6 Dispersive Raman spectroscopy (Bruker, model SENTERA II).....	32
3.7 FESEM apparatus (Zeiss, model Auriga) .....	33
3.8 Scanning electron microscope (Hitachi, model SU8230) .....	33
3.9 AFM apparatus (Park system, XE-120) .....	34
3.10 Contact angle analyzer (Dataphysics, model OCA 20) and a display monitor	35
3.11 DI water droplet on the film's surface in (a) normal view and (b) view on the monitor with an estimation of contact angle values .....	35
3.12 Nanoindentation apparatus (Micromaterial, model Nanotest Vantage).....	36
3.13 Ultraviolet-visible-NIR spectrophotometer (Jasco, model V570).....	36
4.1 Raman spectra for the $\beta$ -FeSi <sub>2</sub> films deposited by FTDCS with different T <sub>ann</sub> .	38
4.2 The views of (a) surface and (b) cross-sectional of the $\beta$ -FeSi <sub>2</sub> films prepared by FTDCS system with post-annealing at different T <sub>ann</sub> .....	39
4.3 AFM results for the $\beta$ -FeSi <sub>2</sub> films prepared by FTDCS technique under different T <sub>ann</sub> .....	41
4.4 Wetting angle between the probe liquid and $\beta$ -FeSi <sub>2</sub> film's surface with different annealing conditions .....	42
4.5 Load-depth plots of the $\beta$ -FeSi <sub>2</sub> films after annealing at 200 °C, 400 °C and 600 °C.....	44
4.6 Raman lines of the prepared $\beta$ -FeSi <sub>2</sub> thin films via RFMS method at different T <sub>sub</sub> of 500 °C, 560 °C, and 600 °C .....	46
4.7 Planar and cross-sectional images of the $\beta$ -FeSi <sub>2</sub> films prepared at the T <sub>sub</sub> of 500 °C, 560 °C, and 600 °C .....	47
4.8 AFM images of the $\beta$ -FeSi <sub>2</sub> film surface fabricated at T <sub>sub</sub> of 500°C, 560 °C, and 600 °C via RFMS .....	48
4.9 Wetting angle for the surface of $\beta$ -FeSi <sub>2</sub> films formed via RFMS at different T <sub>sub</sub> .....	49

## List of figures (cont.)

Figure	Page
4.10 Diffraction patterns for the NC-FeSi <sub>2</sub> films at different T <sub>ann</sub> .....	51
4.11 Raman profiles for the NC-FeSi <sub>2</sub> films formed via RFMS at T <sub>sub</sub> of RT, under different T <sub>ann</sub> .....	52
4.12 Surface images for the NC-FeSi <sub>2</sub> films at different T <sub>ann</sub> .....	53
4.13 AFM images of NC-FeSi <sub>2</sub> films after annealing at different T <sub>ann</sub> .....	54
4.14 Wetting angle for the NC-FeSi <sub>2</sub> films after annealing at T <sub>ann</sub> of 100 °C, 300 °C and 500 °C.....	55
4.15 Diffraction pattern for the $\beta$ -FeSi <sub>2</sub> films formed via RFMS at various C-doping concentrations .....	56
4.16 Raman profiles of $\beta$ -FeSi <sub>2</sub> films formed via RFMS at different C-doping concentrations .....	57
4.17 Transmittance lines for the $\beta$ -FeSi <sub>2</sub> films formed at different C-doping concentrations. The inset shows the $(\alpha h\nu)^2$ versus $h\nu$ plot for each film.....	59
4.18 Plane surface for the $\beta$ -FeSi <sub>2</sub> films formed using different C-doping concentrations via RFMS technique .....	60
4.19 AFM images of $\beta$ -FeSi <sub>2</sub> films formed via RFMS at different doping concentrations .....	61
4.20 Wetting angle for the $\beta$ -FeSi <sub>2</sub> film surface at different C-doped concentrations .....	62

# Chapter 1

## Introduction

### 1.1 Research motivation

Orthorhombic semiconducting phase ( $\beta$ ) iron disilicide ( $\text{FeSi}_2$ ) is a probable candidate as a coating material [1-3].  $\beta$ - $\text{FeSi}_2$  films can be formed using the abundant and eco-friendly materials of iron (Fe) and silicon (Si) [4,5]. The surface for  $\beta$ - $\text{FeSi}_2$  films is smooth and hydrophobic with an average contact angle ( $\theta_{CA}$ ) over than  $90^\circ$  [6]. Nanocrystalline (NC) forms of  $\text{FeSi}_2$  films have distinctive characteristics comparable to those of  $\beta$ - $\text{FeSi}_2$ , which can be formed at room temperature (RT) [7,8]. NC- $\text{FeSi}_2$  films also held a smooth surface with a crystalline diameter of less than 10 nm [9-11]. While research on the production of p-Si/n- $\beta$ - $\text{FeSi}_2$  junctions via sputtering and their application to photodiodes have been actively conducted [4,12-14], there have been a few reports on the wetting and mechanical features for  $\beta$ - $\text{FeSi}_2$  films, as well as the impacts of substrate temperature ( $T_{sub}$ ), annealing temperature ( $T_{ann}$ ) and carbon (C)-doping concentration on the wetting and mechanical features of  $\beta$ - $\text{FeSi}_2$  films, including NC- $\text{FeSi}_2$  films. In fact,  $T_{sub}$ ,  $T_{ann}$  and C-doping could be employed to modify the structure and surface features of thin films.  $T_{sub}$  and  $T_{ann}$  had the advantages to improve the mobility and diffusion of atoms, resulting to an increasing of nucleation density and uniform surface distribution [15-19]. For C-doping, the imperfection of lattice property for  $\beta$ - $\text{FeSi}_2$  films could be lessened [20-23]. The modification of these features could impact to the wetting and mechanical features.

The objective of this research is focus on the formation of  $\beta$ - and NC- $\text{FeSi}_2$  films via sputtering to study their surface morphological, wetting and mechanical properties, including the impact of  $T_{sub}$ ,  $T_{ann}$  and C-doping concentration on those features. This research provides those properties of  $\beta$ - and NC- $\text{FeSi}_2$  films and optimizes these materials under the experimental conditions for hydrophobic and hard coating applications. The result showed that the  $\theta_{CA}$  for  $\beta$ - $\text{FeSi}_2$  films formed at  $T_{sub}$  of  $500^\circ\text{C}$  was increased from  $99.25^\circ$  to  $99.80^\circ$  and  $102.00^\circ$  at higher  $T_{sub}$  of  $560^\circ\text{C}$  and  $600^\circ\text{C}$ , respectively, which expressed the potential for hydrophobic coating. With a variation of  $T_{ann}$  factor, the annealed  $\beta$ - $\text{FeSi}_2$  films at  $200^\circ\text{C}$  exhibited a potential for hydrophobic coating with a  $\theta_{CA}$  of  $93.25^\circ$ , while the  $\theta_{CA}$  was decreased to lower than  $90^\circ$  after

annealed at  $T_{\text{ann}}$  of 400 and 600 °C. Despite, the hardness for the  $\beta$ -FeSi<sub>2</sub> films was improved from 37.55 GPa to 64.88 GPa after annealed at 600 °C, which presented an attractive performance for hard coating. For the NC-FeSi<sub>2</sub> films, the as-deposited and annealed NC-FeSi<sub>2</sub> under  $T_{\text{ann}}$  of 100 and 300 °C held a potential for hydrophobic coating with the  $\theta_{\text{CA}}$  of over than 90°, while the  $\theta_{\text{CA}}$  decreased to lower than that range after annealed at 500 °C. With a variation of C-doping concentration, all undoped and C-doped  $\beta$ -FeSi<sub>2</sub> films, at 0.5 to 3.0 at.%, had a potential for hydrophobic applications, while the  $\theta_{\text{CA}}$  values for the undoped and 3.0 at.% C-doped  $\beta$ -FeSi<sub>2</sub> films were 108.35° and 103.65°, respectively.

## 1.2 Objectives of the study

1. To form  $\beta$ -FeSi<sub>2</sub> and NC-FeSi<sub>2</sub> films via sputtering and to provide their initial surface morphological, wetting and mechanical properties.
2. To study the impact of  $T_{\text{sub}}$ ,  $T_{\text{ann}}$  and C-doping concentration on surface morphological, wetting and mechanical properties of  $\beta$ -FeSi<sub>2</sub> and NC-FeSi<sub>2</sub> films.
3. To optimize  $\beta$ -FeSi<sub>2</sub> and NC-FeSi<sub>2</sub> films under variations of  $T_{\text{sub}}$ ,  $T_{\text{ann}}$  and C-doping concentration for hydrophobic and hard coatings.

## 1.3 Scopes of the study

1. The effect of  $T_{\text{sub}}$  was studied on the  $\beta$ -FeSi<sub>2</sub> films formed via sputtering at  $T_{\text{sub}}$  ranging of 500 to 600 °C.
2. The effect of  $T_{\text{ann}}$  was investigated on the annealed  $\beta$ -FeSi<sub>2</sub> at  $T_{\text{ann}}$  of 200, 400 and 600 °C, including the annealed NC-FeSi<sub>2</sub> films at 100 °C, 300 °C and 500 °C.
3. The effect of C-doping concentrations was researched through the  $\beta$ -FeSi<sub>2</sub> films formed via sputtering using the FeSi<sub>2</sub> alloy targets with the C-doping concentrations of undoped, 0.5 at.%, 1.0 at.% and 3.0 at.%.

#### 1.4 Research procedure

1. Study the research background regarding to  $\beta$ - and NC-FeSi<sub>2</sub> films, including a searching of new research idea.
2. Prepare  $\beta$ - and NC-FeSi<sub>2</sub> films, including characterize their surface, wetting and mechanical properties.
3. Prepare  $\beta$ -FeSi<sub>2</sub> films at varied  $T_{\text{sub}}$ , including characterize their surface, wetting and mechanical properties.
4. Anneal  $\beta$ - and NC-FeSi<sub>2</sub> films at varied  $T_{\text{ann}}$ , including characterize their surface, wetting and mechanical properties.
5. Prepare  $\beta$ -FeSi<sub>2</sub> films at different C-doping concentrations, including characterize their surface and wetting properties.
6. Summarize the effect of  $T_{\text{sub}}$ ,  $T_{\text{ann}}$  and C-doping concentrations on film's properties.
7. Provide all research data for thesis writing.

#### 1.5 Benefits of the study

1. Receive the initial surface morphological, wetting and mechanical properties for the  $\beta$ -FeSi<sub>2</sub> and NC-FeSi<sub>2</sub> films prepared via sputtering.
2. Provide surface morphological, wetting and mechanical properties of  $\beta$ -FeSi<sub>2</sub> and NC-FeSi<sub>2</sub> films under the variations of  $T_{\text{sub}}$ ,  $T_{\text{ann}}$  and C-doping concentrations.
3. Earn the optimized conditions for using  $\beta$ -FeSi<sub>2</sub> and NC-FeSi<sub>2</sub> films in hydrophobic and hard coating applications.

## Chapter 2

### Theory and literature reviews

This chapter describes the information for theory and literature reviews associated to this research. Initially, the essential properties for semiconducting  $\text{FeSi}_2$  films were introduced. The fabrication techniques for the  $\text{FeSi}_2$  films were sequentially explained. Then, the topics of annealing process, wetting property, mechanical properties were presented. The literature reviews were presented in a final section of this chapter.

#### 2.1 Fe-Si system [24-31]

There has been previously researched on the binary system between Fe and Si that Fe-Si system consists various phases such as intermetallic phase ( $\text{Fe}_5\text{Si}_3$ ), ferromagnetic silicide ( $\text{Fe}_3\text{Si}$ ), monosilicide ( $\text{FeSi}$ ) and disilicide ( $\text{FeSi}_2$ ). Among those phases,  $\text{FeSi}_2$  is the one of an appealing material for the Fe-Si system that receives an attention from several research groups, due to a potential for optoelectronic application. Considering to  $\text{FeSi}_2$  systems, this material can also be categorized in three main structures of cubic ( $\gamma\text{-FeSi}_2$ ), orthorhombic ( $\beta\text{-FeSi}_2$ ) and tetragonal ( $\alpha\text{-FeSi}_2$ ), respectively. Figure 2.1 represents a systematical phase diagram for Fe-Si system. From Figure 2.1, there has been considered that ranging of temperature is one of a function included in the phase diagram for Fe-Si system. For  $\text{FeSi}_2$  material, it has been reported on the temperature stability for each consistent phase of  $\gamma\text{-FeSi}_2$ ,  $\beta\text{-FeSi}_2$  and  $\alpha\text{-FeSi}_2$ . Specifically,  $\gamma\text{-FeSi}_2$  has a metastable phase which develops during a polymorphic transformation of  $\beta\text{-FeSi}_2$  at 650 °C. For  $\beta\text{-FeSi}_2$ , this phase exhibits a semiconducting and exist at the stoichiometric composition, where  $\beta\text{-FeSi}_2$  is stable at temperature below 950 °C.  $\alpha\text{-FeSi}_2$  phase has a wide single-phase composition range due to vacancies in the Fe sub-lattice, which is stable at temperature above 950 °C. Lately, for  $\text{FeSi}_2$  system, the semiconducting  $\beta\text{-FeSi}_2$  has drew a major attention over their properties for utilizing as an optoelectronic device.

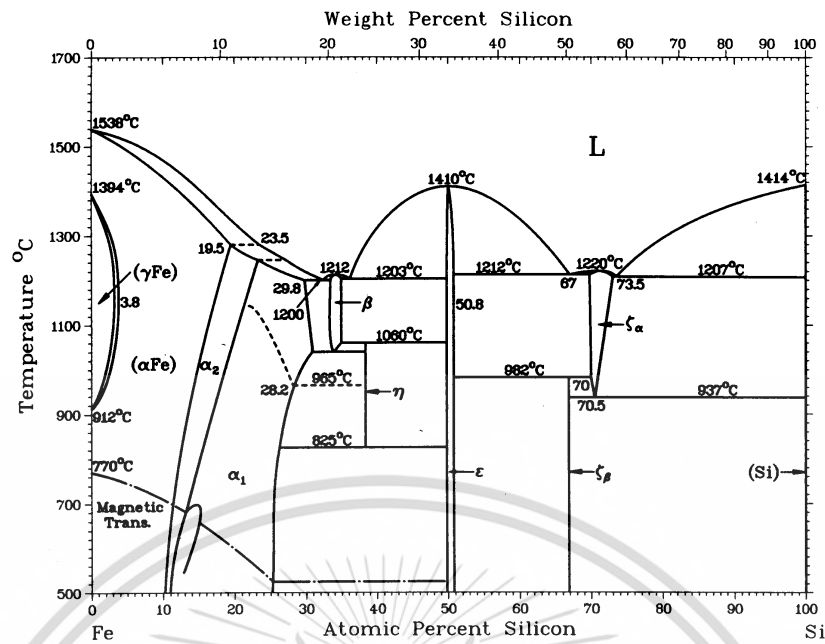


Figure 2.1 Phase diagram for the Fe-Si systems of  $\text{FeSi}_2$ . [24]

## 2.2 Semiconducting $\beta\text{-FeSi}_2$ [32-39]

For the semiconducting  $\beta\text{-FeSi}_2$ , this material can be composed from two abundant and toxic-free material of Fe and Si. The structure for  $\beta\text{-FeSi}_2$  is introduced to be an orthorhombic structure under  $\text{FeSi}_2$  system. As depicted in Figure 2.2,  $\beta\text{-FeSi}_2$  structure contains 48 atoms per their primitive cell, which is 16 atoms of Fe and 32 atoms of Si. The lattice parameter is  $a = 0.986$  nm,  $b = 0.778$  nm and  $c = 0.788$  nm. Their unit cell occupies two inequivalent Fe sites with 8 Fe atoms of each and two inequivalent Si site with 16 atoms of Fe. Moreover, the  $\beta\text{-FeSi}_2$  films can be epitaxially fabricated onto the Si substrate, where the heterostructure between  $\beta\text{-FeSi}_2$  and Si substrate consisted of a minor lattice mismatch of less than 5%. Figure 2.3 demonstrated the three possible variants of epitaxial formation for the  $\beta\text{-FeSi}_2$  and Si(111). The relationship of the heteroepitaxy of  $\beta\text{-FeSi}_2$  and Si with an orientation of (111) are exhibited with two forms as below:

- (i)  $\text{FeSi}_2$  (110)/Si(111) with  $\text{FeSi}_2$  [001]//Si <110>
- (ii)  $\text{FeSi}_2$  (101)/Si(111) with  $\text{FeSi}_2$  [010]//Si <011>

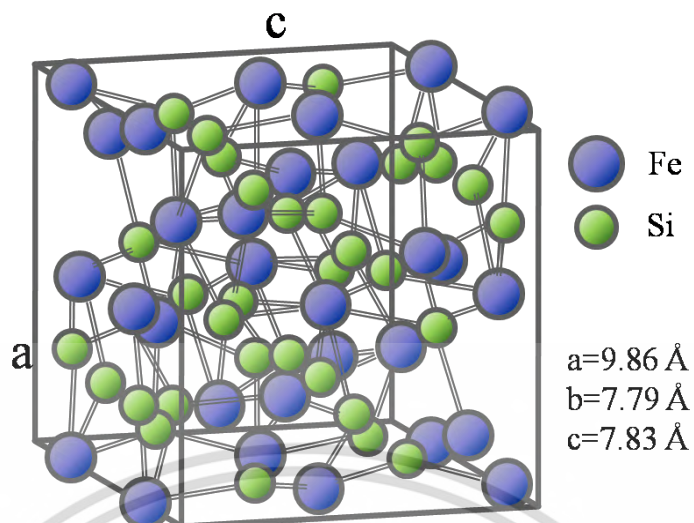


Figure 2.2 Primitive cell for the  $\beta$  structure of  $\text{FeSi}_2$ .

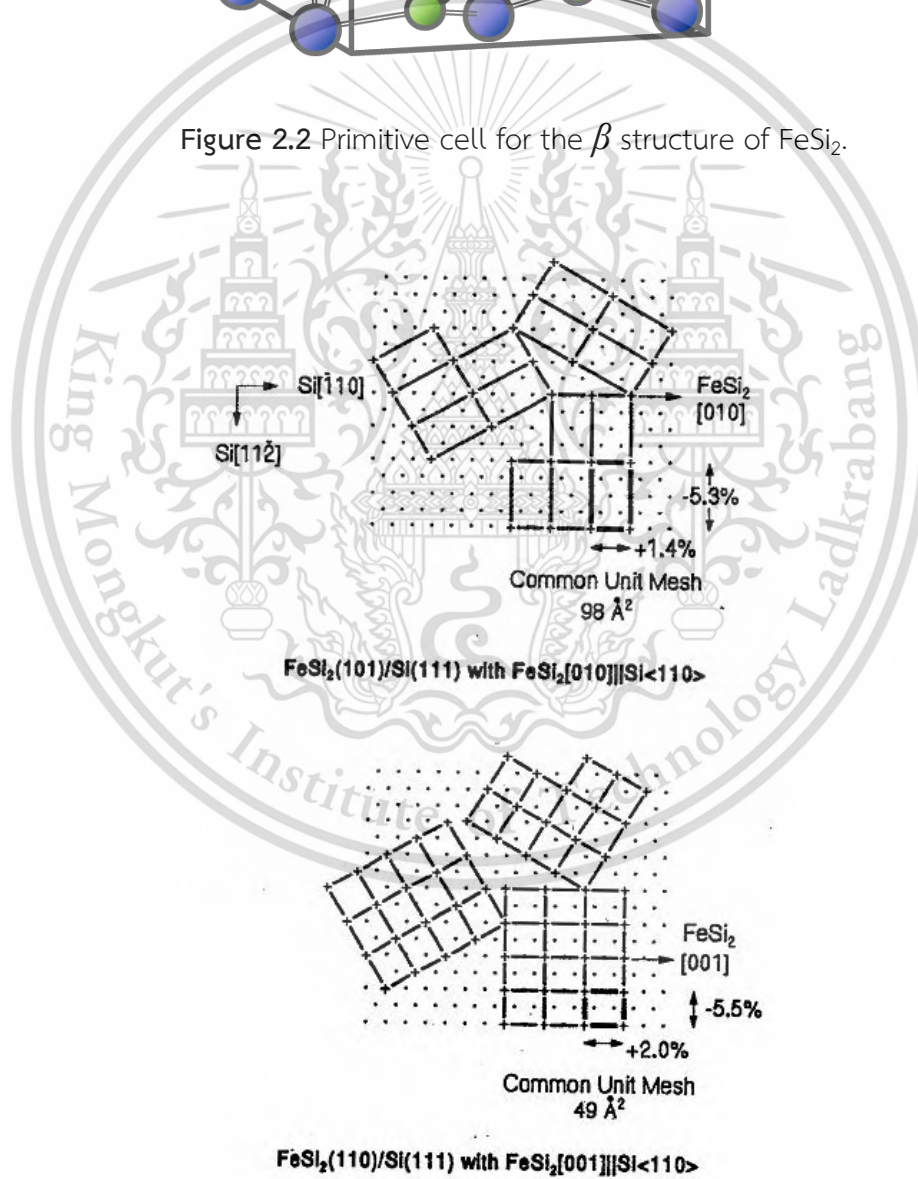


Figure 2.3 Epitaxial relationships for  $\beta$ - $\text{FeSi}_2$  on  $\text{Si}(111)$ . [39]

This material is reserved for educational use only, not allowed for commercial use.  
 Forbidden to modify the content, and cite the document when use.

Figure 2.4 displays a band diagram of  $\beta$ -FeSi<sub>2</sub> for energy close to the band gap. The optical properties for the  $\beta$ -FeSi<sub>2</sub> films had been revealed that  $\beta$ -FeSi<sub>2</sub> films held a direct band gap ( $E_g$ ) of 0.85 eV and an indirect  $E_g$  of 0.76 eV, respectively. The difference between the calculated direct and indirect  $E_g$  is quite small. An indirect  $E_g$  could explain the part of absorption found for energy below the direct-gap transition energy. For this  $E_g$  ranging, the  $\beta$ -FeSi<sub>2</sub> was confirmed that it was conformed to a wavelength for optical fiber telecommunication. The optical absorption coefficient for  $\beta$ -FeSi<sub>2</sub> is larger than  $10^5 \text{ cm}^{-1}$  at 1.2 eV. This value of absorption coefficient is at least two orders of magnitude higher than that of crystalline Si at 1.2 eV, as illustrated in Figure. 2.5.

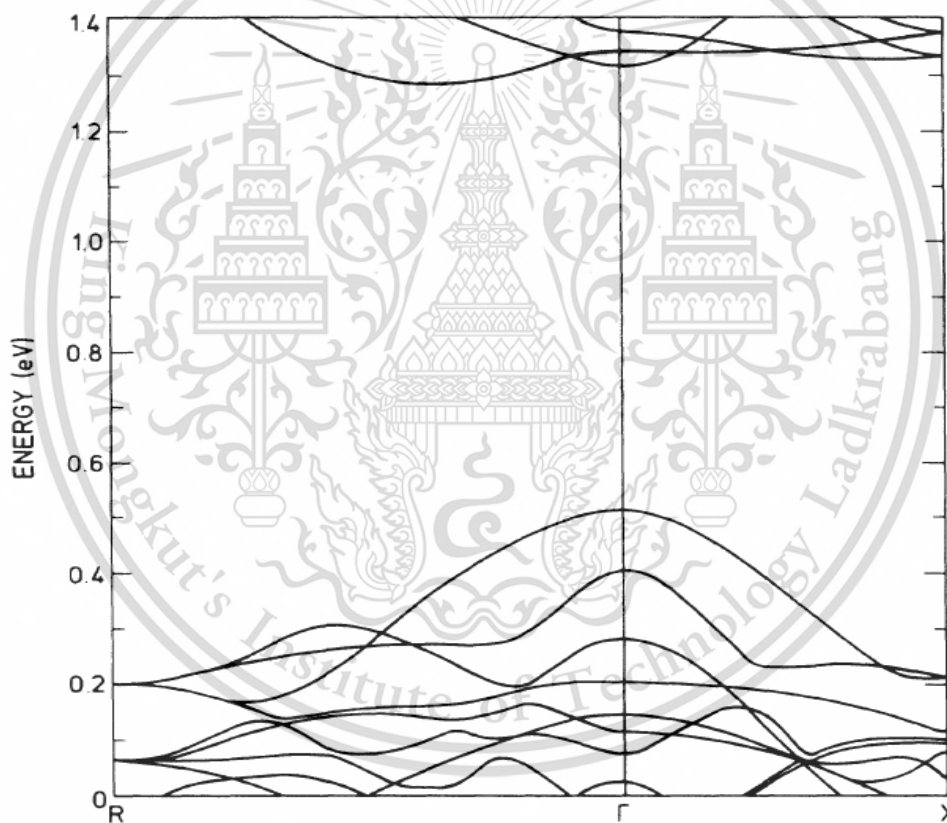


Figure 2.4 Band diagram of  $\beta$ -FeSi<sub>2</sub>. [35]

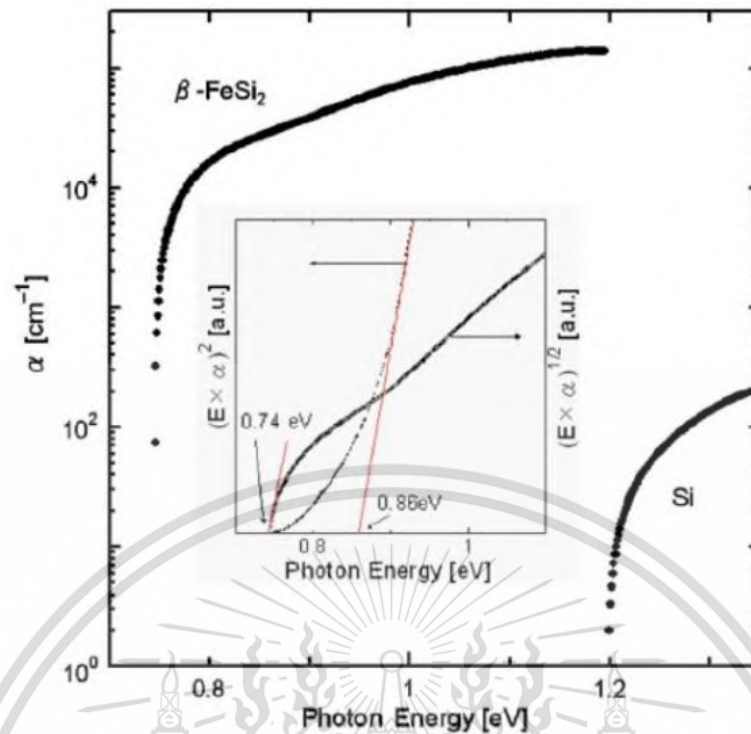


Figure 2.5 Absorption spectrum for  $\beta$ -FeSi<sub>2</sub>. The inset presents the interpolate indirect and direct  $E_g$  of  $\beta$ -FeSi<sub>2</sub>. [35]

### 2.3 Properties of NC-FeSi<sub>2</sub> [40-48]

NC-FeSi<sub>2</sub> held a similarity of their properties to the  $\beta$ -FeSi<sub>2</sub> films. For NC-FeSi<sub>2</sub>, this material can be formed by utilizing Fe and Si, which are the abundant and toxic-free materials. Further, NC-FeSi<sub>2</sub> can be formed onto various kinds of solid-substrate at RT, where it comprised of several crystallites with a diameter of less than 10 nm. As well, NC-FeSi<sub>2</sub> films own their direct and indirect  $E_g$  of 0.85 eV and 0.74 eV, where their absorption coefficient of larger than  $10^5 \text{ cm}^{-1}$ . Several research groups had been reported that NC-FeSi<sub>2</sub> can be achieved by employing different fabrication techniques.

Recently, NC-FeSi<sub>2</sub> films were reported that the films could be formed onto the Si substrate by utilizing a fabrication technique of FTDCS at RT. The structural property for the as-formed NC-FeSi<sub>2</sub> films was indicated that the diffraction peaks exhibited the board peak shape at  $2\theta$  between  $40^\circ$  and  $50^\circ$ , which due to the accumulation of the  $\beta(422)$ ,  $\beta(511)$ ,  $\beta(313)$ ,  $\beta(331)$ ,  $\beta(004)$ ,  $\beta(040)$ ,  $\beta(114)$  and  $\beta(133)$  peaks. The broad shape implied that a crystallite diameter is in nano-scale. Also, the

NC-FeSi<sub>2</sub> films were identified that they possessed a n-type conduction with a residual  
 This material is reserved for educational use only; not allowed for commercial use.  
 Forbidden to modify the content, and cite the document when use.

carrier density of around  $10^{19} \text{ cm}^{-3}$ . The nanostructure of NC-FeSi<sub>2</sub> films has been studied and confirmed by transmission electron microscopy (TEM) and field-emission scanning electron microscopy (FESEM). The p-type Si/n-type NC-FeSi<sub>2</sub> heterojunctions were formed, and their electrical properties were investigated for usage in optoelectronic devices. Nevertheless, the research involved to the surface morphology, wetting and mechanical properties of the NC-FeSi<sub>2</sub> films regarding to the fabrication technique of FTDCS, including RFMS, had been rarely conducted.

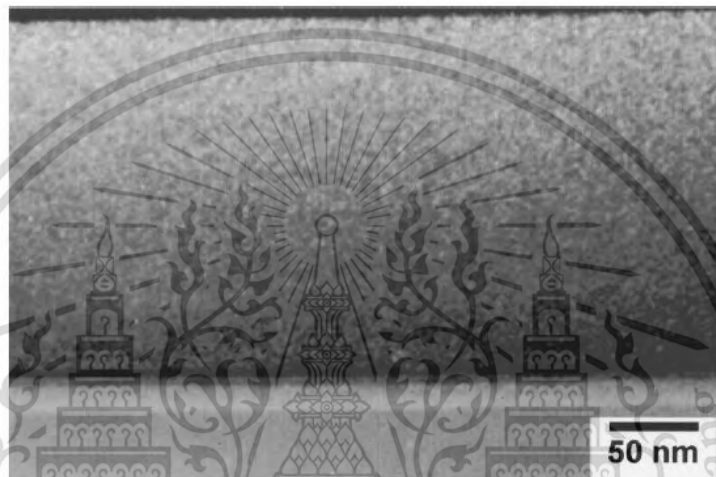


Figure 2.6 TEM image of NC-FeSi<sub>2</sub> films. [44]

#### 2.4 Magnetron sputtering [49-60]

Up to this date, a magnetron sputtering is one kind of physical vapor deposition technique, which is well-known as an effective method for thin film preparation under industrial scale. For this method, magnetron sputtering can be employed to different fabrication applications such as hard coating, wear-resistance coating and large-scale coating. Primarily, sputtering is a process describes a bombarding between the energetic ions and an atom's surface, which results to an ejection of the secondary electron as depicts in Figure 2.7. Then, an ejection of secondary electron could be ejected from the material target in a case of an energy from the incident ion beyond the surface binding energy for the material target. For magnetron sputtering, this system is defined as a sputtering process with a supportive magnetic field from the permanent magnets, which improve a plasma density, deposition rate and lifetime of the electrons around target area. So that, with this reason, the ejected secondary

electron for magnetron sputtering was controlled and guided toward a surface-plane of substrate, under the applied magnetic field. Figure 2.8 demonstrates a general diagram for basic magnetron sputtering system. For a magnetron sputtering, the systems such as direct current (DC) and radio frequency (RF) are broadly utilized for thin film fabrication, because these methods occupied an enhancement of plasma density by applying a strong magnetic field to their system.

For a sputtering using DC system, this method is applicable to deposit the films with an electrically conductive target, commonly a metal-sputtering source. Hence, a DC sputtering is not usually appropriate for utilizing as a deposition process for an insulating-sputtering source. To sputter an insulating target, a sputtering with RF systems could be employed by applying AC voltage at high frequency to the sputtering source. The detail for these magnetron systems will be discussed in the following sections.

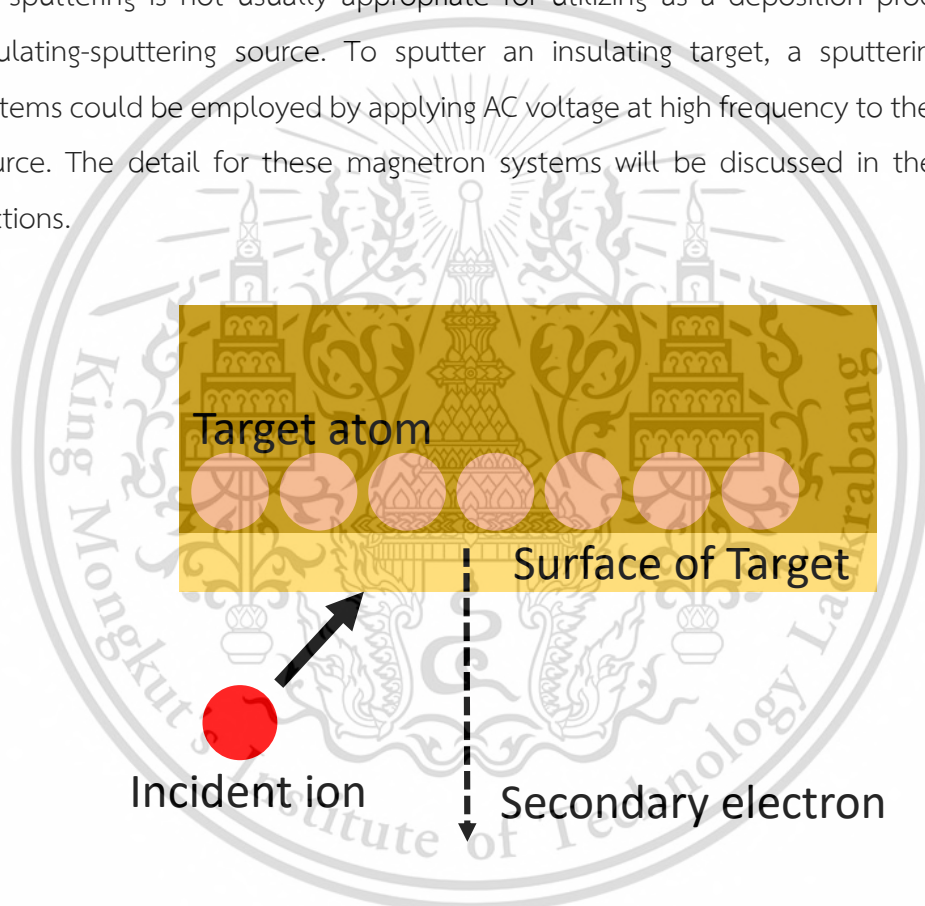


**Figure 2.7** Diagram for the ejection of the secondary electron due to ion bombarding at target's surface.

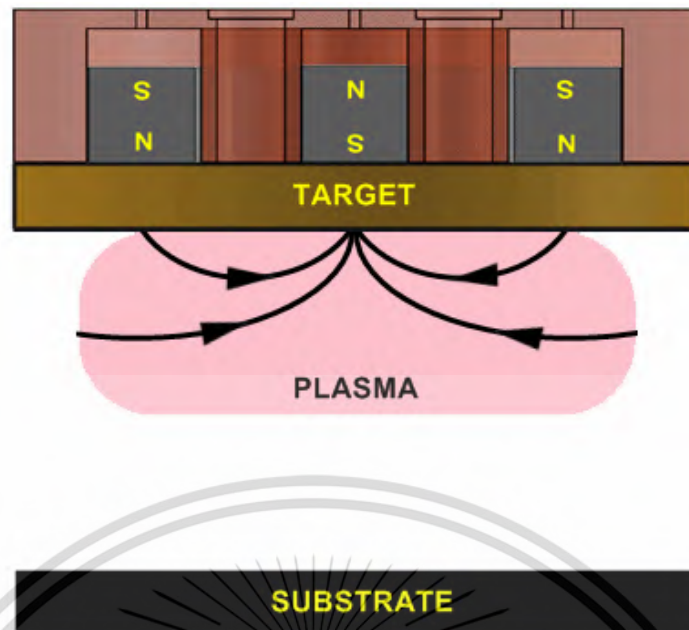


**Figure 2.8** Schematic diagram for the general confinement of plasma for magnetron sputtering system. [58]

#### 2.4.1 FTDCS system

FTDCS is one of sputtering technique under a field of DC magnetron sputtering, which can be employed for thin film deposition using dual target sources facing to each other. For FTDCS system, this technique can be utilized for deposition of film layer at low temperature and high deposition rate. The schematic diagram is presented in Figure 2.9, to systematically review the FTDCS system. Particularly, this system consists of dual target sources, which mostly are in disk shape, parallelly positioned facing together. The permanent magnets were applied beneath each target to control the direction of the secondary electrons under a magnetic region. The magnetic field at the target surface is supported to hold the electron around target's surface and control their direction. From that, it conducted a collision between the electron and inert gas's particle resulting to an ionization, where the ions were accelerated toward the material target by magnetic field.

As a magnetron sputtering, FTDCS receives merit that a direct bombardment of the charged particles, or incident ion, is suppressed from the system by supporting the magnetic field, where the substrate is located away from a plasma region as well.

This material is reserved for educational use only; not allowed for commercial use. Forbidden to modify the content, and cite the document when use.

plasma density from sputtering, less film's surface damage, low increment of  $T_{\text{sub}}$ , less film's stoichiometric difference to the targets. Also, it has been reported regarding  $\beta$ - $\text{FeSi}_2$  film production that this deposition approach could be employed to achieve the epitaxial  $\beta$ - $\text{FeSi}_2$  on Si(111) substrates at low  $T_{\text{sub}}$ . The  $T_{\text{sub}}$  for epitaxial  $\beta$ - $\text{FeSi}_2$  film deposition via FTDCS was 600 °C, which was 200 °C below the  $T_{\text{sub}}$  at which epitaxial  $\beta$ - $\text{FeSi}_2$  growth could be achieved through the usage of post-thermal annealing.

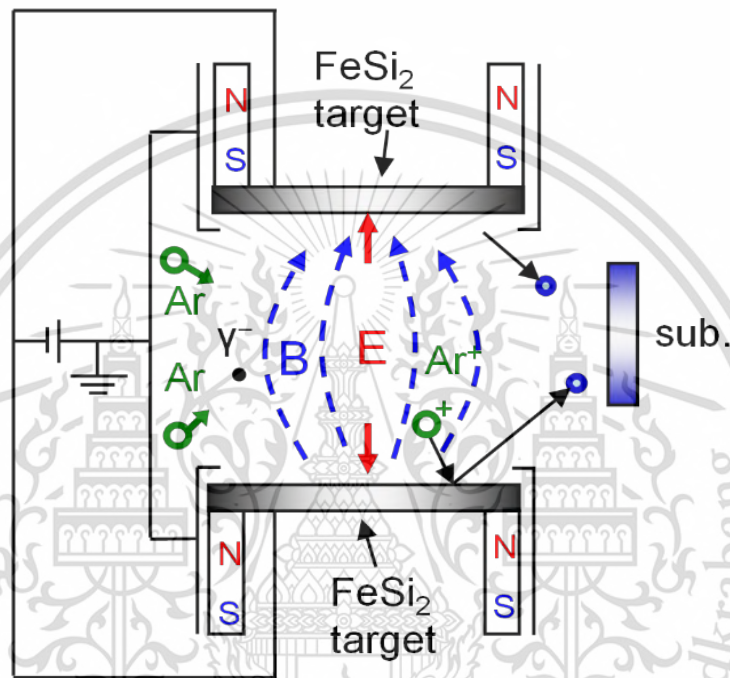


Figure 2.9 Schematic diagram for the fabrication technique of FTDCS.

#### 2.4.2 RFMS system

RFMS is a developed system for the magnetron sputtering by applying an AC with a RF supply source, which is differed to the supply source for the FTDCS system. For RFMS, a high range of frequency has been applied to the system for inducing a high difference of the mobilities of ions and electron under fluctuating field, where the typical frequency ranging commonly around 13.56 MHz. As compared to DC sputtering system, RFMS system has a unique merit to sustain a discharge for non-conductive sputtering target. Therefore, RFMS is suitable for applying as a deposition technique for the dielectric thin films, where it also provides a high deposition rate and large area of coating.

This material is reserved for educational use only, not allowed for commercial use.  
Forbidden to modify the content, and cite the document when use.

Several advantages, over the DC system, for thin film deposition could be acquired by RFMS such as longer residence times in the plasma, higher collisional ionization and higher plasma densities. Figure 2.10 provides a systematic diagram for RFMS system. This system required a matching network for an impedance ( $Z$ ) between the supply source and discharge chamber. This matching network is led into the systems for tuning of a maximum sputtering power. This method facilitates a film fabrication from the variety of materials with high deposition rate and large area. Further, RFMS also a sputtering technique which could be performed at low-pressure environment, resulting to supports an augmentation of a kinetic energy for the sputtered species.

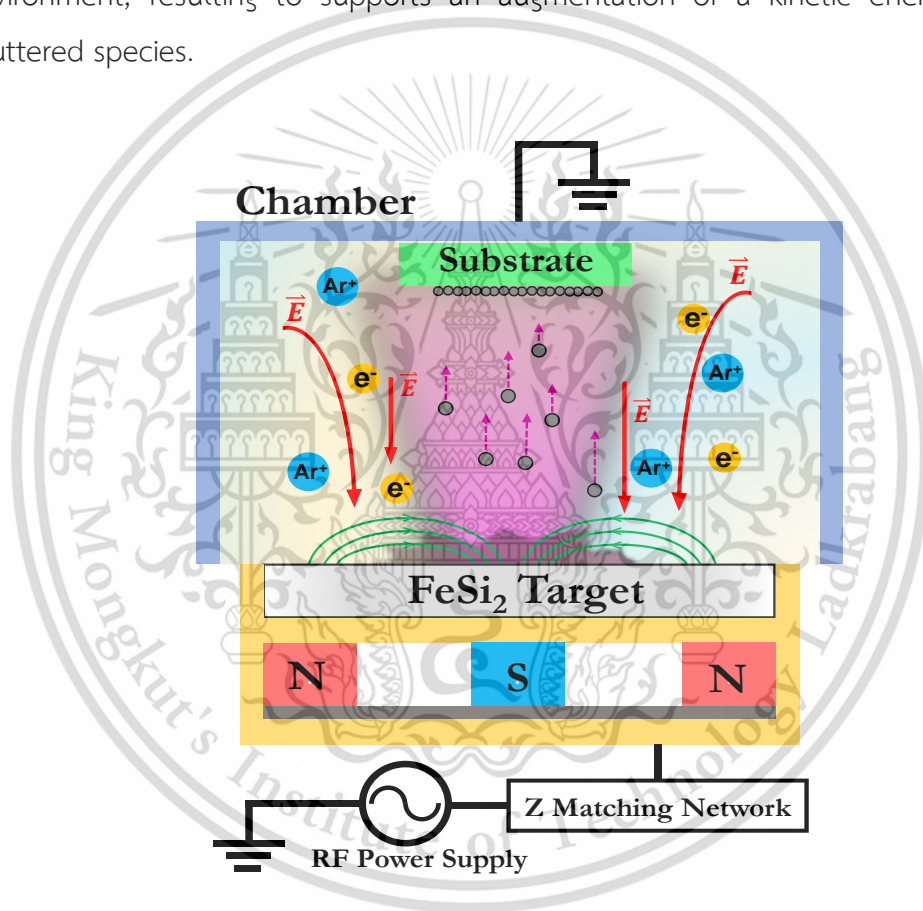


Figure 2.10 Schematic diagram for the fabrication technique of RFMS.

## 2.5 Advantages of $T_{sub}$ on thin film deposition [61]

In general, the films with a polycrystalline structure are well-known that they consisted of the crystallites located along with their boundaries, where their boundary considered to be as a disorder of defect formation, due to the incomplete bonding of their atomic. So that, the occurrence of the defect inside the film's structure are behaved themselves as a trap state, where the carrier can be trapped by this reason and can be led to a change of grain's orientation. The defect problems on the structural property can be diminished significantly by an alteration one of the deposition parameters such as  $T_{sub}$ . Through an increasing of  $T_{sub}$ , the grain's properties such as diameter, boundary and amount can be transformed into a better state. The grain diameter will be increased with a narrow boundary form. Moreover, the height of the potential barrier between the grains, as well as the exist amount of the boundary can be decreased by employing  $T_{sub}$ . From these reasons, the defect existed on the structure of thin film will be treated. The structure of the films will be consisted of a better lattice property and their electrical characteristic, including optical, will be improved as well.

## 2.6 Heat treatment [55]

Heat treatment is denoted as a post-deposition process which applying a heat source such as a furnace, flash lamp and laser source etc. A procedure of post-heating induced a difference of a coefficient of thermal expansion (CTEs) of the substrate and film, as well as different phase in the film, resulting to an occurrence of a stress among a film's structure. So that, when a stress occurred, this can generate a plastic deformation and interfacial fracture for the film and substrate. However, a post-deposition process utilizing heat or thermal treatment has the several important roles to perform an alteration of film's properties as well. This process, heat-treatment, can be employed to promote a diffusion of atoms for the films, which relates to an annealing of the residual stress and structural defect of films. Namely, a post-thermal process by heat can be performed to relieve an effect which came from the residual stress and defect concentration. There has been referred that post-thermal process has the benefits on the deposited films, for example, grain growth, phase changing and structural modification.

## 2.7 Influence of C-doping on $\beta$ -FeSi<sub>2</sub> films [23]

There had been previously reported on the effect of C-doping concentration on the  $\beta$ -FeSi<sub>2</sub> films prepared utilizing RFMS. The influence of element doping of C at different doping concentrations on the  $\beta$ -FeSi<sub>2</sub> films was reported through the research of M. Takahara et. al. The defects or imperfection of lattice properties for the  $\beta$ -FeSi<sub>2</sub> films were lessen by introducing of C element, due to the attractive properties for the C element. For C elements, this element flexibly forms chemical bonds with various elements, where the lattice or imperfection for the  $\beta$ -FeSi<sub>2</sub> films could be compensated by employing an integration with C atoms. As well, C element possesses a large electronegativity, which takes an advantage for attraction of those free electron of  $\beta$ -FeSi<sub>2</sub>. With these reasons, the dangling bonds for the  $\beta$ -FeSi<sub>2</sub>, including a defect of lattice, could be terminated, resulting to a decreasing of carrier density. Moreover, unless the structural and electrical characteristics, several research groups had been reported that the morphology for the based substance can be improved by C-doping. For the preparations,  $\beta$ -FeSi<sub>2</sub> with a doping of C could be achieved by a sputtering technique to the C-blended FeSi<sub>2</sub> alloy targets.

## 2.8 Characterization techniques [61-71]

This topic presents a basic principle of different characterization techniques to investigate film's properties related to this research.

### 2.8.1 X-ray diffraction

X-ray Diffraction (XRD) is a common characterization technique to examine crystal structure which relates to an X-ray source at single wavelength to inflate the crystal of the coated layer, which can be a single crystal or a polycrystal formation. Various structural information can be clarified using XRD such as crystal structure, atomic spacing and crystalline diameter etc. In general, for XRD, the X-ray were generated in a cathode ray tube during a heated filament, where the electrons were generated. Then, the generated electrons are bombard to a specimen or a sample under an applied voltage. From that, the electrons from an inner shell could be ejected from the sample, in a case of the incident electrons having an adequate energy. This produces an interaction between the X-ray photons and the measured sample, resulting the absorption and scattering effects relate to Bragg's Law as below:

This material is reserved for educational use only, not allowed for commercial use.  
Forbidden to modify the content, and cite the document when use.

$$n\lambda = 2d\sin(\theta) \quad (2.1)$$

where  $n$  is an integer,  $\lambda$  is a wavelength of the radiation source,  $d$  is an interplanar spacing generating the diffraction and  $\theta$  is a diffraction angle.

The detector was utilized to gather the characteristic of the X-ray spectra, which stepped along the preferred angular range as displayed in Figure 2.11. The crystallite's diameter ( $D$ ) could be estimated from the gathered spectra by utilizing Scherrer's equation, which considered at the most intense peak's position. According to Scherrer's equation,  $D$  could be evaluated by this following formular:

$$D = \frac{0.9\lambda}{(FWHM)(\cos\theta)} \quad (2.2)$$

where  $\lambda$  is a wavelength of the X-ray source, FWHM is a full width at half maximum of the peak in radian,  $\theta$  is a diffraction angle.

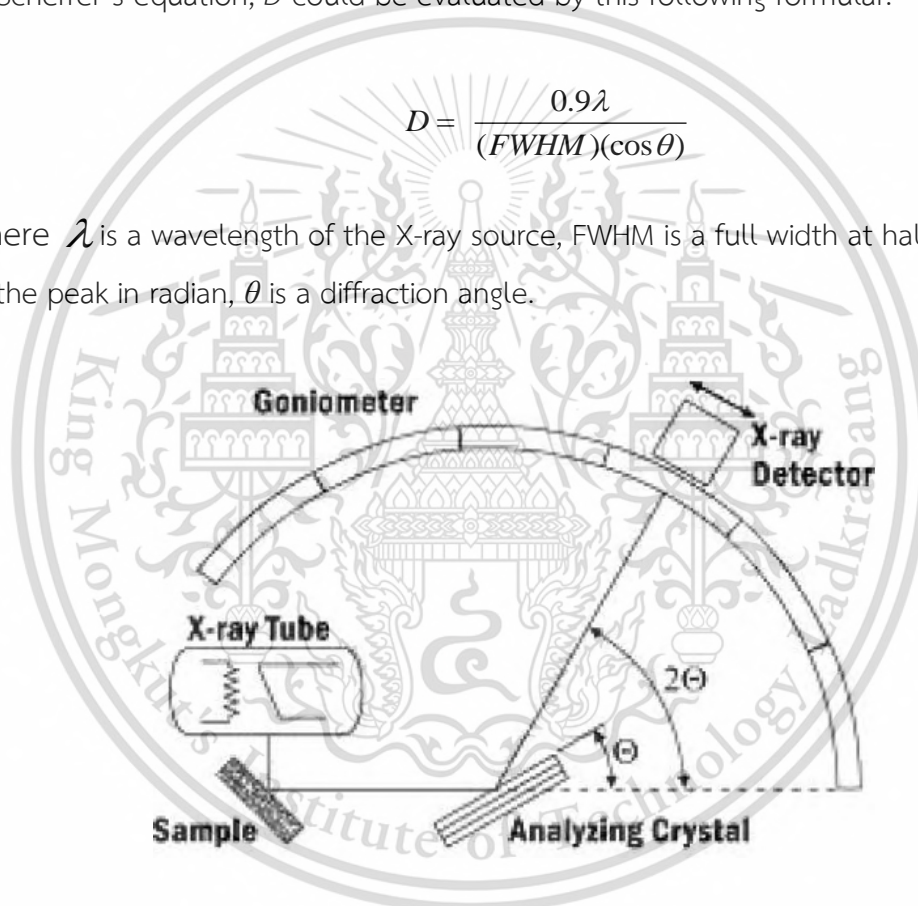


Figure 2.11 Diagram for XRD technique. [63]

### 2.8.2 Raman spectroscopy

Raman spectroscopy is a spectroscopic procedure utilized to observe the vibrational and rotational behaviors in a material science. This instrument employs an effect of Raman scattering between an incident wavelength and phonons in the system of material, which relies on the changing of polarizability among the bond during their phonon motion. Raman effect is an inelastic scattering of the photons due to the

reason of the vibrational-induced phonon mode, which results the up or down shifting of an incident wavelength. Generally, the incident wavelength utilized for Raman spectroscopy was a monochromatic light source for stimulation, which is commonly a laser beam. Figure 2.12 provides a schematic diagram for Raman spectroscopy. The laser beam is illuminated toward a sample by monochromator, to inspect a Raman spectrum of the sample. The dispersed wavelength is collected through a detector, where the wavelengths that closes to the laser line are filtered out.

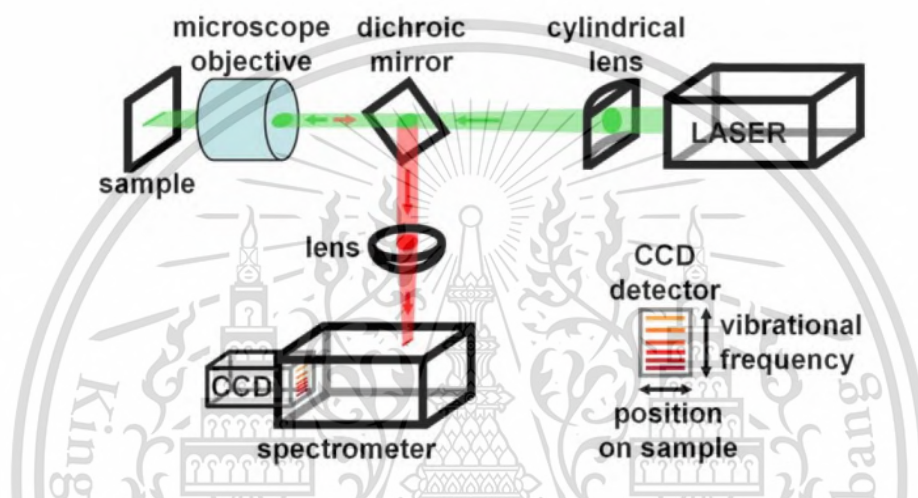


Figure 2.12 Schematic 2D diagram for Raman spectroscopy. [64]

### 2.8.3 Scanning electron microscope

Scanning electron microscope (SEM) is a scientific instrument which is employed to study the surface morphology of the samples at a high ranging of magnification. For SEM, this instrument employs an electron to hit the atoms of the specimen, where the scattered electron led to a production of the backscattered and secondary electrons. The electrons had a potential to transmitted toward specimen in case of the electrons consisting of a sufficient energy to strike the inner shell's electron. Then, the excited atom may relax with the liberation of Auger electrons or X-ray photons. Figure 2.13 illustrates a 2D-diagram for SEM. The electron beam is incident toward a sample through electromagnetic deflection coils, to scan the surface plane. Then, the scanned signal was mapped from each scanning point, where the scanning signal was detected and displayed onto the monitor.

This material is reserved for educational use only, not allowed for commercial use.  
Forbidden to modify the content, and cite the document when use.

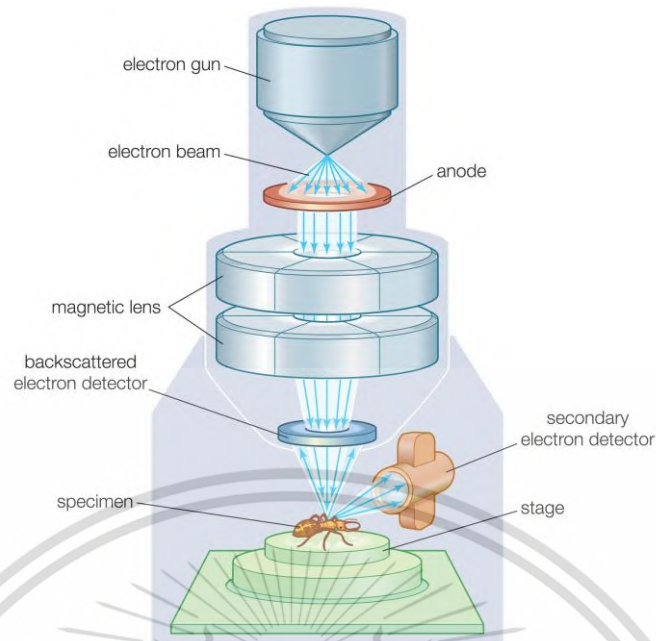


Figure 2.13 2D-diagram for SEM equipment. [65]

#### 2.8.4 Atomic force microscopy

An atomic force microscopy (AFM) is a technique for analyzing the physical properties of the sample surface at a nanometer scale, which uses a force in angstrom-scale for observation. Various properties could be achieved by utilizing an AFM technique such as morphological, mechanical and electrical properties of the measured sample. For AFM, the observation by this technique ordinarily applies a scanning probe over the scanning area. The scanning probe for AFM technique appears in a cantilever shape, which usually made of Si. The cantilever is mounted with a spring with a spring constant of less than the atom-atom bonding. The scanning probe is attractively deflected to a van der Waals force and repulsed to the surface. For imaging, the cantilever with a nano-scale radius of tip was dragged along the scanning path, where the backside for the cantilever was focused by a laser diode. Then, photodetector is applied to detect the deflection of the incident laser beam, which projected to the backside of the cantilever, by tracking a beam's position. The contact force between the cantilever's tip and the sample is maintained through a piezoceramic scanner, which is controlled by an electronic feedback loop voltage. The operating condition for AFM technique can be regularly performed in three modes of

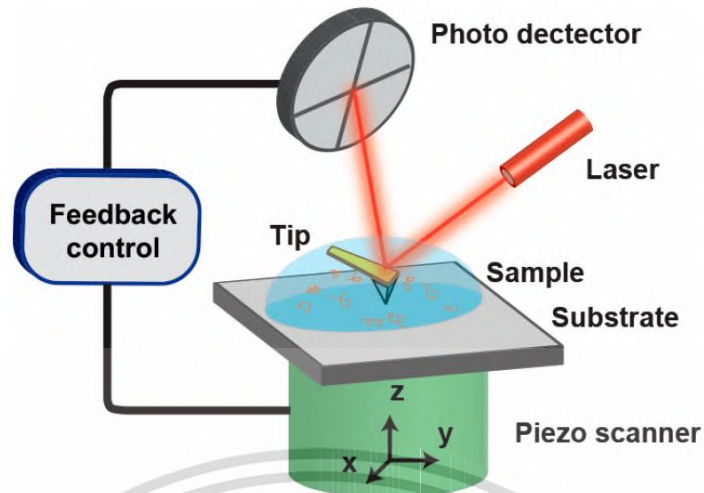


Figure 2.14 Diagram for general AFM apparatus. [66]

### 2.8.5 Contact angle measurement

Contact angle (CA) measurement is a technique to study the hydrophobic and hydrophilic properties of sample surface by a dripping of a probe liquid such as water, alcohol and oil, including the polar and non-polar liquids. By dripping a solution, a wetting angle over the surface can be determined. It can be applied in research such as performance analysis of water repellent, automotive glass, building film, etc. CA measurement is easily performed by establishing the tangent angle of a liquid droplet onto the solid surface. The possibility of estimating solid surface tensions from contact angles relies on a relation of Young's equation as below :

$$\gamma_{sv} = \gamma_{sl} + \gamma_{lv} \cos\theta \quad (2.3)$$

where the  $\gamma$  denotes to the surface tension referred between the interface of (i) solid to vapor "sv", (ii) solid to liquid "sl", and liquid to vapor "lv".

Specifically, the wetting characteristic for the solid-surfaces could be determined by their average contact angle ( $\theta_{CA}$ ) between the probe liquid and surface. Specifically, the wetting state could be categorized into four main types based on the  $\theta_{CA}$ , as a superhydrophobic ( $150^\circ \leq \theta_{CA} \leq 180^\circ$ ), hydrophobic ( $90^\circ \leq \theta_{CA} < 150^\circ$ ), hydrophilic ( $10^\circ \leq \theta_{CA} < 90^\circ$ ) and superhydrophilic ( $\theta_{CA} < 10^\circ$ ) [35-38]. Hence, the repellent and adhesive ability over the surface could be determined from these ranges,

where the higher  $\theta_{CA}$  indicated a high repellence and low adhesiveness of the surface. The wetting behavior in general terms for the solid surface is revealed in Figure 2.15.

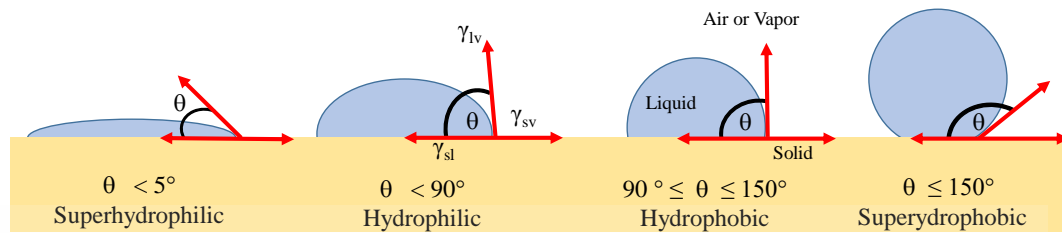


**Figure 2.15** Schematic diagram for the general wetting state on the solid surface substrate at different ranging of CA.

### 2.8.6 Nanoindentation

Nanoindentation is a technique to study the mechanical property of the sample by applying an indentation at a micro- or nanoscale. This method could be utilized to evaluate a hardness, elasticity, stiffness and adhesion force of a variety of materials. Nanoindentation testing allows mechanical probing of film specimens having characteristic dimensions that are typically  $1 \mu\text{m}^2$  in size. The testing is accomplished with the indenter by load-controlled submicron indentation instrument. Figure 2.16 presents the diagram for a nanoindentation components. The positioning of stage was controlled on the x-y-z axis, using a precision piezoelectric stack. The indenter tip was penetrated toward a sample's surface by a force and displacement controller sensors. The diamond indenter with a Berkovich shape possessing a three-sided pyramidal geometry is most frequently employed. Load is applied with a coil and magnet assembly while displacement is usually measured by capacitance sensors.

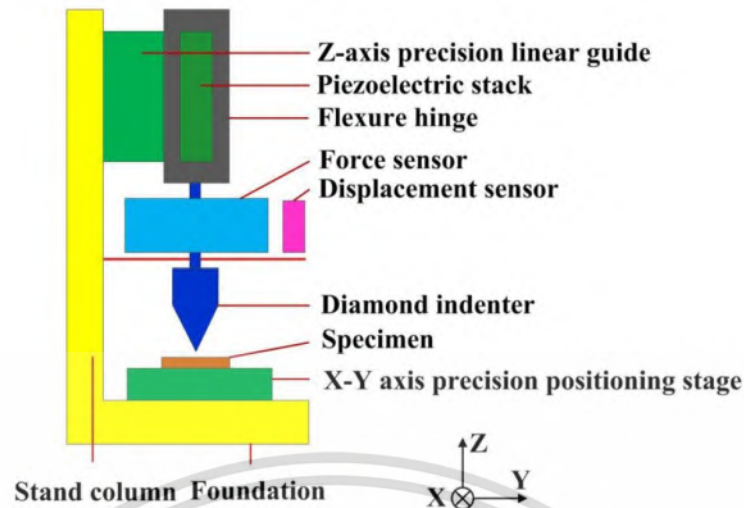


Figure 2.16 Schematic diagram for a nanoindentation apparatus. [71]

## 2.9 Related research [16,21,72]

In this topic, the related research on the effect of  $T_{\text{sub}}$ ,  $T_{\text{ann}}$  and C-doping concentrations were demonstrated. The research that related to the properties of thin films regarding thermal processes of  $T_{\text{sub}}$  and  $T_{\text{ann}}$ , including C-doping concentrations, were presented in this topic.

### 2.9.1 Influences of $T_{\text{sub}}$ and $T_{\text{ann}}$ on thin film's properties

The increasing of the  $T_{\text{sub}}$  and  $T_{\text{ann}}$  could lead to a rise of the adatom mobility, which caused an agglomeration in the structure and developed the structure and surface roughness. The changing of these two properties could affect the wetting and mechanical properties. In this section, the related research based on the effect of  $T_{\text{sub}}$  and  $T_{\text{ann}}$  were presented.

B.G. Priyadarshini et. al [16] reported on an effect of  $T_{\text{sub}}$  on the structure and surface for the alloy films of nickel (Ni) thin films. The Ni films were sputtered onto Si(111) substrates via RF- and DC-magnetron sputtering at 30 °C, 300 °C and 500 °C. The structure for the deposited films was investigated that the as-deposited Ni films showed an improvement grain's diameter, including an increasing of surface roughness at higher  $T_{\text{sub}}$ . The roughness for the as-deposited Ni films held a roughness of 3.85 nm, which was altered to 10.00 and 23.00 nm the temperatures of 300 °C and 500 °C, respectively.

This material is reserved for educational use only, not allowed for commercial use.  
Forbidden to modify the content, and cite the document when use.

B.G. Priyadarshini et. al also reported the influence of  $T_{\text{ann}}$  of their films, where the as-deposited films were annealed at 300 °C and 500 °C. The film's roughness was increased to 5.42 nm and 7.14 nm after annealing at  $T_{\text{ann}}$  of 300 °C and 500 °C, respectively.

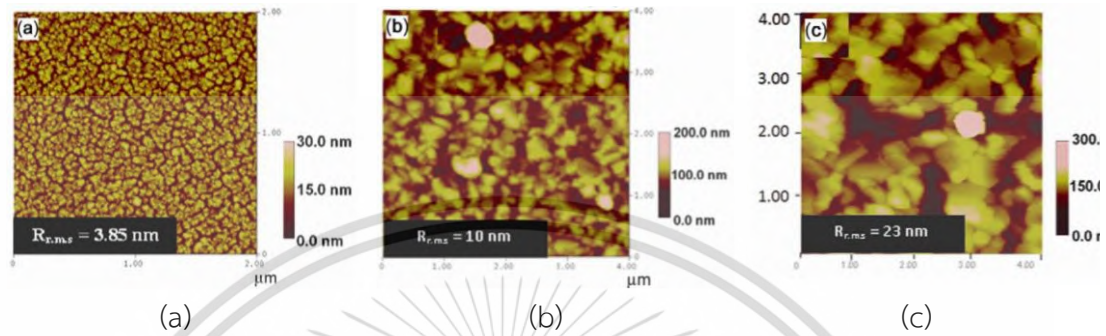


Figure 2.17 AFM images for as-prepared Ni films at (a) 30 °C (b) 300 °C and (c) 500 °C. [16]

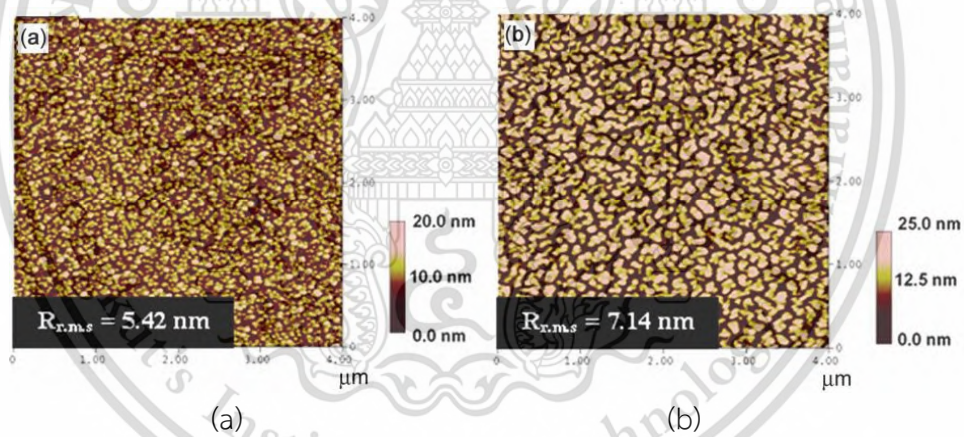


Figure 2.18 AFM images for Ni films after annealing at (a) 300 °C and (b) 500 °C. [16]

Further, L. Yang et.al. [72] reported an impact of  $T_{\text{ann}}$  on wettability of  $\text{TiO}_2$  nanotube array (TN) films. The TN films were annealed in air under different  $T_{\text{ann}}$  ranging of 200 °C to 800 °C. The results were reported that the as-deposited films exhibited the change of surface and wetting angle with a higher applying temperature. The surface for the as-deposited films altered to a cluster formation, while the CA was changed from 130.00° to 77.00°.

This material is reserved for educational use only, not allowed for commercial use.  
Forbidden to modify the content, and cite the document when use.

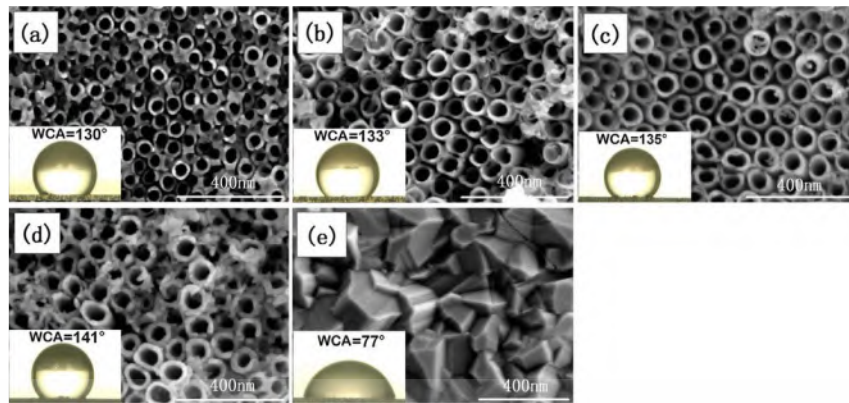


Figure 2.19 The change of surface and wetting angles of TN films at different  $T_{\text{ann}}$ .

### 2.9.2 Influences of C-doping on thin film's properties

X.-N. Li et. al [16] conducted the research related to the microstructures of  $\beta\text{-FeSi}_2$  and C-doped  $\beta\text{-Fe(C,Si)}_2$  films. They reported that the structure and morphology for the undoped sample had significant changes after C-doping. The grain size for C-doped films, with 1% doped ratio of C/Fe, was observed to be smaller than the case of the undoped films. The surface for the C-doped samples exhibited more homogeneous and smoother than that of undoped samples.



Figure 2.20 Plane surface views for the  $\beta\text{-FeSi}_2$  films formed via ion implantation in case of (a) without C-doping and (b) with C-doping. [16]

## Chapter 3

### Research methodology

This chapter describes the fabrication details of  $\beta$ - and NC-FeSi<sub>2</sub> films to research the effects of  $T_{\text{sub}}$ ,  $T_{\text{ann}}$  and C-doping concentrations on surface morphological, wetting and mechanical characteristics. The first topic details a cleansing procedure for the Si substrate. Second, the fabrication and annealing conditions for the as-formed  $\beta$ -FeSi<sub>2</sub> films via FTDCS were presented. Third section provides the fabrication conditions of  $\beta$ -FeSi<sub>2</sub> films via RFMS at varied  $T_{\text{sub}}$ . Fourth, the fabrication and annealing conditions for the NC-FeSi<sub>2</sub> films were detailed. Fifth, the fabrication details for the undoped and C-doped  $\beta$ -FeSi<sub>2</sub> films were provided. The last section introduced the characterization techniques to investigate the properties for all films. The formation of  $\beta$ - and NC-FeSi<sub>2</sub> films was performed via FTDCS and RFMS systems by Asst.Prof.Dr. Nathaporn Promros and master's degree students at Kyushu University, Japan. Figure 3.1 presents FTDCS and RFMS systems utilized in this research.



Figure 3.1 (a) FTDCS and (b) RFMS systems for sample preparation.

### 3.1 Cleansing procedure for the Si substrates

The Si substrates with an orientation of (111) were cleaned by rinsing in the solvents of acetone, methanol, and deionized (DI) water using an ultrasonic bath. Then, the substrates were applied into a diluted hydrofluoric (HF) acid (concentration of 1%) to expel a native oxide layer. After applying the HF acid, the Si substrate was cleaned and dried by using DI water and nitrogen (N) gas, respectively.

### 3.2 Fabrication process for unannealed $\beta$ -FeSi<sub>2</sub> sample via FTDCS

The details for fabrication  $\beta$ -FeSi<sub>2</sub> films via FTDCS system, including annealing conditions were presented in this topic.  $\beta$ -FeSi<sub>2</sub> films were formed via FTDCS at a  $T_{\text{sub}}$  of 600 °C and then annealed at  $T_{\text{ann}}$  from 200 to 600 °C, to study the effect of  $T_{\text{ann}}$  on their properties. It was expected that the surface, wetting and mechanical properties for the as-deposited  $\beta$ -FeSi<sub>2</sub> films will modified after annealing. Namely, the atoms will earn higher diffusion energy and allow to transfer in crystal lattice by providing an additional temperature during annealing, which will modify the surface arrangement, roughness, wetting and mechanical features.

The cleaned Si substrates were transferred into the sputtering chamber in order to fabricate  $\beta$ -FeSi<sub>2</sub> films. The based pressure was evacuated and kept at  $3 \times 10^{-5}$  Pa by using the dual vacuum systems of rotary and turbomolecular pumps. Then, the chamber was fed by argon (Ar) gas at feeding rate of 15 sccm, while the pressure was controlled to be  $1.33 \times 10^{-1}$  Pa. Subsequently, the  $\beta$ -FeSi<sub>2</sub> films were fabricated to the Si substrate at a controlled  $T_{\text{sub}}$  of 600 °C under 1 kV and 1.5 mA of the applying voltage and current. The fabrication condition for the FeSi<sub>2</sub> films via FTDCS for annealing at different  $T_{\text{ann}}$  was demonstrated in Table. 3.1.

**Table 3.1** Fabrication details for  $\beta$ -FeSi<sub>2</sub> films via FTDCS before annealing.

<b>Substrate</b>	Si(111)
<b>Target</b>	FeSi <sub>2</sub>
<b>T<sub>sub</sub></b>	600 °C
<b>Base pressure</b>	$3 \times 10^{-5}$ Pa
<b>Ar gas flow rate</b>	15 sccm
<b>Sputtering pressure</b>	$1.33 \times 10^{-1}$ Pa
<b>Voltage</b>	1 kV
<b>Current</b>	1.5 mA

### 3.2.1 Annealing procedure

The as-formed  $\beta$ -FeSi<sub>2</sub> films at T<sub>sub</sub> of 600 °C were divided for annealing at T<sub>ann</sub> of 200 °C, 400 °C, and 600 °C, respectively. The annealing process was conducted at Photonics Technology Laboratory (PTL), National Electronics and Computer Technology Center (NECTEC), Thailand. Figure 3.2 presents the annealing apparatus for annealing the as-prepared  $\beta$ -FeSi<sub>2</sub> samples. The divided  $\beta$ -FeSi<sub>2</sub> samples were located onto the semi-cylinder quartz with a shape, then transferred into an annealing system. The pressure inside the quartz tube was evacuated by utilizing rotary and turbomolecular pumps to less than  $5 \times 10^{-6}$  mbar. Later, the heating system was applied to heat the quartz tube for annealing the  $\beta$ -FeSi<sub>2</sub> samples. The heating process was conducted utilizing a temperature controller (Shimaden, model SR53). The pre-heat temperature was kept at 40 °C for 10 minutes, then increased for 20 °C until it reached the desired T<sub>sub</sub> of 200 °C, 400 °C and 600 °C. Each sample was annealed for for 2 hours. The annealing condition for the  $\beta$ -FeSi<sub>2</sub> films prepared via FTDCS were provided in Table 3.2.

**Table 3.2** Annealing conditions for the  $\beta$ -FeSi<sub>2</sub> films formed via FTDCS.

<b>Samples</b>	<b>Pressure (mbar)</b>	<b>T<sub>ann</sub> (°C)</b>	<b>Annealing time (hours)</b>
As-formed $\beta$ -FeSi <sub>2</sub>	-	-	-
Annealed $\beta$ -FeSi <sub>2</sub>	$< 5 \times 10^{-6}$	200	2
Annealed $\beta$ -FeSi <sub>2</sub>	$< 5 \times 10^{-6}$	400	2
Annealed $\beta$ -FeSi <sub>2</sub>	$< 5 \times 10^{-6}$	600	2



**Figure 3.2** Thermal annealing apparatus for annealing of the as-prepared  $\beta$ -FeSi<sub>2</sub> samples at different  $T_{\text{ann}}$  of 200 °C, 400 °C and 600 °C.

### 3.3 Preparation of $\beta$ -FeSi<sub>2</sub> samples via RFMS at different $T_{\text{sub}}$

This section presents a fabrication of  $\beta$ -FeSi<sub>2</sub> films via RFMS by elevation of  $T_{\text{sub}}$ , 500 °C to 600 °C, in order to study the effect of  $T_{\text{sub}}$  on surface and wetting properties of  $\beta$ -FeSi<sub>2</sub>. By increasing of  $T_{\text{sub}}$ , the migration rate of adatoms on the substrate surface increased and caused the additional energy in the adatoms aside from the kinetic energy [15,16], which affected the conglomeration of grains to form into a larger size, including an increase of surface  $R_{\text{rms}}$ . It was expected that the  $\beta$ -FeSi<sub>2</sub> films will express an enhancement of  $\theta_{\text{CA}}$  by increasing of  $T_{\text{sub}}$ .

The cleaned Si(111) substrates were applied in RFMS system to deposit the  $\beta$ -FeSi<sub>2</sub> samples at different  $T_{\text{sub}}$ . The alloy target of FeSi<sub>2</sub> (Toshima Manufacturing Co. Ltd.) with 4N of purity was provided as a sputtering target. The internal pressure of the RFMS chamber was kept at lower than  $1 \times 10^{-5}$  Pa, using the rotary pump (Ulvac, model VD301) and turbomolecular pump (Mitsubishi Sinchoon, model FT-800W). Latterly, a sputtering gas of Ar (purity 4N; Iwatani Corp.) was supplied with a 15 sccm of flow rate, which was controlled by an Ar flow indicator (Kofloc, model DPM-3). Then, the inside pressure was preserved at  $2.66 \times 10^{-1}$  Pa throughout the process. The  $T_{\text{sub}}$  of the RFMS system was controlled at temperatures of 500 °C, 560 °C, and 600 °C through a temperature controller (Yokogawa, model UT150). To fabricate the  $\beta$ -FeSi<sub>2</sub> films, a sputtering power of 20 W was powered by an RF power generator (Dressler Cesar RF Power Generator, model Cesar-133) with an automatic matching controller

(Astech, model TH-10R). The condition for  $\beta$ -FeSi<sub>2</sub> films preparation under different  $T_{\text{sub}}$  via RFMS system was summarized in Table 3.3.

**Table 3.3** Fabrication details for  $\beta$ -FeSi<sub>2</sub> films by RFMS at varied  $T_{\text{sub}}$ .

Substrate	Si (111)
Target	FeSi <sub>2</sub>
$T_{\text{sub}}$	500 °C, 560 °C and 600 °C
Base pressure	$< 1.00 \times 10^{-5}$ Pa
Ar gas flow rate	15 sccm
Sputtering pressure	$2.66 \times 10^{-1}$ Pa
Sputtering power	20 W

### 3.4 Fabrication process for unannealed NC-FeSi<sub>2</sub> sample via RFMS

This section provides the fabrication and annealing conditions for NC-FeSi<sub>2</sub> films. The as-deposited NC-FeSi<sub>2</sub> films were formed at RT of  $T_{\text{sub}}$  and then annealed at varied  $T_{\text{ann}}$  of 100 °C to 500 °C under air-ambience. It was aimed that the surface and wetting properties for the as-deposited NC-FeSi<sub>2</sub> will exhibit the changes in roughness and wetting angle after annealing. Namely, the adatoms over the NC-FeSi<sub>2</sub> films will gain higher diffusion energy and increase nucleation density after annealing [15-19]. So that, the annealed NC-FeSi<sub>2</sub> films will exhibit the alterations of surface formation and surface roughness, which also affect to their wetting angle.

Si substrates were introduced to the chamber of RFMS systems to prepare the NC-FeSi<sub>2</sub> films.  $T_{\text{sub}}$  for the preparation of NC-FeSi<sub>2</sub> films in this topic was applied at RT. The based pressure was provided at  $3 \times 10^{-5}$  Pa by using the rotary and turbomolecular co-pumping systems. Then, the Ar gas with 4N of purity was introduced to the chamber with a feeding rate of 15 sccm, where the pressure was provided at  $2.66 \times 10^{-1}$  Pa. The RF power source was generated to sputter the NC-FeSi<sub>2</sub> films at a power of 20 W. The fabrication condition for the NC-FeSi<sub>2</sub> films via RFMS for annealing at different  $T_{\text{ann}}$  is presented in Table 3.4.

**Table 3.4** Fabrication condition for NC-FeSi<sub>2</sub> films via RFMS before annealing.

Substrate	Si(111)
Target of sputtering	FeSi <sub>2</sub>
T <sub>sub</sub>	RT
Base pressure	3 × 10 <sup>-5</sup> Pa
Ar gas flow rate	15 sccm
Sputtering pressure	2.66 × 10 <sup>-1</sup> Pa
Sputtering power	20 W

### 3.4.1 Annealing procedure

The annealing process for the as-deposited NC-FeSi<sub>2</sub> films was conducted by a thermal furnace at Faculty of Science, King Mongkut's Institute of Technology Ladkrabang. Figure 3.3 displays a thermal furnace for annealing process of the as-prepared NC-FeSi<sub>2</sub> films via RFMS. The NC-FeSi<sub>2</sub> films were separated for annealing at 100 °C, 300 °C, and 500 °C under air-ambient for 2 hours. After a separation, each NC-FeSi<sub>2</sub> sample was placed on the crucible and then transferred into the thermal furnace for annealing under their temperature conditions. The T<sub>ann</sub> was controlled by a programmable temperature controller (TAEI, model PFU96). The temperature was kept at 40 °C to pre-heat the NC-FeSi<sub>2</sub> films. Then, the temperature was rose until it reached the set temperature ranges of 100 °C, 300 °C, and 500 °C. Then, the annealed NC-FeSi<sub>2</sub> films were cooled down until the temperature reached into RT. The annealing condition in this topic was presented as Table 3.5.

**Table 3.5** Annealing conditions for the as-prepared NC-FeSi<sub>2</sub> films via RFMS.

Samples	Ambient	T <sub>ann</sub> (°C)	Annealing time (hours)
As-prepared NC-FeSi <sub>2</sub>	-	-	-
Annealed NC-FeSi <sub>2</sub>	air	100	2
Annealed NC-FeSi <sub>2</sub>	air	300	2
Annealed NC-FeSi <sub>2</sub>	air	500	2

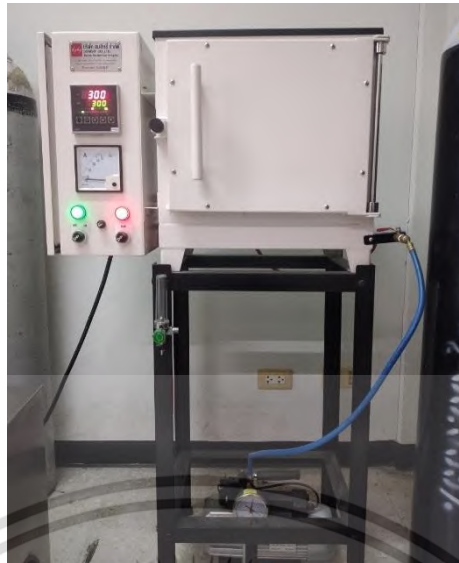


Figure 3.3 Annealing furnace for the as-prepared NC-FeSi<sub>2</sub> films.

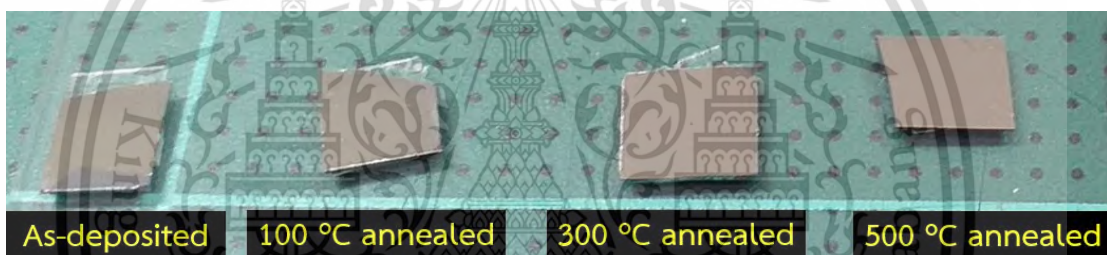


Figure 3.4 The as-deposited and annealed NC-FeSi<sub>2</sub> films at different  $T_{\text{ann}}$  of 100 °C, 300 °C and 500 °C

### 3.5 Preparation of undoped and C-doped $\beta$ -FeSi<sub>2</sub> films via RFMS

This topic presents a forming of  $\beta$ -FeSi<sub>2</sub> films via RFMS by using the undoped and C-doped FeSi<sub>2</sub> targets with various C-doping concentrations to study the effect of C-doping concentrations on the properties of  $\beta$ -FeSi<sub>2</sub> films. C dopant will modify the structure and surface properties of  $\beta$ -FeSi<sub>2</sub> films, due to an incorporation between the C atoms and Fe-Fe bonding of  $\beta$ -FeSi<sub>2</sub>. Moreover, C dopant could lead a hindrance of grain growth and induces a finer surface of  $\beta$ -FeSi<sub>2</sub> [21,22]. So that, the changing of structure and surface features is expected to modify the wetting property of the surface of  $\beta$ -FeSi<sub>2</sub> films as well.

$\beta$ -FeSi<sub>2</sub> films were formed on Si substrates via RFMS at  $T_{\text{sub}}$  of 560 °C by using the FeSi<sub>2</sub> targets with different C-doping concentrations of undoped, 0.5 at.%, 1.0 at.%

This material is reserved for educational purposes only, not allowed for commercial use. Forbidden to modify the content, and cite the document when use.

and 3.0 at.%, respectively. The based pressure was adjusted to  $3.00 \times 10^{-5}$  Pa using a rotary and turbomolecular pump. After that, Ar gas was fed into the system with a feeding rate of 15 sccm, where the sputtering pressure was adjusted to  $2.66 \times 10^{-1}$  Pa. Then, the  $\beta$ -FeSi<sub>2</sub> films were sputtered on the surface plane of Si substrate using an applied sputtering power of 20 W. Table 3.6 provides the fabrication for the undoped and C-doped  $\beta$ -FeSi<sub>2</sub> films via RFMS.

**Table 3.6** Fabrication condition for the undoped and C-doped  $\beta$ -FeSi<sub>2</sub> films via RFMS at different C-doping concentrations.

Substrate	Si(111)
Target	Undoped FeSi <sub>2</sub> and C-doped FeSi <sub>2</sub> at 0.5 at.%, 1.0 at.%, and 3.0 at.%
T <sub>sub</sub>	560 °C
Base pressure	$3 \times 10^{-5}$ Pa
Ar gas flow rate	15 sccm
Sputtering pressure	$2.66 \times 10^{-1}$ Pa
Sputtering power	20 W

### 3.6 Investigation techniques

To investigate the characteristic, several characterization techniques were employed to evaluate the structural, surface morphological, wetting and mechanical properties for the prepared  $\beta$ - and NC-FeSi<sub>2</sub> films under their research topics. The details for each equipment were described as below.

#### 3.6.1 Structural investigation

The effect of T<sub>sub</sub>, T<sub>ann</sub> and C-doping concentrations on the structural property was investigated by utilizing an X-ray diffractometer (Rigaku, model TTRAX III) and a dispersive Raman spectroscopy (Bruker, model Senterra II). The X-ray diffraction (XRD) patterns for all prepared FeSi<sub>2</sub> films were inspected by using a CuK $\alpha$  source with the X-ray wavelength of 1.542 Å under RT. Figure 3.5 presents the X-ray diffractometer (Rigaku, model TTRAX III) at The National Metal and Materials Technology Center (MTEC), Thailand.



Figure 3.5 XRD diffractometer (Rigaku, model TTRAX III).

The Raman spectra for the  $\text{FeSi}_2$  films prepared at different  $T_{\text{sub}}$ ,  $T_{\text{ann}}$  and C-doping concentrations were evaluated by a dispersive Raman spectroscopy at Synchrotron Light Research Institute, Thailand. An excitation laser of 532 nm at 25 mW with a 25  $\mu\text{m}$  of detector aperture was employed to extract the Raman line for all  $\text{FeSi}_2$  samples. Figure 3.6 provides an image of a Raman spectroscopy for determination of the Raman spectra for all prepared  $\text{FeSi}_2$  films at different  $T_{\text{sub}}$ ,  $T_{\text{ann}}$  and C-doping concentrations.

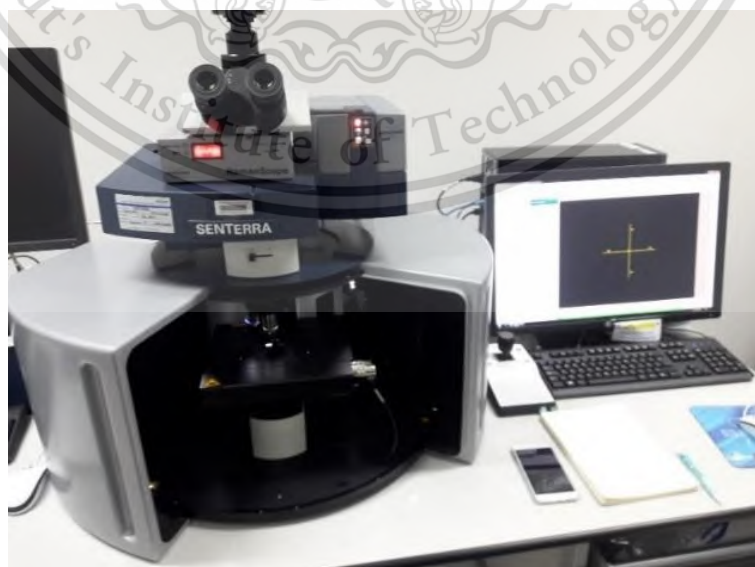


Figure 3.6 Dispersive Raman spectroscopy (Bruker, model SENTERRA II).

### 3.6.2 Morphology investigation

The surface morphology for all  $\beta$ -FeSi<sub>2</sub> and NC-FeSi<sub>2</sub> films was investigated through a field emission scanning electron microscope (FESEM; Zeiss, model Auriga) at The Center for Scientific and Technological Equipment, Facility Building 11, Suranaree University of Technology and scanning electron microscope (Hitachi, model SU8230) at NSTDA Characterization and Testing Service Center (NCTC).



Figure 3.7 FESEM apparatus (Zeiss, model Auriga).



Figure 3.8 Scanning electron microscope (Hitachi, model SU8230).  
This material is reserved for educational use only, not allowed for commercial use.  
Forbidden to modify the content, and cite the document when use.

The surface roughness for all  $\beta$ - and NC-FeSi<sub>2</sub> samples, prepared at different  $T_{\text{sub}}$ ,  $T_{\text{ann}}$  and C-doping concentrations, was provided by using an atomic force microscope (AFM; Park systems, model XE-120). The film's surface was scanned using a non-contact scanning mode within a scanning area of 25  $\mu\text{m}^2$ . The root mean square roughness ( $R_{\text{rms}}$ ) was extracted by utilizing XEI software. Figure 3.9 presents an AFM apparatus at The Center for Scientific and Technological Equipment, Facility Building 11, Suranaree University of Technology.

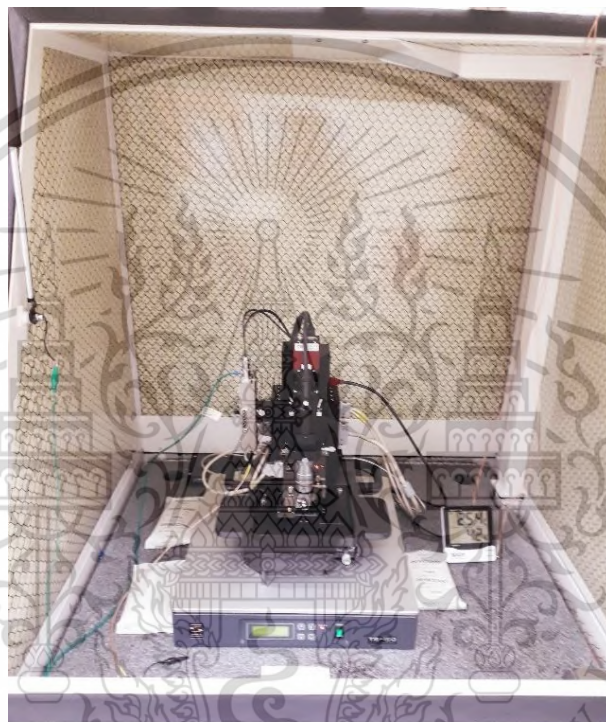


Figure 3.9 AFM apparatus (Park system, XE-120).

### 3.6.3 Wetting angle investigation

The wetting angle for the surface of the  $\beta$ - and NC-FeSi<sub>2</sub> films, prepared at different  $T_{\text{sub}}$ ,  $T_{\text{ann}}$  and C-doping concentrations, was investigated by utilizing a optical contact angle measurement (Dataphysics, model OCA 20) at Scientific Instruments Center, Faculty of Science, King Mongkut's Institute of Technology Ladkrabange, as represented in Figure 3.10. For this measurement, DI water was dripped onto the surface of each FeSi<sub>2</sub> sample with a volumn of 5  $\mu\text{l}$  and a dosing rate of 1  $\mu\text{l/s}$ . The wetting angle was captured by a camera with a 20 kx of magnitude, where the  $\theta_{\text{CA}}$  was evaluated from SCA 20 software.

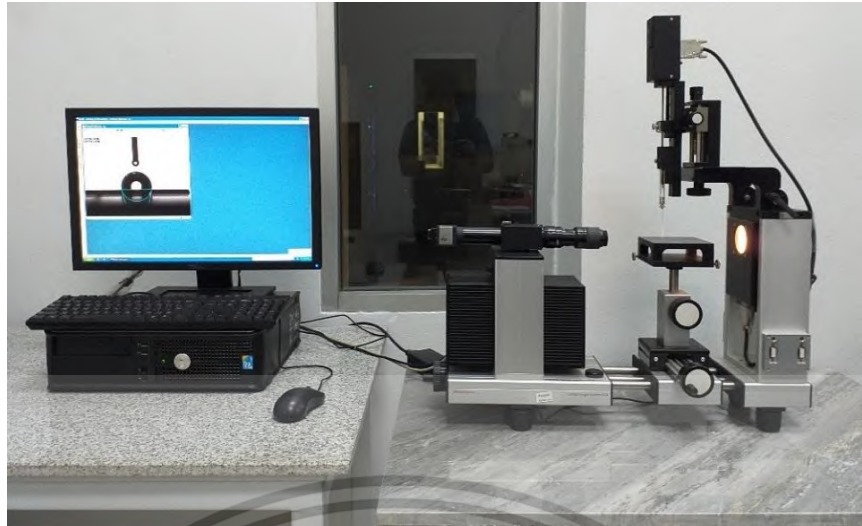


Figure 3.10 Contact angle analyzer (Dataphysics, model OCA 20) and a display monitor.



Figure 3.11 DI water droplet on the film's surface in (a) normal view and (b) view on the monitor with an estimation of contact angle values.

#### 3.6.4 Mechanical investigation

The mechanical property for the surface of  $\beta$ -FeSi<sub>2</sub> films prepared at different  $T_{\text{ann}}$  was investigated at The Center for Scientific and Technological Equipment, Facility Building 10, Suranaree University of Technology through the nanoindentation test (Micromaterial, model Nanotest Vantage) using Berkovich indenter, as depicted in Figure 3.12.

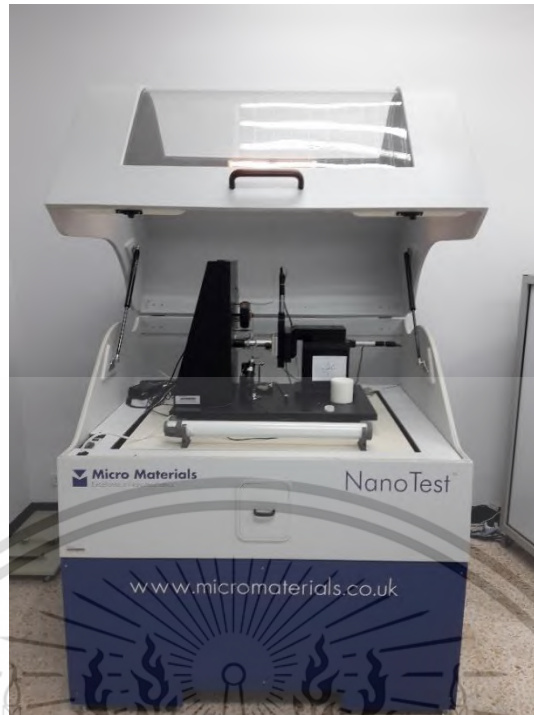


Figure 3.12 Nanoindentation apparatus (Micromaterial, model Nanotest Vantage).

### 3.6.5 Optical investigation

Figure 3.13 presents an ultraviolet-visible-NIR spectrophotometer (Jasco, model V-570). This spectrophotometer was utilized to investigate the transmittance spectra for the undoped and C-doped  $\beta$ -FeSi<sub>2</sub> films. The transmittance spectra for the undoped and C-doped  $\beta$ -FeSi<sub>2</sub> films were evaluated under 200 to 2200 nm.



Figure 3.13 Ultraviolet-visible-NIR spectrophotometer (Jasco, model V570).  
Forbidden to modify the content, and cite the document when use.

## Chapter 4

# Results and discussion

This chapter describes the experimental results of surface morphological, structural, and wetting properties for FeSi<sub>2</sub> films prepared under the variations of depositions of T<sub>sub</sub>, T<sub>ann</sub> and C-doping concentrations. The results will be presented under three main topics of (i) effect of T<sub>sub</sub>, (ii) effect of T<sub>ann</sub> and (iii) effect of C-doping concentrations, respectively. The results and discussion under the chapter will be discussed in 4 topics as:

1. Effect of T<sub>ann</sub> on the characteristics of β-FeSi<sub>2</sub> films prepared via FTDCS.
2. Effect of T<sub>sub</sub> on the characteristics of β-FeSi<sub>2</sub> films prepared via RFMS.
3. Effect of T<sub>ann</sub> on the characteristics of NC-FeSi<sub>2</sub> films prepared via RFMS.
4. Effect of C-doping concentrations on characteristics of β-FeSi<sub>2</sub> films prepared via RFMS.

### 4.1 Effect of T<sub>ann</sub> on the characteristics of β-FeSi<sub>2</sub> films prepared via FTDCS

This section presents the characteristic of the β-FeSi<sub>2</sub> films prepared T<sub>sub</sub> of 600 °C via FTDCS with an annealing process at different T<sub>ann</sub> of 200 °C, 400 °C and 600 °C under vacuum ambient. Their Raman spectra, surface and cross-section morphologies, surface roughness, wetting angle and mechanical properties were presented and discussed.

#### 4.1.1 Raman spectra

Figure 4.1 presents the Raman spectra for the formed β-FeSi<sub>2</sub> films with and without annealing. The as-formed β-FeSi<sub>2</sub> films exhibited the peaks of ~194 cm<sup>-1</sup> and ~247 cm<sup>-1</sup> at the centered ranging from 150 cm<sup>-1</sup> to 350 cm<sup>-1</sup>. It was observed that the as-prepared films exhibited the β phase, which conformed with the typical Raman of β-FeSi<sub>2</sub> [73,74]. After annealing, the annealed β-FeSi<sub>2</sub> films at T<sub>ann</sub> of 200 °C, 400 °C and 600 °C exhibited the similarity of Raman spectra as compared to the β-FeSi<sub>2</sub> films without annealing. Further, the annealed β-FeSi<sub>2</sub> films at the T<sub>ann</sub> of 400 °C and 600 °C showed an additional Raman peaks at a centered position of 200 cm<sup>-1</sup>. In fact, there has been discussed that the typical Raman peaks for β-FeSi<sub>2</sub> at the scattered position

of less than  $280\text{ cm}^{-1}$  indicated the molecular displacement of Fe-Fe bonding for the  $\beta$ -FeSi<sub>2</sub> [73]. For other locations, the Raman peaks at the centered position of  $\sim 194$  and  $\sim 248\text{ cm}^{-1}$  are predominated by the motion of Fe atoms, which associated to the angular and radial motions of Fe atoms, respectively. For the peak of  $200\text{ cm}^{-1}$ , this peak corresponds to the polarizability tensor, c-polarization, of the  $\beta$ -phase [75].

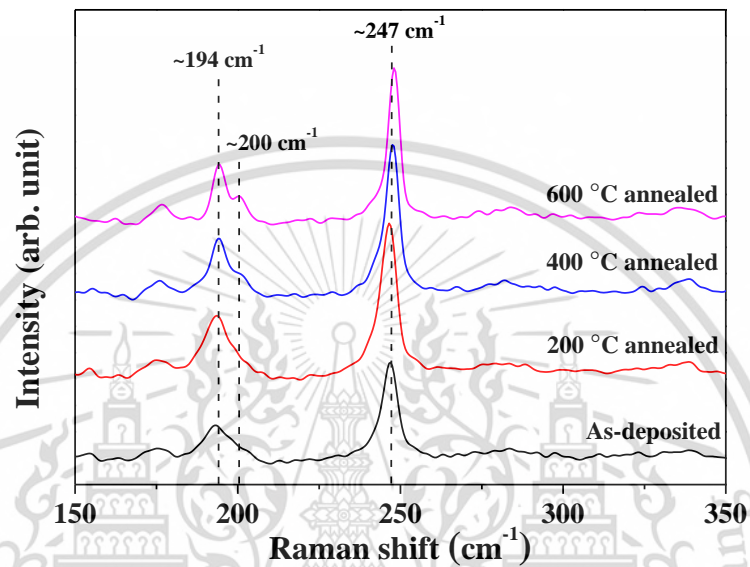
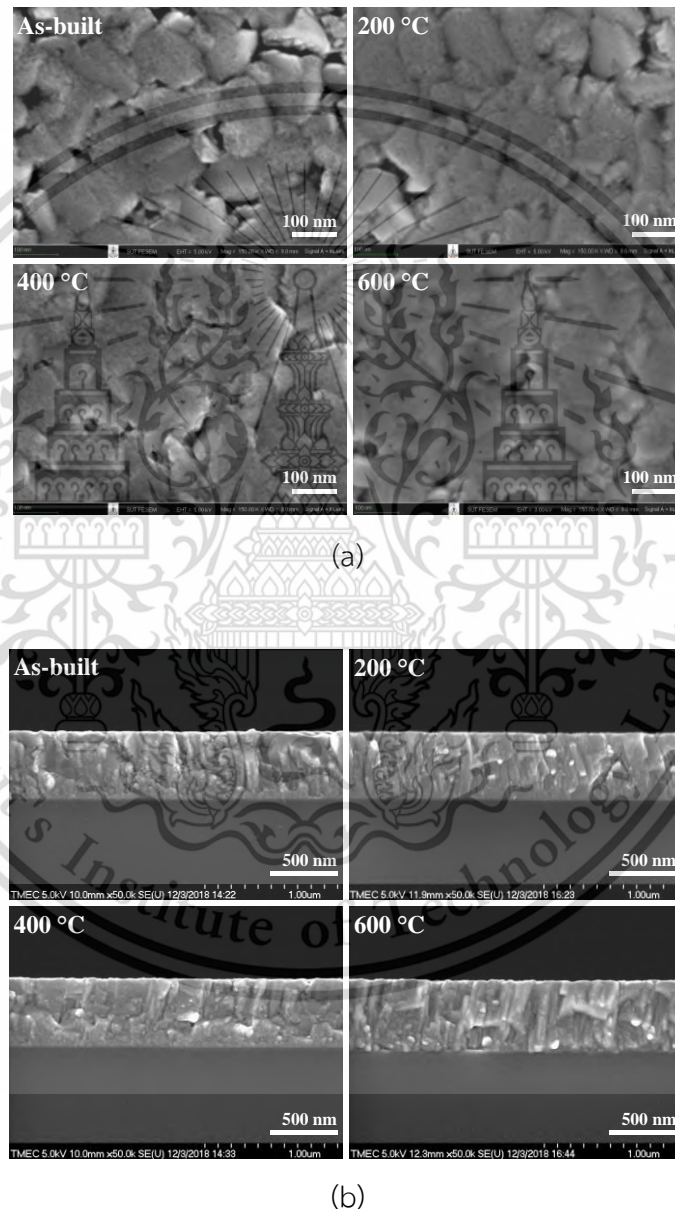


Figure 4.1 Raman spectra for the  $\beta$ -FeSi<sub>2</sub> films deposited by FTDCS with different  $T_{\text{ann}}$ .

#### 4.1.2 Surface and cross-section morphologies

Figure 4.2 (a) and (b) represent the surface and cross-section morphologies for the  $\beta$ -FeSi<sub>2</sub> films produced by FTDCS, with a post annealing at different  $T_{\text{ann}}$ , at 150k and 50k of magnitude, respectively. It was observed that the surface for the unannealed  $\beta$ -FeSi<sub>2</sub> films showed several of crystallites with a uniform formation over the surface with a grain's diameter of around 114.11 nm. The areas of porous were also observed between their grain boundaries. After annealing, the film's surface was noted that the film surface consisted of a compact format of grain's shape with higher  $T_{\text{ann}}$ , where the porous areas also lightly lessen than that of the unannealed films. Moreover, the grain's diameter for the annealed films was altered to 126.79 nm, 135.12 nm, and 146.13 nm after annealing at  $T_{\text{ann}}$  of 200 °C, 400 °C, and 600 °C, respectively. Therefore, this indicated that the annealing process at the applying  $T_{\text{ann}}$  of 200 °C, 400 °C and 600 °C influenced to the surface property of  $\beta$ -FeSi<sub>2</sub> films.

The cross-sectional property for the unannealed  $\beta$ -FeSi<sub>2</sub> films was identified that the interface between the layers of films and Si substrate has no distortions. As well, the diffusion of  $\beta$ -FeSi<sub>2</sub> films to the Si plane was not observed for the annealed  $\beta$ -FeSi<sub>2</sub> films at a  $T_{\text{ann}}$  ranging of 200 – 600 °C. From the results, a well cross-sectional property, smooth and sharp interface, for the  $\beta$ -FeSi<sub>2</sub> films can be received for annealing conditions.



**Figure 4.2** The views of (a) surface and (b) cross-sectional of the  $\beta$ -FeSi<sub>2</sub> films prepared by FTDCS system with post-annealing at different  $T_{\text{ann}}$ .  
 This material is reserved for educational use only, not allowed for commercial use.  
 Forbidden to modify the content, and cite the document when use.

### 4.1.3 Surface roughness

Figure 4.3 reveals the surface for the  $\beta$ -FeSi<sub>2</sub> films with a different annealing conditions of unannealed and annealed at 200, 400 and 600 °C, investigated through AFM technique. With a non-contact mode, the surface for the unannealed  $\beta$ -FeSi<sub>2</sub> films presents the grooves over the surface, including the void among them. The surface for the unannealed  $\beta$ -FeSi<sub>2</sub> films was investigated that it held a minimal  $R_{rms}$  of around 2.02 nm. This should come from the advantages for the fabrication technique of FTDCS, where the surface of the substrate was located far from the generated plasma region during the preparation [49]. So that, the deposited film surface took less damage from the plasma during a sputtering as well. The surface for the annealed  $\beta$ -FeSi<sub>2</sub> films at 200 °C exhibited  $R_{rms}$  of 2.48 nm, which was lightly altered to 2.60 and 2.89 nm after annealing at  $T_{ann}$  of 400 and 600 °C, respectively. This could be discussed that  $T_{ann}$  at ranging of 200 - 600 °C slightly affected to the roughness for the surface of  $\beta$ -FeSi<sub>2</sub> films.

**Table 4.1** Surface  $R_{rms}$  for the  $\beta$ -FeSi<sub>2</sub> films after annealing.

$T_{ann}$ (°C)	$R_{rms}$ (nm)
Unannealed	2.02
200	2.48
400	2.60
600	2.89

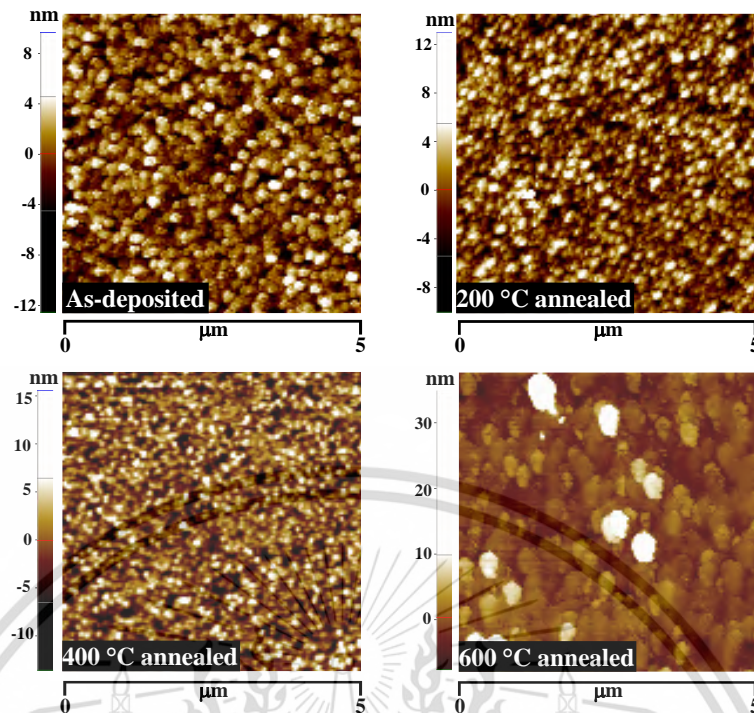


Figure 4.3 AFM results for the  $\beta$ -FeSi<sub>2</sub> films prepared by FTDCS technique under different  $T_{\text{ann}}$ .

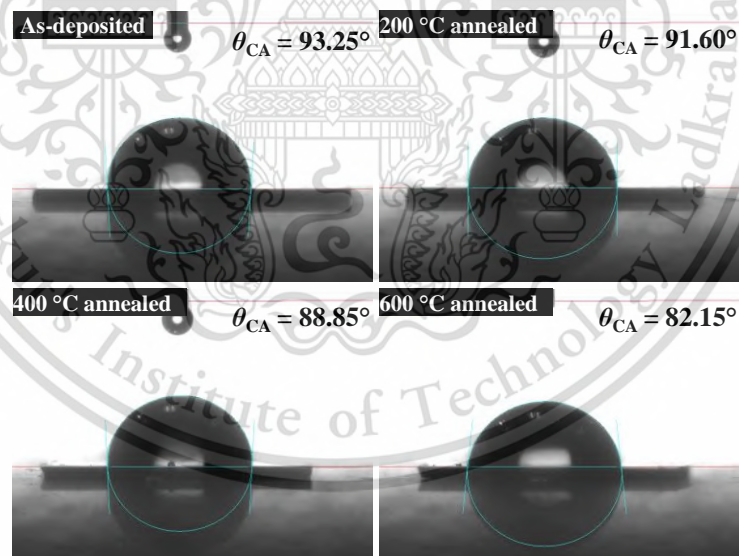
#### 4.1.4 Wetting angle

Figure 4.4 presents the set of captured images between the probe liquid and the surface layer of the  $\beta$ -FeSi<sub>2</sub> films, at  $T_{\text{ann}}$  of unannealed, 200, 400 and 600 °C. For the unannealed films, the surface demonstrates a high wetting angle to the probe liquid with the  $\theta_{\text{CA}}$  of 93.25°, where the  $\theta_{\text{CA}}$  was in range of hydrophobic state. For the unannealed  $\beta$ -FeSi<sub>2</sub> films, it could be simplified through the wetting model of Cassie-Baxter [76-79]. This model mainly discusses to the existence of those air-pockets surrounding above the solid surface, which reduces the contact area of the liquid droplet and uplift the wetting angle [79,80]. Namely, the surface which consists of the air-pockets will provide a superior wetting angle than those surfaces without the air-pockets [85]. As FESEM and AFM results, it was observed that the surface for the unannealed  $\beta$ -FeSi<sub>2</sub> films consisted of several void and groove in a nano-scale covering the surface, where those properties could be behaved as the air-pockets to support the droplet. The surface for the  $\beta$ -FeSi<sub>2</sub> exhibited a reduction of  $\theta_{\text{CA}}$  after annealing. The annealed  $\beta$ -FeSi<sub>2</sub> films at  $T_{\text{ann}}$  of 200 °C exhibited the  $\theta_{\text{CA}}$  of 91.6°, where it decreased to 88.85° and 82.15° after annealed at 400 °C and 600 °C, respectively. The

result showed that the annealed  $\beta$ -FeSi<sub>2</sub> films exhibited the  $\theta_{CA}$  in range of hydrophobic, where it turned into hydrophilic after annealing at 400 °C and 600 °C. The alteration of wetting state could be discussed to the changing in the wetting model of Wenzel, due to the lessened hydrophobicity to maintain in the Cassie-Baxter state [79]. For the annealed  $\beta$ -FeSi<sub>2</sub> films, this should be regarded to a larger contact area between the film's surface and the probe liquid, where the liquid allowed to infiltrate to the gaps around the groove region [80,81]. According to the wetting angle, it clearly noticed that the  $\theta_{CA}$  for  $\beta$ -FeSi<sub>2</sub> was reduced after providing higher  $T_{ann}$ .

**Table 4.2**  $\theta_{CA}$  and wetting state for the  $\beta$ -FeSi<sub>2</sub> films at different  $T_{ann}$ .

$T_{ann}$ (°C)	$\theta_{CA}$	Wetting state
Unannealed	93.25	Hydrophobic
200	91.60	Hydrophobic
400	88.85	Hydrophilic
600	82.15	Hydrophilic



**Figure 4.4** Wetting angle between the probe liquid and  $\beta$ -FeSi<sub>2</sub> film's surface with different annealing conditions.

#### 4.1.5 Mechanical property

Figure 4.5 presents a plot of load versus depth from nanoindentation test on the film's surface of  $\beta$ -FeSi<sub>2</sub> films in cases of non-annealing and annealing. As presented in Figure 4.5, the indentation load was performed to the  $\beta$ -FeSi<sub>2</sub> films surface at 5 mN with a 15 sec of dwell time. For the  $\beta$ -FeSi<sub>2</sub> films without annealing, the surface revealed the hardness of around 37.55 GPa with an indented depth of around 28 nm of surface layer, where the reduced elastic modulus was found to be around 643.42 GPa. For the unannealed  $\beta$ -FeSi<sub>2</sub> films, the hardness ranging was found to be less than the diamond and diamond liked carbon (DLC) films, that are hard coating candidate materials, and their hardness was around 80 to 100 GPa [82,83]. In contrast, the elastic modulus for the unannealed  $\beta$ -FeSi<sub>2</sub> was found to be better than the DLC films [48]. This should be due to the facts that the  $\beta$ -FeSi<sub>2</sub> films consist of the chemical bonding of Fe-Si and Fe-Fe, with the substantial contribution of d-electrons, which contrasted to the C-based material [48].

For the annealed  $\beta$ -FeSi<sub>2</sub> at varied  $T_{ann}$ , the annealed films at  $T_{ann}$  of 200 °C exhibited a hardness of 39.84 GPa and 659.46 GPa for the reduced elastic modulus. With an increasing of  $T_{ann}$ , the hardness and reduced elastic modulus for the 400 °C annealed  $\beta$ -FeSi<sub>2</sub> films were 48.06 GPa and 681.27 GPa, respectively, where they altered to 64.88 GPa and 756.50 GPa after annealing at 600 °C. As the results, the enhancement for the hardness of  $\beta$ -FeSi<sub>2</sub> films after annealing can be referred to the growth of the grain diameters due to an improvement of  $T_{ann}$ . In fact, the results can be also understood by the inverse Hall-Petch effect [48,82]. It was indicated that dislocations play a primary role in the Hall-Petch effect [84,85], whereas grain boundary sliding is notable for the hardness of  $\beta$ -FeSi<sub>2</sub> films. For this reason, the behaviors observed here may be indicative of the structure of the grain boundary being more relevant to the primary mechanical responses during indentation in  $\beta$ -FeSi<sub>2</sub> films.

**Table 4.3** Hardness and reduced elastic modulus for  $\beta$ -FeSi<sub>2</sub> films at different T<sub>ann</sub>.

T <sub>ann</sub> (°C)	Hardness (GPa)	Reduced elastic modulus (GPa)
Unannealed	37.55	643.42
200	39.84	659.46
400	48.06	681.27
600	64.88	756.50

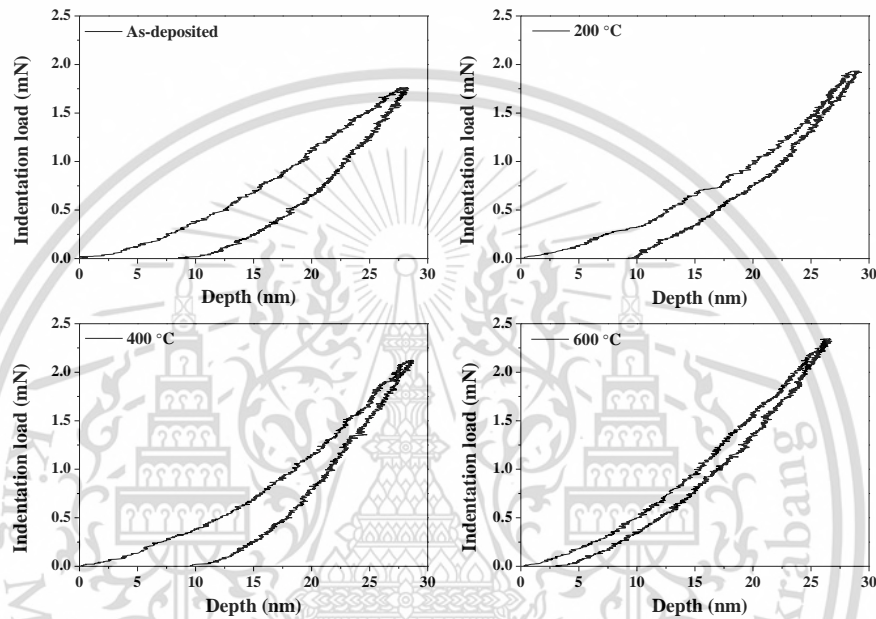


Figure 4.5 Load-depth plots of the  $\beta$ -FeSi<sub>2</sub> films after annealing at 200 °C, 400 °C and 600 °C.

## 4.2 Effect of $T_{\text{sub}}$ on the properties of $\beta$ -FeSi<sub>2</sub> films formed via RFMS

This section presents the characteristic of the  $\beta$ -FeSi<sub>2</sub> films prepared via RFMS at different  $T_{\text{sub}}$  of 500 °C, 560 °C and 600 °C. Their Raman spectra, surface and cross-sectional morphologies, surface roughness, and wetting angle were presented and discussed.

### 4.2.1 Raman spectra

Figure 4.6 shows the scattered Raman positions of the  $\beta$ -FeSi<sub>2</sub> deposited via RFMS at  $T_{\text{sub}}$  of 500 °C, 560 °C, and 600 °C. At 500 °C, the produced  $\beta$ -FeSi<sub>2</sub> films present the Raman peaks at  $\sim 174 \text{ cm}^{-1}$ ,  $\sim 189 \text{ cm}^{-1}$ ,  $\sim 199 \text{ cm}^{-1}$ ,  $\sim 243 \text{ cm}^{-1}$ ,  $\sim 278 \text{ cm}^{-1}$ , and  $\sim 334 \text{ cm}^{-1}$ , where these positions slightly shifted from the typical Raman line of  $\beta$ -FeSi<sub>2</sub> [73,74]. The shifting referred to the lattice properties such as defects and lattice distortion [75]. At  $T_{\text{sub}}$  of 560 °C and 600 °C, the Raman peaks of the  $\beta$ -FeSi<sub>2</sub> films exhibited various scattered positions at around  $\sim 174 \text{ cm}^{-1}$ ,  $\sim 192 \text{ cm}^{-1}$ ,  $\sim 199 \text{ cm}^{-1}$ ,  $\sim 246 \text{ cm}^{-1}$ ,  $\sim 281 \text{ cm}^{-1}$ , and  $\sim 344 \text{ cm}^{-1}$ . In comparison with the Raman lines of 560 °C and 600 °C, it can be observed that the peaks of  $\sim 189 \text{ cm}^{-1}$ ,  $\sim 243 \text{ cm}^{-1}$ , and  $\sim 278 \text{ cm}^{-1}$  for the  $\beta$ -FeSi<sub>2</sub> films prepared at 500 °C were shifted to a higher position, due to the effect of lattice thermal expansion, by increasing  $T_{\text{sub}}$  [99]. The lattice expansion in the growth of  $\beta$ -FeSi<sub>2</sub> films could be instigated by in-plane lattice strain due to the mismatch in thermal expansion coefficient and lattice constant between the films and the substrate [86]. A decrease in Si-vacancies density causes a shifting of the Raman spectra as well [86]. Typically, based on the Raman line of  $\beta$ -FeSi<sub>2</sub> material, the displacement of Fe-Fe in the lattice occurred at a position lower than  $280 \text{ cm}^{-1}$  [73]. The intensive peaks of around  $\sim 194 \text{ cm}^{-1}$ ,  $\sim 200 \text{ cm}^{-1}$ , and  $\sim 247 \text{ cm}^{-1}$  are indicative to the  $\beta$  phase of the FeSi<sub>2</sub> composite [82]. Specifically, these positions of the Raman line present the eminent motion of Fe atoms between the association of angular and radial motion inside the Fe atoms [87], which also specify the Raman active mode of the  $\beta$ -FeSi<sub>2</sub> [74,75]. For the other positions, the Raman peaks at  $\sim 283 \text{ cm}^{-1}$  and  $\sim 340 \text{ cm}^{-1}$  disclose the vibrational correspondence of Fe-Si or Si-Si bonding, while the  $\sim 177 \text{ cm}^{-1}$  peak correlates to the Fe-Fe bonding at lower energy [73,74]. So that, the Raman line of the created  $\beta$ -FeSi<sub>2</sub> films via RFMS, for all  $T_{\text{sub}}$  conditions, showed similarities to the same position of a typical Raman line of  $\beta$ -FeSi<sub>2</sub> material [73,74].

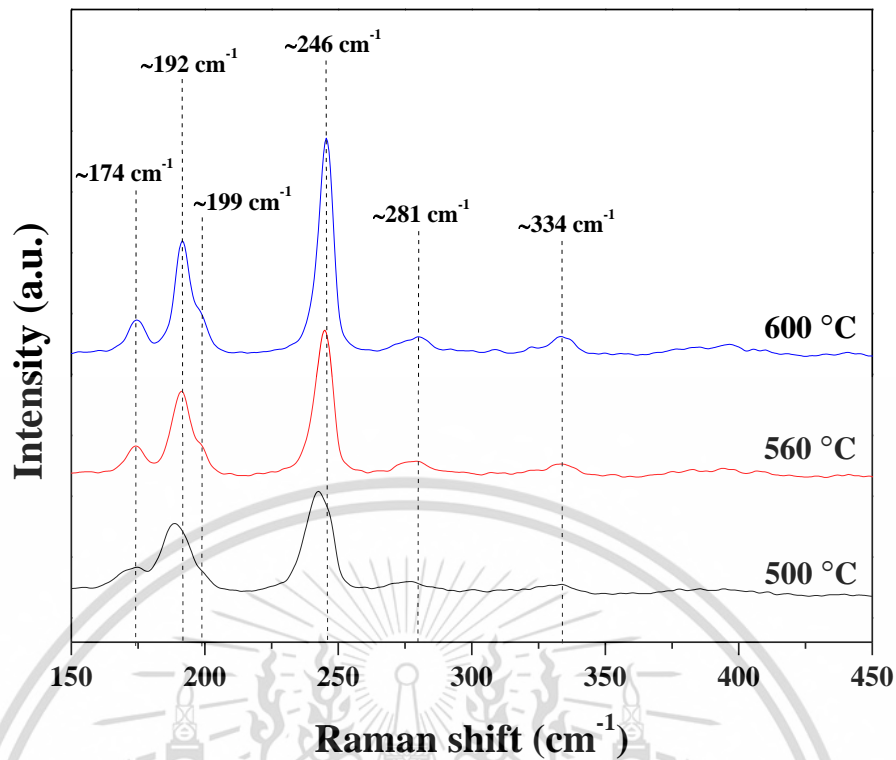


Figure 4.6 Raman lines of the prepared  $\beta$ -FeSi<sub>2</sub> thin films via RFMS method at different T<sub>sub</sub> of 500 °C, 560 °C, and 600 °C.

#### 4.2.2 Surface and cross-section morphologies

Figure 4.7 presents the planar and cross-sectional images for the  $\beta$ -FeSi<sub>2</sub> films formed at T<sub>sub</sub> of 500 °C, 560 °C, and 600 °C. The surface for the formed films at 500 °C exhibited a forming of grain boundaries with a grain size of around 28 nm to 30 nm with some porous zones, where film's surface barely affected after employing T<sub>sub</sub> of 560 °C. At T<sub>sub</sub> of 600 °C, the surface demonstrated denser grain with an average grain size of around 36 nm, where it contained copious porous zones around the boundary's edge. It was observed that the surface of  $\beta$ -FeSi<sub>2</sub> films exhibited a tighter grain zone after employing higher T<sub>sub</sub>, which should be due to an increasing of surface migration of the adatoms with higher energy [16]. Namely, the increase in grain size with a uniform distribution over the surface arose from the suppression of the limited mobility of adatoms by increasing T<sub>sub</sub> [15]. Due to the rise of T<sub>sub</sub>, the smaller grains can be activated through larger energy, which generated greater mobility of nanoparticles [88]. Wherefore, the promotion of larger grain was developed from that surface migration of adatoms, which resulted to a formation with larger size [88].

The cross-sectional property between  $\beta$ -FeSi<sub>2</sub> layer and Si substrate, at different  $T_{\text{sub}}$ , was demonstrated in the cross-section at 50 kx of magnification. A sharp line of the interface and smooth connection, with a thickness of around 350 nm, was found for all prepared  $\beta$ -FeSi<sub>2</sub> films at 500 °C, 560 °C, and 600 °C. Namely, there is no collapse area between the  $\beta$ -FeSi<sub>2</sub> film layer and the Si substrate.

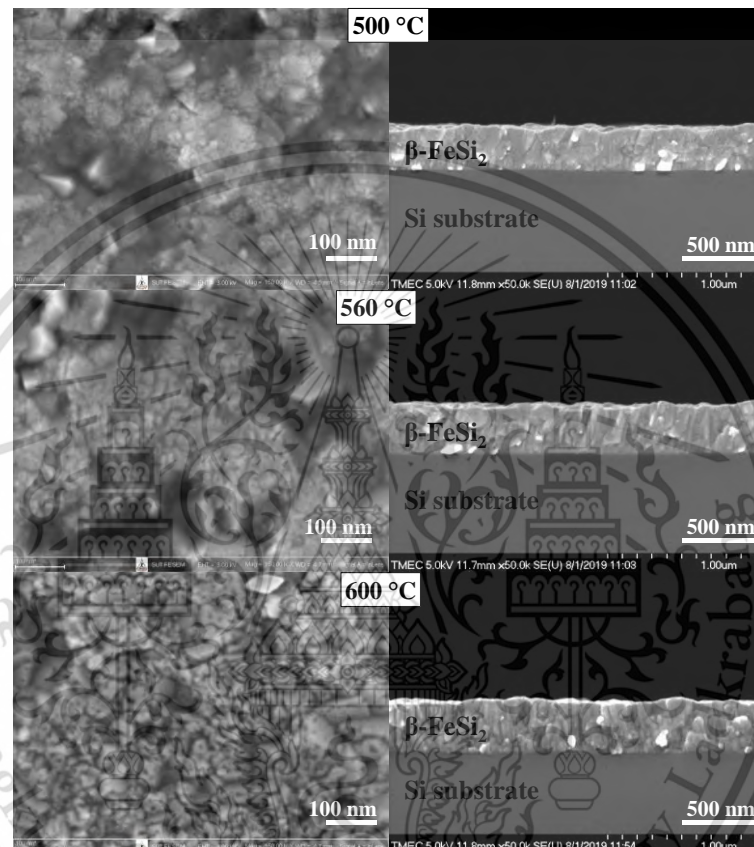


Figure 4.7 Planar and cross-sectional images of the  $\beta$ -FeSi<sub>2</sub> films prepared at the  $T_{\text{sub}}$  of 500 °C, 560 °C, and 600 °C.

#### 4.2.3 Surface roughness

Figure 4.8 depicts the scanned AFM results, using non-contact scanning mode, of the  $\beta$ -FeSi<sub>2</sub> films formed at different  $T_{\text{sub}}$  of 500 °C, 560 °C, and 600 °C. The surface of the prepared  $\beta$ -FeSi<sub>2</sub> films at 500 °C held a  $R_{\text{rms}}$  of around 10.19 nm. The  $R_{\text{rms}}$  value of the  $\beta$ -FeSi<sub>2</sub> film surface was considerably increased to a higher value for the fabricated films with an increment of  $T_{\text{sub}}$ . The  $R_{\text{rms}}$  for  $\beta$ -FeSi<sub>2</sub> film surface was increased to 10.84 nm and 13.67 nm at the increased  $T_{\text{sub}}$  of 560 °C and 600 °C, respectively. It was observed that the  $R_{\text{rms}}$  value of the  $\beta$ -FeSi<sub>2</sub> film surface was affected

This material is reserved for educational use only, not allowed for commercial use.  
Forbidden to modify the content, and cite the document when use.

by the  $T_{\text{sub}}$ . The alteration of the surface topology could be inferred to the occurrence of grain growth. At higher  $T_{\text{sub}}$ , there was a substantial enhancement in the rate of surface migration of adatoms on the substrate surface, where the adatoms gained additional energy besides kinetic energy [89]. The larger grains were formed due to the coalescence of the surrounding grains, resulting in an increased roughness of the film surface [89].

**Table 4.4** Surface  $R_{\text{rms}}$  for the  $\beta$ -FeSi<sub>2</sub> films formed at different  $T_{\text{sub}}$ .

$T_{\text{sub}}$ (°C)	$R_{\text{rms}}$ (nm)
500	10.19
560	10.84
600	13.67

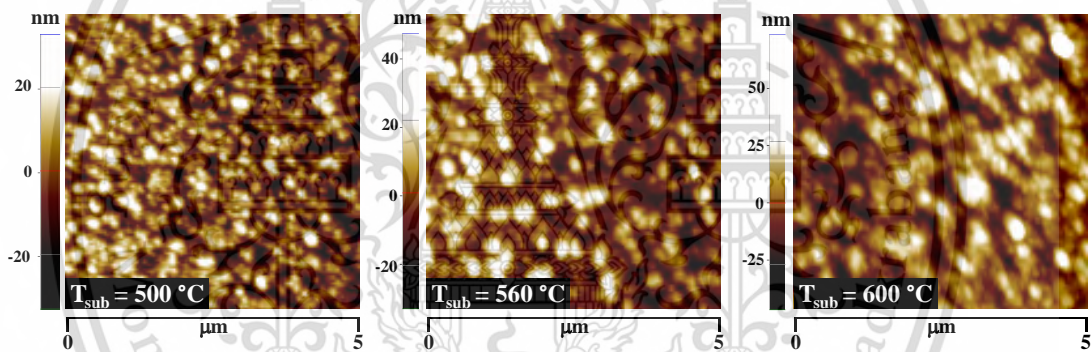


**Figure 4.8** AFM images of the  $\beta$ -FeSi<sub>2</sub> film surface fabricated at  $T_{\text{sub}}$  of 500°C, 560 °C, and 600 °C via RFMS.

#### 4.2.4 Wetting angle

Figure 4.9 gives a measured results of the  $\theta_{\text{CA}}$  value between the DI water droplet and the surface of  $\beta$ -FeSi<sub>2</sub> films formed at different  $T_{\text{sub}}$  via RFMS. At 500 °C, the surface of  $\beta$ -FeSi<sub>2</sub> films exhibited a hydrophobic property with 99.25° of  $\theta_{\text{CA}}$ . At 500 °C, the film's surface consisted of the porous areas and rough surface. Therefore, the wetting property of rough or porous film surface could be clarified by the theorized models of Wenzel and Cassie-Baxter [78]. For the Wenzel model, the liquid medium would entirely expand to the composition, in micro or nanoscale, over the existed porous areas [69]. The Wenzel model was proposed in a formula form of  $\cos\theta_w =$

This material is reserved for educational use only, not allowed for commercial use. Forbidden to modify the content, and cite the document when use.

$R(\cos\theta)$ , where  $R$  is the ratio of the actual area of rough surface to the normally projected area [69,81]. As Cassie-Baxter's model, this model generally describes the interfacial surface tension between the groove and a dropped liquid, in the case of a liquid that lays on the rough or porous surface [81]. Consequently, the basis of this principle explains the occurrence of voids around the contact surface, where air can enter the vacant spaces and support beneath the fluid [80,81,90,91]. Resultingly,  $\theta_{CA}$  in the concept of Cassie-Baxter leads to an enhancement of the  $\theta_{CA}$  value more than a flat or smooth surface area [80,91]. For the deposited films at the different temperatures, the  $\beta$ -FeSi<sub>2</sub> films revealed an improvement of  $\theta_{CA}$ . The  $\theta_{CA}$  values for the  $\beta$ -FeSi<sub>2</sub> films formed at  $T_{sub}$  of 560 °C and 600 °C were 99.80° and 102.00°, respectively. At higher  $T_{sub}$ , the  $\beta$ -FeSi<sub>2</sub> films presented a hydrophobicity of the surface with higher  $\theta_{CA}$ . As the morphological results, the surface of the  $\beta$ -FeSi<sub>2</sub> formed at 500 °C, 560 °C, and 600 °C consisted of the  $R_{rms}$  values of around 10 nm to 13 nm, where the small grains coalesced at higher  $T_{sub}$ . With the models of Wenzel and Cassie-Baxter, an improvement of the  $\theta_{CA}$  value for the  $\beta$ -FeSi<sub>2</sub> films can be inferred to an increase of the  $R_{rms}$  value at higher  $T_{sub}$ .

**Table 4.5**  $\theta_{CA}$  and wetting state for the  $\beta$ -FeSi<sub>2</sub> films formed at different  $T_{sub}$ .

$T_{sub}$ (°C)	$\theta_{CA}$ (°)	Wetting state
500	99.25	Hydrophobic
560	99.80	Hydrophobic
600	102.00	Hydrophilic

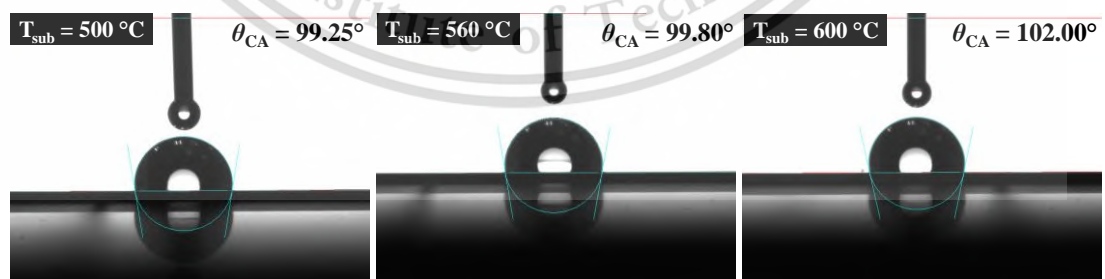


**Figure 4.9** Wetting angle for the surface of  $\beta$ -FeSi<sub>2</sub> films formed via RFMS at different  $T_{sub}$ .

### 4.3 Effect of $T_{\text{ann}}$ on the characteristics of NC-FeSi<sub>2</sub> films prepared via RFMS

This section presents the characteristics of the NC-FeSi<sub>2</sub> films prepared  $T_{\text{sub}}$  of RT via RFMS with an annealing process at the different  $T_{\text{ann}}$  of 100 °C, 300 °C and 500 °C under air ambient. Their XRD patterns, Raman spectra, surface morphology, surface roughness, wetting angle were presented and discussed.

#### 4.3.1 XRD patterns

Figure 4.10 presents the diffraction patterns of the NC-FeSi<sub>2</sub> films, which deposited onto the Si substrates, via RFMS systems at  $T_{\text{sub}}$  of RT under different post-annealing conditions. Without annealing, the NC-FeSi<sub>2</sub> films displayed their diffraction pattern with a broad shape at the  $2\theta$  positions of around 42° to 52°. The results showed that the as-prepared NC-FeSi<sub>2</sub> films were identified to comprise of a NC formation, where their  $D$  was evaluated to be around 1.5 nm. The broadening of diffraction peaks for NC-FeSi<sub>2</sub> films is due to the overlapping of the diffraction peaks of  $\beta$ -phase FeSi<sub>2</sub> [14,45]. After applying annealing procedure, it was noted that the NC-FeSi<sub>2</sub> films demonstrated a change regarding their diffraction pattern after applying a  $T_{\text{ann}}$  of 500 °C. The annealed NC-FeSi<sub>2</sub> films at 500 °C revealed a considerable change of the diffraction's peaks, where several preferred orientations of  $\beta(202)$ ,  $\beta(330)$ ,  $\beta(232)$ ,  $\beta(004)$ ,  $\beta(114)$ ,  $\beta(033)$ ,  $\beta(204)$ ,  $\beta(024)$ ,  $\beta(224)$  and  $\beta(424)$  were clearly noticed. In particular, the change in the diffraction pattern for the annealed films at 500 °C should involve to the fact that the atoms grew an advancement of diffusion activation energy after providing higher temperature, resulting to an allowance of the atoms with lower surface energy to transfer to an energetically favorable place in the crystal lattice [92]. Hence, the crystallites were grown in the preferred direction by having energy supplied at higher temperatures. For annealed NC-FeSi<sub>2</sub> films, the evaluated  $D$  for the annealed NC-FeSi<sub>2</sub> films at  $T_{\text{ann}}$  of 100 °C was approximately around 1.8 nm, which altered to be 3.3 nm and 20.0 nm after receiving higher  $T_{\text{ann}}$  of 300 °C and 500 °C, respectively. The results suggested that the diameter for the NC-FeSi<sub>2</sub> crystallites is dominantly enhanced after applying annealing procedure at 500° C. Namely, the increasing in a diameter should refer to the agglomeration of the crystallites into larger cluster format.

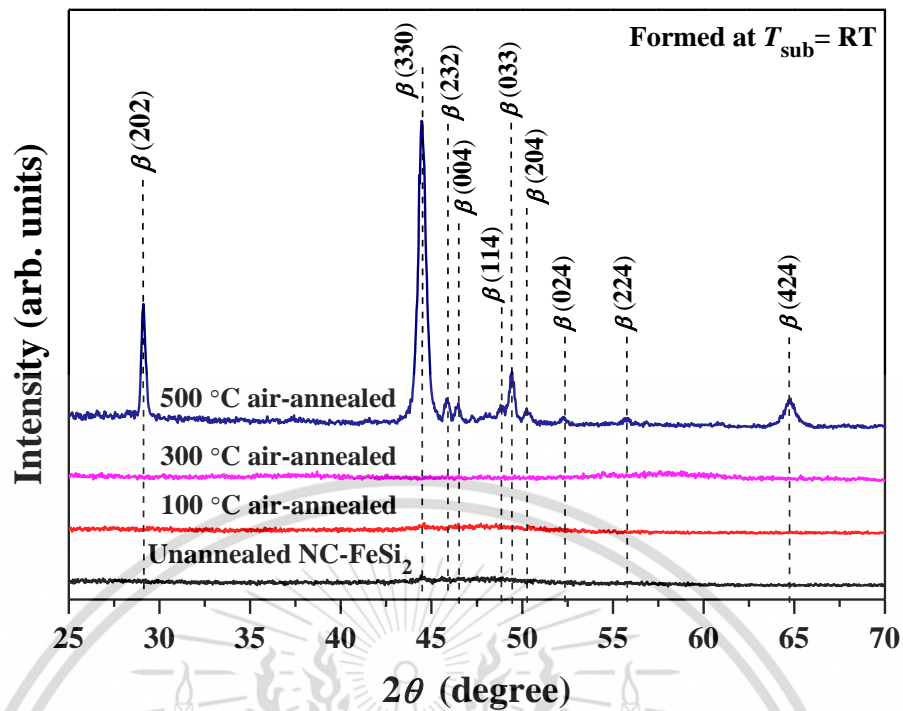


Figure 4.10 Diffraction patterns for the NC-FeSi<sub>2</sub> films at different  $T_{\text{ann}}$ .

#### 4.3.2 Raman spectra

Figure 4.11 reveals the Raman spectra of the NC-FeSi<sub>2</sub> films formed at RT utilizing RFMS with a post-annealing at various  $T_{\text{ann}}$ . As in Figure 4.17, the as-formed NC-FeSi<sub>2</sub> at RT exhibited their Raman line at the centered positions of  $\sim 180.7 \text{ cm}^{-1}$  and  $\sim 232.8 \text{ cm}^{-1}$ , which slightly shifted from the typical Raman peaks for FeSi<sub>2</sub> based material, which were around  $\sim 177 \text{ cm}^{-1}$ ,  $\sim 194 \text{ cm}^{-1}$ , and  $\sim 247 \text{ cm}^{-1}$ . For those typical peaks, they were dominated by the vibration between the Fe atoms inside the  $\beta$ -FeSi<sub>2</sub> material [73-75]. After annealing, the Raman peaks at  $180.7 \text{ cm}^{-1}$  were barely shifted for the films annealed at  $300 \text{ }^\circ\text{C}$  and  $500 \text{ }^\circ\text{C}$ . However, all Raman lines for the unannealed and annealed films showed a shifting as compared to the typical Raman line for the  $\beta$ -FeSi<sub>2</sub>, which might be due to the lattice distortion and defects related to Fe [75].

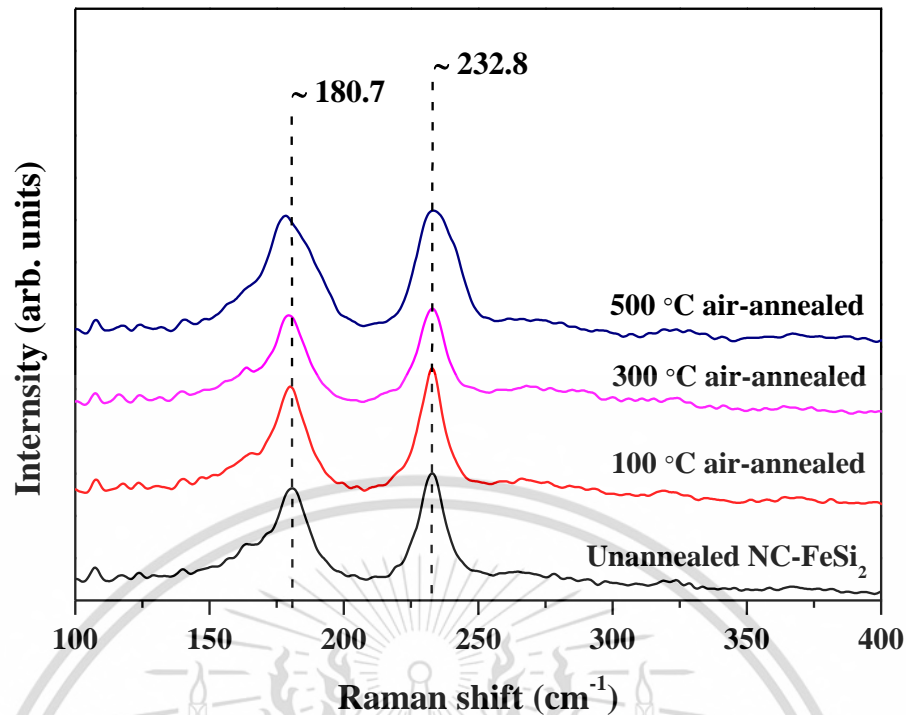


Figure 4.11 Raman profiles for the NC-FeSi<sub>2</sub> films formed via RFMS at  $T_{\text{sub}}$  of RT, under different  $T_{\text{ann}}$ .

#### 4.3.3 Surface morphology

Figure 4.12 presents the plane views for the NC-FeSi<sub>2</sub> film surface at different  $T_{\text{ann}}$ . It was found that the surface, without annealing, consisted of numerous crystallites with an approximated diameter of around 1-3 nm, while the film's surface exhibited minimal change after annealing at  $T_{\text{ann}}$  of 100 °C and 300 °C. The surface for the NC-FeSi<sub>2</sub> films displays a clustering of their crystallites after employing  $T_{\text{ann}}$  of 500 °C. As received from diffraction pattern, the unannealed NC-FeSi<sub>2</sub> films, including the annealed films at 100 °C and 300 °C, were identified that the films held a NC form, where their crystallites should own numerous crystallites with small diameters. The films annealed at 500 °C exhibited a major change in diffraction results, which should be referred to a development of crystalline structure at higher  $T_{\text{ann}}$ .

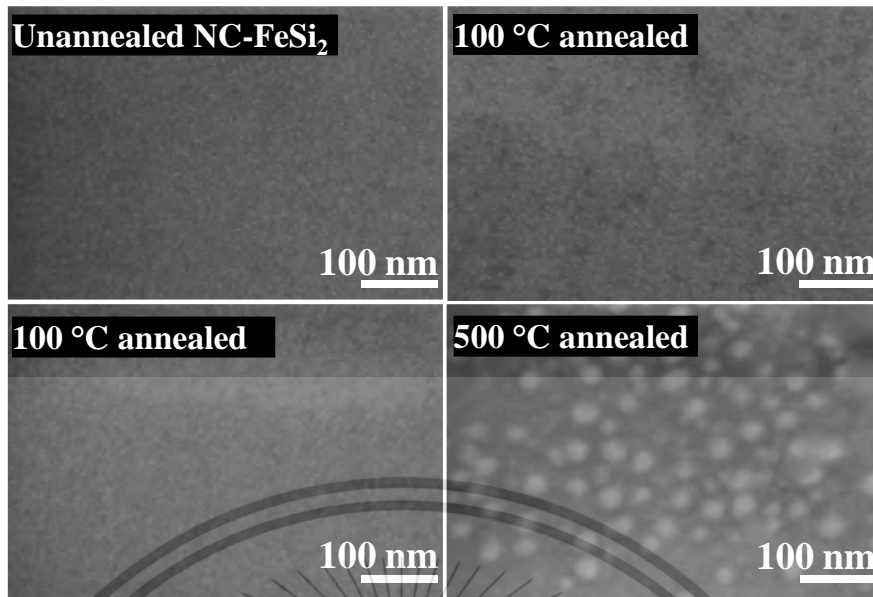


Figure 4.12 Surface images for the NC-FeSi<sub>2</sub> films at different  $T_{\text{ann}}$ .

#### 4.3.4 Surface roughness

Figure 4.13 gives the AFM results for the NC-FeSi<sub>2</sub> films formed at  $T_{\text{sub}}$  of RT under applying an annealing procedure at different  $T_{\text{ann}}$ . In Figure 4.13, the results showed that the unannealed NC-FeSi<sub>2</sub> contained the  $R_{\text{rms}}$  over the surface of 0.94 nm. The increment in surface  $R_{\text{rms}}$  was observed after annealing with higher providing  $T_{\text{ann}}$ . For the annealed NC-FeSi<sub>2</sub> films at 100 °C, the  $R_{\text{rms}}$  over the film's surface was evaluated to be around 1.05 nm, while the annealed NC-FeSi<sub>2</sub> films at 300 °C and 500 °C were 2.68 nm and 5.32 nm, respectively. For the results, the surface roughness was noted to tally with their surface images, where the films gained the rearrangement on their surface as an improvement of crystallinity. At  $T_{\text{ann}}$  lower than 500 °C, the surface contained none of clustering form, regards to their crystallites. In contrast, the 500 °C annealed NC-FeSi<sub>2</sub> films exhibited the change of their surface morphology, where their crystallites were formed into a large cluster form. The rising of  $R_{\text{rms}}$  after annealing should be due to the clustered crystallites, which occurred at a developed  $T_{\text{ann}}$ .

**Table 4.6** Surface  $R_{rms}$  for NC-FeSi<sub>2</sub> films at different  $T_{ann}$ .

$T_{ann}$ (°C)	$R_{rms}$ (nm)
Unannealed	0.94
100	1.05
300	2.68
500	5.32

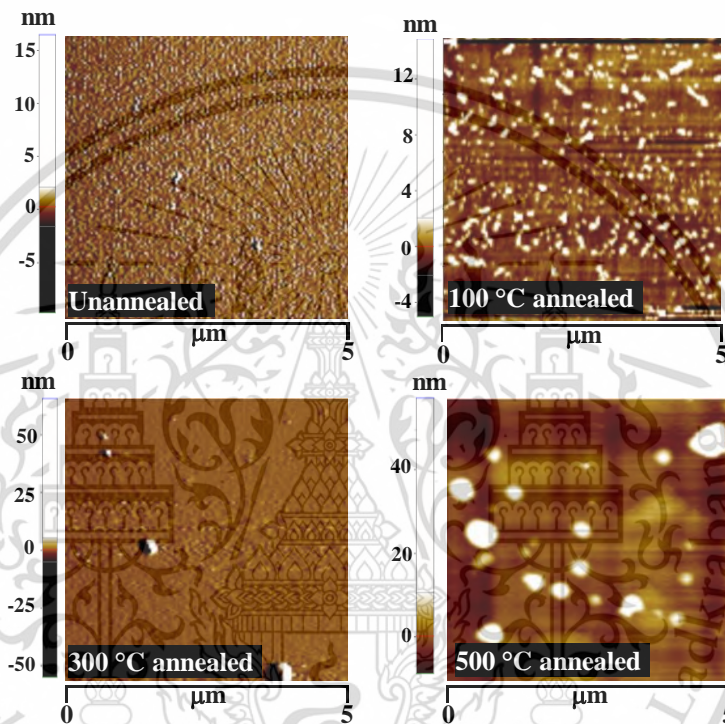


**Figure 4.13** AFM images of NC-FeSi<sub>2</sub> films after annealing at different  $T_{ann}$ .

#### 4.3.5 Wetting angle

Figure 4.14 shows wetting angle for the surface of NC-FeSi<sub>2</sub> films in case of unannealed and annealed at different  $T_{ann}$ . The surface for the NC-FeSi<sub>2</sub> films, without annealing, presented a hydrophobic property with the  $\theta_{CA}$  of 102.35°. By employing post annealing, the surface for 100 °C annealed NC-FeSi<sub>2</sub> films also held hydrophobic property with an average  $\theta_{CA}$  of 100.30°, where it was reduced to 93.45° after annealing at 300 °C. At  $T_{ann}$  of 500 °C, the surface for the NC-FeSi<sub>2</sub> films which annealed at this temperature disclosed a different wetting property to the other NC-FeSi<sub>2</sub> films. The

This material is reserved for educational use only; not allowed for commercial use.  
Forbidden to modify the content, and cite the document when use.

the  $\theta_{CA}$  of 41.70°. From the surface observation, the crystallites for the as-formed NC-FeSi<sub>2</sub> films were clustered after providing an annealing procedure at 500 °C, where the surface morphology for both films was clearly different. So that, as presented in this section, the conversion of wetting state for the surface of NC-FeSi<sub>2</sub> films, from hydrophobic to hydrophilic, should be due to the fact that the liquid occupied to clustered zone between those nanoclusters. Namely, the surface of films took more influence of water-solid interface than that of air-solid interface, when providing higher  $T_{ann}$ . As a result, liquid had conformal contact with the solid surface, which could improve a water-solid interfacial force and led to a reduction of wetting angle. The increment of a material's roughness with a hydrophilic surface induces an increased hydrophilic state, as explained in the wetting model of Wenzel [79].

Table 4.7  $\theta_{CA}$  and wetting state for NC-FeSi<sub>2</sub> films at different  $T_{ann}$ .

$T_{ann}$ (°C)	$\theta_{CA}$ (°)	Wetting state
Unannealed	102.35	Hydrophobic
100	100.30	Hydrophobic
300	93.45	Hydrophobic
500	41.70	Hydrophilic

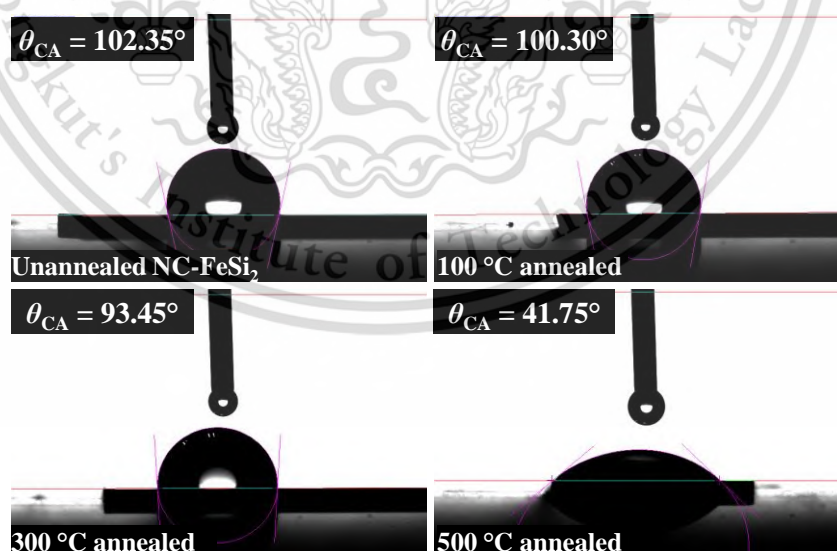


Figure 4.14 Wetting angle for the NC-FeSi<sub>2</sub> films after annealing at  $T_{ann}$  of 100 °C, 300 °C and 500 °C.

This material is reserved for educational use only, not allowed for commercial use.  
Forbidden to modify the content, and cite the document when use.

#### 4.4 Effect of C-doping concentrations on characteristics of $\beta$ -FeSi<sub>2</sub> films prepared via RFMS

This section presents the characteristics of the  $\beta$ -FeSi<sub>2</sub> films prepared at  $T_{\text{sub}}$  of 560 °C via RFMS under varied C-doping concentrations of undoped and C-doped of 0.5 at.%, 1.0 at.% and 3.0 at.%. Their XRD patterns, Raman spectra, optical property, surface morphology, surface roughness and wetting angle were presented and discussed.

##### 4.4.1 XRD patterns

Figure 4.15 presents the diffraction pattern for the undoped and C-doped  $\beta$ -FeSi<sub>2</sub> films. The undoped  $\beta$ -FeSi<sub>2</sub> films exhibited a strong  $\beta$ (202/220) peaks at the position of around 29.0°, including the peak of Si(111) at 28.7°. Also, the weak peaks of Si(222) and  $\beta$ (404/440) were noted at 58.8° and 60.3°, respectively. This indicated to the successful epitaxial formations of  $\beta$ -FeSi<sub>2</sub> films on the substrate of Si(111). The diffraction patterns for all C-doped  $\beta$ -FeSi<sub>2</sub> films displayed that the C-doping concentrations of 0.5 at.% to 3.0 at.% certainly not affected to structural property of  $\beta$ -FeSi<sub>2</sub> films.

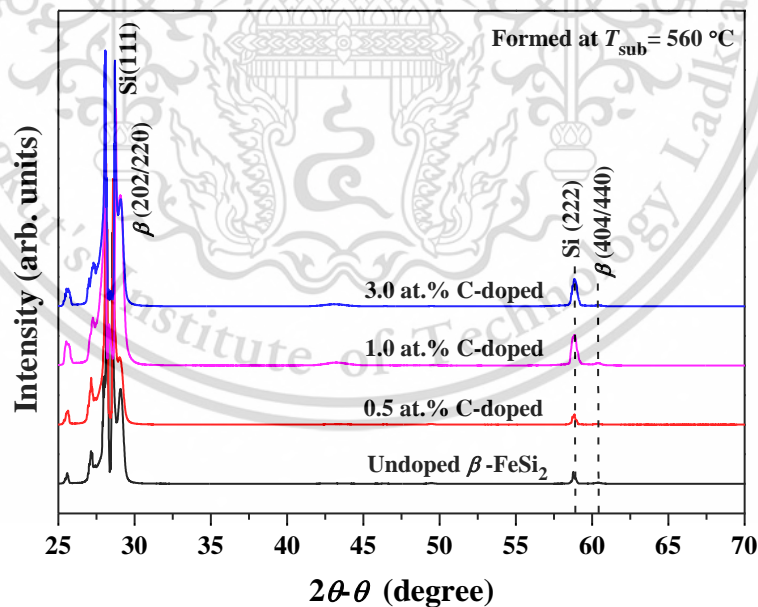


Figure 4.15 Diffraction pattern for the  $\beta$ -FeSi<sub>2</sub> films formed via RFMS at various C-doping concentrations.

#### 4.4.2 Raman spectra

Figure 4.16 denotes to the Raman profiles for  $\beta$ -FeSi<sub>2</sub> films prepared via RFMS with a variation of C-doping concentration. The Raman profile for the undoped  $\beta$ -FeSi<sub>2</sub> films revealed the centered positions of  $\sim 172.8$ ,  $\sim 188.6$  and  $\sim 243.0$  cm<sup>-1</sup>, where their positions slightly shifted from the typical line of  $\beta$ -FeSi<sub>2</sub> material. The main reason for this shifting behavior should be regarded to the expansion of lattice, which introduced a strain at the heterointerface [86,87]. The splitting at 180.7 cm<sup>-1</sup> referred to a diminished defects of FeSi<sub>2</sub> films after providing higher T<sub>sub</sub> [75]. The C-doped FeSi<sub>2</sub>, under 0.5 at.%, 1.0 at.% and 3.0 at.%, also reveals a similarity of Raman peaks as the undoped  $\beta$ -FeSi<sub>2</sub> films. The Raman spectra on this section also suggested that the C-doping concentrations have low impact to the  $\beta$ -FeSi<sub>2</sub> structure.

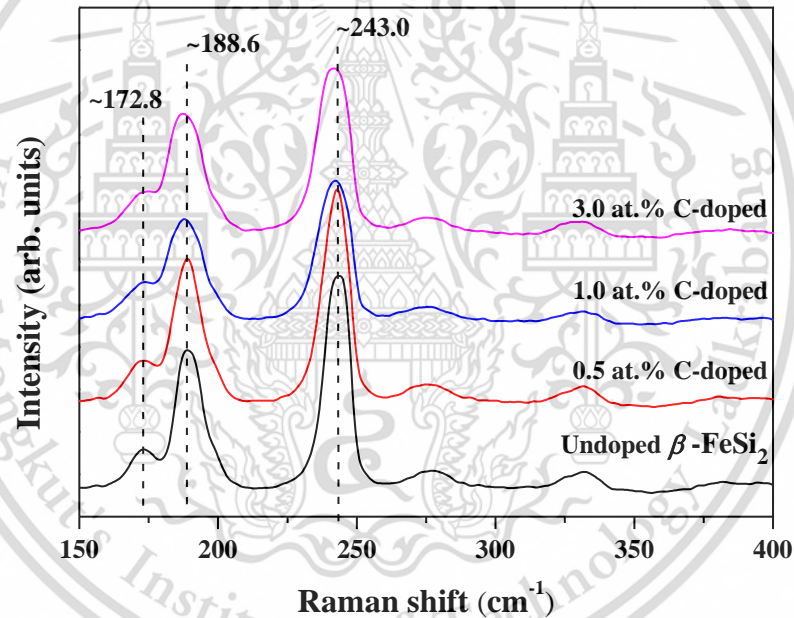


Figure 4.16 Raman profiles of  $\beta$ -FeSi<sub>2</sub> films formed via RFMS at different C-doping concentrations.

#### 4.4.3 Optical property

Figure 4.17 offers the transmittance lines for the  $\beta$ -FeSi<sub>2</sub> films with varied C-doping concentrations. The thickness for the undoped films was examined to be around 306 nm. The thickness for the C-doped films was around 287, 275, and 290 nm under 0.5 at.%, 1.0 at.%, and 3.0 at.% of concentrations. The transmittance spectra for the  $\beta$ -FeSi<sub>2</sub> films without C-doping demonstrate a transmittance percentage of 46 %,

This material is reserved for educational use only, not allowed for commercial use. Forbidden to modify the content, and cite the document when use.

where the films corresponded to the NIR region. For C-doped  $\beta$ -FeSi<sub>2</sub> films, it was observed that the transmittance percentage was decreased with an increase of C-doping concentrations. At 0.5 at.% of C-doping, the  $\beta$ -FeSi<sub>2</sub> films transmitted at a percentage of 42 %, where this reduced to 22% and 20 % at the doping concentrations of 1.0 at.% and 3.0 at.%, respectively. The inset signifies the plots of  $(\alpha h\nu)^2$  versus  $h\nu$  for the  $\beta$ -FeSi<sub>2</sub> films formed at different C-doping concentrations. The intersection of the fitting lines at the axis of  $h\nu$  gave the direct optical  $E_g$  for the films. The evaluated  $E_g$  for the undoped films was noted to be around 0.89 eV, where the  $E_g$  for  $\beta$ -FeSi<sub>2</sub> films slightly changed after increasing of C-doping concentration. With C-doping, the  $E_g$  values were evaluated to be 0.87 eV, 0.84 eV and 0.83 eV for the C-doped films at 0.5 at.%, 1.0 at.%, and 3.0 at.%, respectively. The results showed that the  $\beta$ -FeSi<sub>2</sub> held a lower  $E_g$  range after the films were doped with C element. The narrowing of  $E_g$ , after the C-doping, could be assigned to an increment of the hole density in the semiconductor [40]. Namely, the additional carrier enlarges the current carrier and induces  $E_g$  to become narrower, when doping a C ion with a positive charge into  $\beta$ -FeSi<sub>2</sub> [93].

**Table 4.8** Thickness, transmittance percentage and  $E_g$  for the  $\beta$ -FeSi<sub>2</sub> films under different C-doping concentrations.

C-doped concentrations (at.%)	Thickness (nm)	Transmittance (%)	$E_g$ (eV)
Undoped	306	46.0	0.89
0.5	287	42.0	0.87
1.0	275	22.0	0.84
3.0	290	20.0	0.83

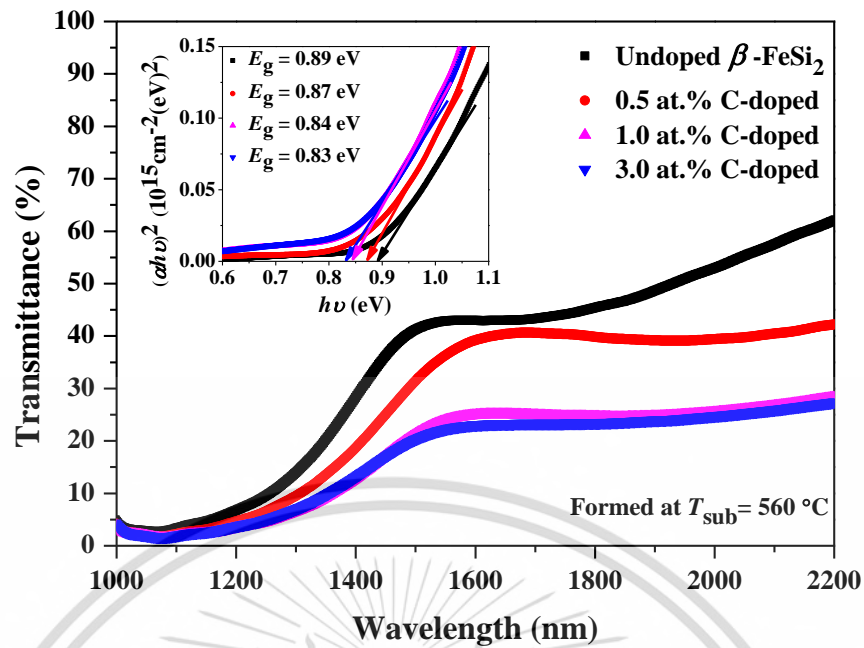
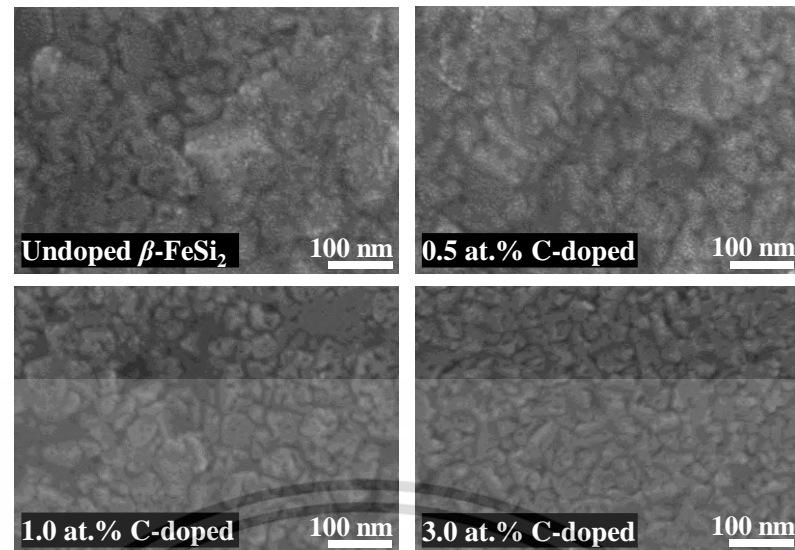


Figure 4.17 Transmittance lines for the  $\beta$ -FeSi<sub>2</sub> films formed at different C-doping concentrations. The inset shows the  $(\alpha h\nu)^2$  versus  $h\nu$  plot for each film.

#### 4.4.4 Surface morphology

Figure 4.18 provides the surface morphology for undoped and C-doped  $\beta$ -FeSi<sub>2</sub> films. The undoped film's surface presented a plenty of small grains with a diameter of approximately around 20 nm – 22 nm. The crystallite's size of the  $\beta$ -FeSi<sub>2</sub> formed via RFMS at 560 °C is larger than those formed at RT due to the limitation of adatoms mobility, which was hindered by the increment of  $T_{\text{sub}}$  [15]. As  $T_{\text{sub}}$  rose, the smaller grains were energized via higher energy, which induced the increase in mobility of nanoparticles as well as the enlargement of grain size [15,17]. For FeSi<sub>2</sub> films with C-doping, the surface for the 0.5 at.% C-doped FeSi<sub>2</sub> films presented a comparable surface arrangement to the undoped  $\beta$ -FeSi<sub>2</sub> films. With 1.0 at.% and 3.0 at.%, the surface for the  $\beta$ -FeSi<sub>2</sub> films exhibited a finer surface, where the grains diameter for these films seemed to be smaller than the undoped  $\beta$ -FeSi<sub>2</sub> films. The reduction in the diameter might be regarded to a result of the difference of grain boundaries from C incorporation, where the incorporation of C content also conduces the hindrance of the grain growth in the films [94,95].



**Figure 4.18** Plane surface for the  $\beta$ -FeSi<sub>2</sub> films formed using different C-doping concentrations via RFMS technique.

#### 4.4.5 Surface roughness

Figure 4.19 reveals results for the AFM images for the  $\beta$ -FeSi<sub>2</sub> films prepared by varied C-doping concentrations. The  $R_{\text{rms}}$  for the FeSi<sub>2</sub> film's surface without C-doping was around 15.71 nm, which this should be due to ion bombarding over their surface during sputtering via RFMS. Compared to the RT-formed FeSi<sub>2</sub> via RFMS, the surface for the  $\beta$ -FeSi<sub>2</sub> prepared at 560 °C showed a higher  $R_{\text{rms}}$ . This signifies an enhancement for the surface roughness with the elevation of  $T_{\text{sub}}$  attributable to the grain growth, where the films prepared at higher temperature should allow the increasing of the migration rate of adatoms [89]. Namely, the adatoms will gain the additional energy aside the kinetic energy at higher temperature. This is the cause of the conglomeration of adjacent small grains into larger grain sizes and brings about the increment of  $R_{\text{rms}}$  [84]. With the increasing of doping concentrations, the surface for the C-doped FeSi<sub>2</sub> films presents the  $R_{\text{rms}}$  values 15.40 nm, 11.49 nm, and 10.59 nm for the doping concentrations of 0.5 at.%, 1.0 at.%, and 3.0 at.%, respectively. The decrement in surface roughness for the C-doped  $\beta$ -FeSi<sub>2</sub> films with an increasing of doping concentrations is possibly regarded to the C incorporation among the FeSi<sub>2</sub> film, which increases the nucleation rate and induces a finer grain [21,93].

**Table 4.9** Surface  $R_{\text{rms}}$  for  $\beta$ -FeSi<sub>2</sub> films at different C-doping concentrations.

C-doped concentrations (at.%)	$R_{\text{rms}}$ (nm)
Undoped	15.71
0.5	15.40
1.0	11.49
3.0	10.59

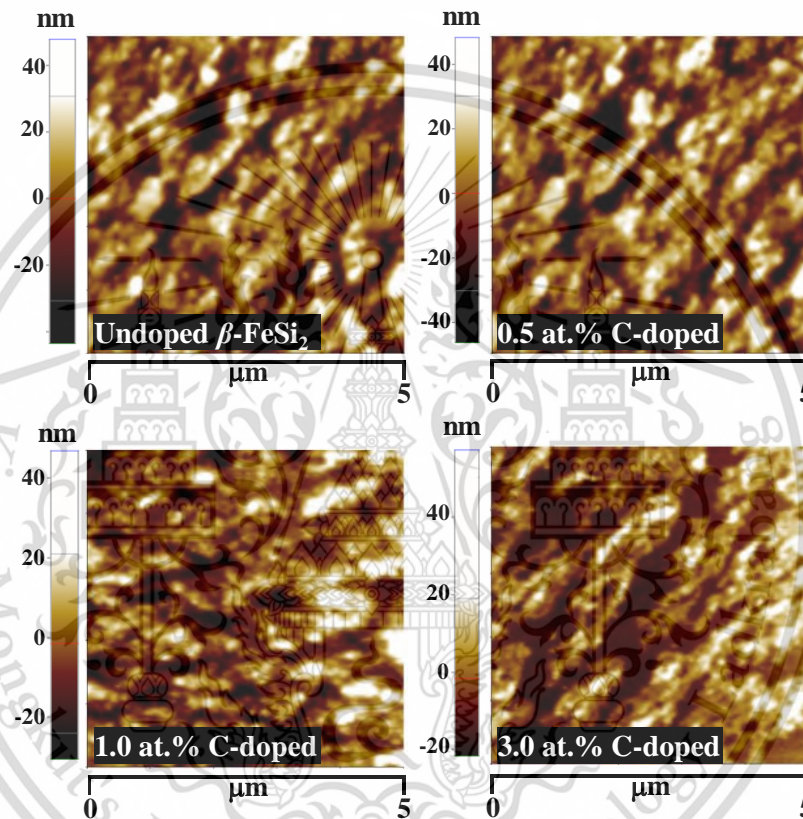


**Figure 4.19** AFM images of  $\beta$ -FeSi<sub>2</sub> films formed via RFMS at different doping concentrations.

#### 4.4.6 Wetting angle

Figure 4.20 exposes the  $\theta_{\text{CA}}$  for the surface of undoped and C-doped  $\beta$ -FeSi<sub>2</sub> films. The wetting angle over the surface for undoped  $\beta$ -FeSi<sub>2</sub> films was determined that the film surface exhibited a hydrophobic property, with average  $\theta_{\text{CA}}$  of 108.35°. As the  $R_{\text{rms}}$  results, the undoped film's surface presented a high roughness, which would prevent the expansion of the liquid drops due to a possibility to contain more air-

This material is reserved for educational use only, not allowed for commercial use.  
Forbidden to modify the content, and cite the document when use.

pockets. Namely, the surface for the undoped films could preserve the hydrophobicity of the surface [96]. For the C-doped films, the surface also showed a hydrophobic property as the undoped films, where the  $\theta_{CA}$  slightly decreased to 107.55°, 105.45° and 103.65° at the C-doping concentrations of 0.5 at.%, 1.0 at.% and 3.0 at.%, respectively. This introduced that the hydrophobicity was reduced with an increasing of C-doping concentrations, which should be also due to a reduction of surface roughness.

Table 4.10  $\theta_{CA}$  and wetting state for  $\beta$ -FeSi<sub>2</sub> films at different C-doping concentrations.

C-doped concentrations (at.%)	$\theta_{CA}$ (°)	Wetting state
Undoped	108.35	Hydrophobic
0.5	107.50	Hydrophobic
1.0	105.45	Hydrophobic
3.0	103.65	Hydrophobic

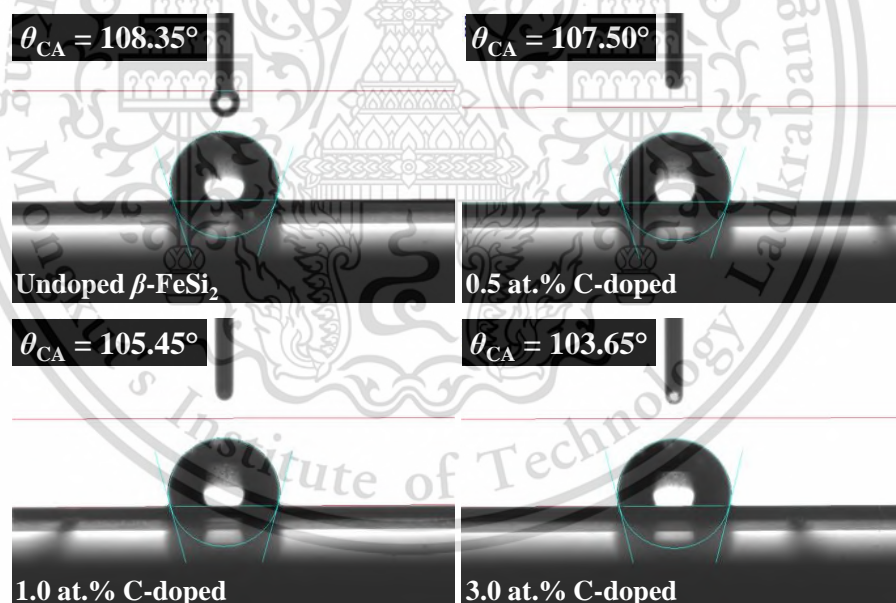


Figure 4.20 Wetting angle for the  $\beta$ -FeSi<sub>2</sub> film surface at different C-doped concentrations.

## Chapter 5

# Conclusions and suggestions

This chapter summarizes the experimental results gained from the research and provides suggestions for related research work requiring further study in the future. The conclusions on each research will be summarized as these following topics:

1. Effect of  $T_{\text{ann}}$  on  $\beta$ -FeSi<sub>2</sub> films formed via FTDCS
2. Effect of  $T_{\text{sub}}$  on  $\beta$ -FeSi<sub>2</sub> films formed via RFMS.
3. Effect of  $T_{\text{ann}}$  on NC-FeSi<sub>2</sub> films formed via RFMS.
4. Effect of C-doping concentrations on  $\beta$ -FeSi<sub>2</sub> films formed via RFMS.
5. Suggestions

### 5.1 Effect of $T_{\text{ann}}$ on $\beta$ -FeSi<sub>2</sub> films prepared via FTDCS

$\beta$ -FeSi<sub>2</sub> films were formed at  $T_{\text{sub}}$  of 600 °C via FTDCS. Then the as-deposited FeSi<sub>2</sub> films were annealed at different  $T_{\text{ann}}$  of 200 °C to 600 °C under vacuum ambient. The surface for the as-deposited  $\beta$ -FeSi<sub>2</sub> films presented low surface roughness with  $R_{\text{rms}}$  of 2.02 nm. The surface for annealed  $\beta$ -FeSi<sub>2</sub> films exhibited more compact formation with an increasing of  $R_{\text{rms}}$ , while the  $R_{\text{rms}}$  enhanced marginally to 2.89 nm after annealing at 600 °C. For the wetting angle, the surface for the as-deposited  $\beta$ -FeSi<sub>2</sub> and 200 °C annealed  $\beta$ -FeSi<sub>2</sub> films demonstrated a wetting state of hydrophobic with  $\theta_{\text{CA}}$  of 93.25° and 91.60°, respectively. The wetting state conversed to hydrophilic after annealed at  $T_{\text{ann}}$  of 400 °C and 600 °C. Nevertheless, the hardness for the  $\beta$ -FeSi<sub>2</sub> improved from 37.55 GPa to 64.88 GPa after annealed at 600 °C. The results presented that the as-deposited and 200 °C annealed  $\beta$ -FeSi<sub>2</sub> films expressed a potential for hydrophobic coatings, while the 600 °C annealed  $\beta$ -FeSi<sub>2</sub> films were attractive for hard coating application.

## 5.2 Effect of $T_{\text{sub}}$ on $\beta$ -FeSi<sub>2</sub> films formed via RFMS

$\beta$ -FeSi<sub>2</sub> thin films on Si(111) substrates were deposited via RFMS method at the  $T_{\text{sub}}$  of 500 °C, 560 °C, and 600 °C. The  $\beta$ -FeSi<sub>2</sub> film surface displayed a formation of grain boundary for the  $T_{\text{sub}}$  greater than or equal to 500 °C. The average grain sizes for the films deposited at 500 °C and 560 °C were around 28 nm to 30 nm, which altered to 36 nm at a  $T_{\text{sub}}$  of 600 °C. Surface  $R_{\text{rms}}$  for the  $\beta$ -FeSi<sub>2</sub> films formed at 500 °C was evaluated to be around 10.19 nm, which increased to 13.67 nm at higher  $T_{\text{sub}}$  of 600 °C.  $\theta_{\text{CA}}$  for the formed  $\beta$ -FeSi<sub>2</sub> at 500 °C was 99.25°, which improved to 99.80° and 102.00° at the higher  $T_{\text{sub}}$  of 560 and 600 °C, respectively. It was observed that the surface for  $\beta$ -FeSi<sub>2</sub> films formed via RFMS at 500 °C, 560 °C and 600 °C presented a hydrophobic property, which revealed a potential to be applied in the field of a hydrophobic surface coating.

## 5.3 Effect of $T_{\text{ann}}$ on NC-FeSi<sub>2</sub> films formed via RFMS

NC-FeSi<sub>2</sub> films were formed via RFMS at RT and then annealed at different  $T_{\text{ann}}$  of 100 °C to 500 °C. The surface for the as-formed NC-FeSi<sub>2</sub> consisted of several crystallites with the  $R_{\text{rms}}$  of 0.94 nm. After annealing at 500 °C, the surface formed a cluster format, where the  $R_{\text{rms}}$  were increased to 5.32 nm. The wetting angle for the surface of NC-FeSi<sub>2</sub> films was identified that it was a hydrophobic with  $\theta_{\text{CA}}$  of 102.35°. After annealing, the surface for the annealed NC-FeSi<sub>2</sub> films at  $T_{\text{ann}}$  of 100 °C and 300 °C also exhibited a hydrophobic property, where the  $\theta_{\text{CA}}$  of these films was 100.30° and 93.45°, respectively. In contrast, the hydrophilic surface was found on the annealed NC-FeSi<sub>2</sub> films at  $T_{\text{ann}}$  of 500 °C, where the  $\theta_{\text{CA}}$  was 41.70°. Therefore, the results indicated that the as-formed NC-FeSi<sub>2</sub> films exhibited a suitable  $\theta_{\text{CA}}$  for hydrophobic coating, while the  $T_{\text{ann}}$  of 100 °C to 500 °C reduced the  $\theta_{\text{CA}}$  of NC-FeSi<sub>2</sub> films.

## 5.4 Effect of C-doping concentrations on $\beta$ -FeSi<sub>2</sub> films formed via RFMS

$\beta$ -FeSi<sub>2</sub> films were formed via RFMS at 560 °C of  $T_{\text{sub}}$  using the FeSi<sub>2</sub> alloy targets with the different C-doping concentrations of undoped, 0.5 at.%, 1.0 at.% and 3.0 at.%. The surface for the undoped films held a grain shape with some pinholes, where the grains were finer with an increasing of C-doping concentrations. The evaluated  $R_{\text{rms}}$  of

the undoped  $\beta$ -FeSi<sub>2</sub> films was around 15.71 nm, which was decreased to 10.59 nm after increasing the C-doping concentration to 3.0 at.%. The surface of undoped  $\beta$ -FeSi<sub>2</sub> films presented a  $\theta_{CA}$  of 108.35°. The surface for 0.5 at.% C-doped  $\beta$ -FeSi<sub>2</sub> films presented a  $\theta_{CA}$  of 107.50°, which slightly reduced to 105.45° and 103.65° at higher C-doping concentrations of 1.0 at.% and 3.0 at.%, respectively. It was noted that all wetting states for the undoped and C-doped  $\beta$ -FeSi<sub>2</sub> were hydrophobic, which were attractive for applying into hydrophobic coating.

## 5.5 Suggestions

The current research provides the following suggestions for related work in the future:

1. The other fabrication parameters such as sputtering power and sputtering pressure could be performed to research their effectiveness on the surface, wetting and mechanical properties of FeSi<sub>2</sub> films.
2. The additional annealing parameters should be performed on the FeSi<sub>2</sub> films such as annealing time and gas annealing, including a rapid annealing technique.
3. The plasma etching parameters could be performed onto FeSi<sub>2</sub> film's surface such as power, ambient and time.

## References

- [1] Leong, D., Harry, M., Reeson, K.J. and Homewood, K.P. 1997. "A silicon/iron-disilicide light-emitting diode operating at a wavelength of 1.5  $\mu\text{m}$ .", *Nature* 387 : 686-688.
- [2] Suemasu, T., Takakura, K., Li, C., Ozawa, Y., Kumagai, Y. and Hasegawa, F. 2004. "Epitaxial growth of semiconducting  $\beta\text{-FeSi}_2$  and its application to light-emitting diodes." *Thin Solid Films* 461 : 209-218.
- [3] Charoenyuenyao, P., Promros, N., Chaleawpong, R., Saekow, B., Porntheeraphat, S. and Yoshitake, T. 2020. "Influence of annealing temperature on mechanical and wetting properties of  $\beta\text{-FeSi}_2$  films built using facing-targets direct-current sputtering.", *J. Nanosci. Nanotechnol.* 20 : 621-628.
- [4] Izumi, S., Shaban, M., Promros, N., Nomoto, K. and Yoshitake, T. 2013. "Near-infrared photodetection of  $\beta\text{-FeSi}_2/\text{Si}$  heterojunction photodiodes at low temperatures.", *Appl. Phys. Lett.* 102 : 032107.
- [5] Tatar, B., Kutlu, K. and Urgan, M. 2007. "Synthesis of  $\beta\text{-FeSi}_2/\text{Si}$  heterojunctions for photovoltaic applications by unbalanced magnetron sputtering.", *Thin Solid Films* 516 : 13-16.
- [6] Promros, N., Baba, R., Takahara, M., Mostafa, T.M., Sittimart, P., Shaban, M. and Yoshitake, T. 2016. "Epitaxial growth of  $\beta\text{-FeSi}_2$  thin films on Si(111) substrates by radio frequency magnetron sputtering and their application to near-infrared photodetection.", *Jpn. J. Appl. Phys.* 55 : 06HC03.
- [7] Promros, N., Sittimart, P. and Kaenrai, W. 2016. "Investigation of electrical transport properties in heterojunctions comprised of silicon substrate and nanocrystalline iron disilicide films.", *Int. J. Nanotechnol.* 13 : 903-912.
- [8] Funasaki, S., Promros, N., Iwasaki, R., Takahara, M., Shaban, M. and Yoshitake, T. 2013. "Fabrication of mesa structural  $n$ -type nanocrystalline- $\text{FeSi}_2/p$ -type Si heterojunction photodiodes by liftoff technique combined with photolithography.", *Phys. Status Solidi C* 10 : 1785-1788.
- [9] Sittimart, P., Duangrawa, A., Onsee, P., Teakchaicum, S., Nopparuchikun, A. and Promros, N. 2018. "Interface state density and series resistance of  $n$ -type nanocrystalline  $\text{FeSi}_2/p$ -type Si heterojunctions formed by utilizing facing-

- target direct-current sputtering.”, *J. Nanosci. Nanotechnol.* 18 : 1841–1846.
- [10] Nopparuchikun, A., Promros, N., Sittimart, P., Onsee, P., Duangrawa, A., Teakchaicum, S., Nogami, T. and Yoshitake, T., 2017. “Interface-state density estimation of *n*-type nanocrystalline FeSi<sub>2</sub>/*p*-type Si heterojunctions fabricated by pulsed laser deposition.”, *Adv. Nat. Sci.: Nanosci. Nanotechnol.* 8 : 035016.
- [11] Promros, N., Yamashita, K., Izumi, S., Iwasaki, R., Shaban, M. and Yoshitake, T. 2012. “Near-infrared photodetection of *n*-type  $\beta$ -FeSi<sub>2</sub>/intrinsic Si/*p*-type Si heterojunctions at low temperatures.”, *Jpn. J. Appl. Phys.* 51 : 09MF02.
- [12] Chaleawpong, R., Promros, N., Charoenyuenyao, P., Nopparuchikun, A., Sittimart, P., Nogami, T. and Yoshitake, T. 2018. “Production of *p*-type Si/*n*-type  $\beta$ -FeSi<sub>2</sub> heterojunctions using facing-targets direct-current sputtering and evaluation of their resistance and interface state density.” *Phys. Status Solidi A* 215 : 1701022.
- [13] Promros, N., Yamashita, K., Iwasaki, R. and Yoshitake, T. 2012. “Effects of hydrogen passivation on near-infrared photodetection of *n*-type  $\beta$ -FeSi<sub>2</sub>/*p*-type Si heterojunction photodiodes.”, *Jpn. J. Appl. Phys.* 51 : 108006.
- [14] Kaenrai, W., Promros, N., Sittimart, P., Chaleawpong, R., Charoenyuenyao, P., Changcharoen, T., Nopparuchikun, A., Nogami, T. and Yoshitake, T. 2019. “Photovoltaic properties and series resistance of *p*-type Si/intrinsic Si/*n*-type nanocrystalline FeSi<sub>2</sub> heterojunctions created by utilizing facing-targets direct current sputtering.”, *J. Nanosci. Nanotechnol.* 19 : 1445–1450.
- [15] Kumar, M. 2019. “Effect of substrate temperature on surface morphology and optical properties of sputter deposited nanocrystalline nickel oxide films.”, *Mater. Res. Express* 6 : 0964.
- [16] Priyadarshini, B.G., Aich, S. and Chakraborty, M. 2014. “On the microstructure and interfacial properties of sputtered nickel thin film on Si (100).”, *Bull. Mater. Sci.* 37 : 1265-1273.
- [17] Ghorannevis, Z., Hosseinejad, M.T., Habibi, M. and Golmahdi, P. 2015. “Effect of substrate temperature on structural, morphological and optical properties of deposited Al/ZnO films.”, *J. Theor. Appl. Phys.* 9 : 33-38.
- [18] Michelini, M., Nava, F. and Galli, E. 1991. “Structural and electrical investigation of amorphous-to-crystalline transformation in iron disilicide alloy thin
- This material is reserved for educational use only, not allowed for commercial use  
Forbidden to modify the content, and cite the document when use.

- films.”, *J. Mater. Res.* 6 : 1655–1663.
- [19] Yamaguchi, K., Shimura, K., Udono, H., Sasase, M., Yamamoto, H., Shamoto, S.I. and Hojou, K. 2006. “Effect of thermal annealing on the photoluminescence of  $\beta$ -FeSi<sub>2</sub> films on Si substrate.”, *Thin Solid Films* 508 : 367–370.
- [20] Zhang, X., Qin, J., Hao, R., Wang, L., Shen, X., Yu, R., Limpanart, S., Ma, M. and Liu R. 2016. “Carbon-doped ZnO nanostructures: facile synthesis and visible light photocatalytic applications.”, *J. Phys. Chem. C* 119 : 20544–20554.
- [21] Li, X.-N., Nie, D. and Dong, C. 2002. “A comparative study on microstructures of  $\beta$ -FeSi<sub>2</sub> and carbon-doped  $\beta$ -Fe(Si,C)<sub>2</sub> films by transmission electron microscopy.”, *Nucl. Instrum. Methods Phys. Res. B* 194 : 47–53.
- [22] Dong, C., Li, X., Nie, D., Xu L. and Zhang Z. 2004. “High-quality carbon-doped  $\beta$ -type FeSi<sub>2</sub> films synthesized by ion implantation.”, *Thin Solid Films* 461 : 48–56.
- [23] Takahara, M., Tarek, M., Ryuji, B., Suguru, F., Mahmoud, S., Promros, N. and Yoshitake, T. 2015. “Electric properties of carbon-doped *n*-type  $\beta$ -FeSi<sub>2</sub>/*p*-type Si heterojunction diodes”, *JJAP Conf. Proc.* 3 : 011101.
- [24] Borisenko, V.E. 2013. *Semiconducting Silicides: Basics, Formation, Properties.* Berlin : Springer Science & Business Media.
- [25] Chen, L.J. 2004. *Silicide Technology for Integrated Circuits*, The institution of London : Engineering and Technology.
- [26] Yang, Z. and Homewood, K.P. 1996. “Effect of annealing temperature on optical and structural properties of ion-beam-synthesized semiconducting FeSi<sub>2</sub> layers.”, *J. Appl. Phys.* 79 : 4312-4317.
- [27] Shaban, M. Nomoto, K. Nakashima, K. and Yoshitake, T. 2008. “Low-temperature annealing of *n*-type  $\beta$ -FeSi<sub>2</sub>/*p*-type Si heterojunctions.”, *Jpn. J. Appl. Phys.* 47 : 3444-3446.
- [28] Olk, C.H. Yalisove, S.M. and Doll, G.L. 1995. “Defect-induced absorption-band-edge values in  $\beta$ -FeSi<sub>2</sub>.”, *Phys. Rev. B.* 52 : 1692-1698.
- [29] Shaban, M. Nakashima, K. and Yoshitake, T. 2007. “Substrate temperature dependence of photovoltaic properties of  $\beta$ -FeSi<sub>2</sub>/Si heterojunctions prepared by facing-target DC sputtering.”, *Jpn. J. Appl. Phys.* 46 : 7708-7710.

- [30] Hossain, M.Z. Mimura, T. Miura, N. and Uekusa, S.I. 2009. "Surface morphology and luminescence characterization of  $\beta$ -FeSi<sub>2</sub> thin films prepared by pulsed laser deposition.", *Appl. Surf. Sci.* 256 : 1227-1231.
- [31] Christensen, N.E. 1990. "Electronic structure of  $\beta$ -FeSi<sub>2</sub>.", *Phys. Rev. B.* 42 : 7148-7153.
- [32] Shaban, M. Nakashima, K. and Yoshitake, T. 2007. "Substrate temperature dependence of photovoltaic properties of  $\beta$ -FeSi<sub>2</sub>/Si heterojunctions prepared by facing-target DC sputtering.", *Jpn. J. Appl. Phys.* 46 : 7708-7710.
- [33] Rizzi, A. Rösen, B.N.E. Freundt, D. Dieker, C. Lüth, H. and Gerthsen, D. 1995. "Heteroepitaxy of  $\beta$ -FeSi<sub>2</sub> on Si by gas-source MBE.", *Phys. Rev. B.* 51 : 17780-17804.
- [34] Christensen, N.E. 1990. "Electronic structure of  $\beta$ -FeSi<sub>2</sub>.", *Phys. Rev. B.* 42 : 7148-7153.
- [35] Bost, M.C. and Mahan, J.E. 1985. "Optical properties of semiconducting iron disilicide thin films.", *J. Appl. Phys.* 58 : 2696-2703.
- [36] Suzuno, M. Murase, S. Koizumi, T. and Suemasu, T. 2008. "Improved Room-Temperature 1.6  $\mu$ m Electroluminescence from p-Si/ $\beta$ -FeSi<sub>2</sub>/n-Si Double Heterostructures Light-Emitting Diodes.", *Appl. Phys. Express.* 1 : 021403.
- [37] Suzuno, M. Koizumi, T. and Suemasu, T. 2009. "p-Si/ $\beta$ -FeSi<sub>2</sub>/n-Si double-heterostructure light-emitting diodes achieving 1.6  $\mu$ m electroluminescence of 0.4 mW at room temperature.", *Appl. Phys. Lett.* 94 : 213509.
- [38] Gay, J.M. Stocker, P. and Rethore, F. 1993. "X-ray scattering studies of FeSi<sub>2</sub> films epitaxially grown on Si (111).", *J. Appl. Phys.* 73 : 8169-8178.
- [39] Mahan, J.E. Thanh, V.L. Chevrier, J. Berbezier, I. Derrien, J. and Long, R.G. 1993. "Surface electron-diffraction patterns of  $\beta$ -FeSi<sub>2</sub> films epitaxially grown on silicon.", *J. Appl. Phys.* 74 : 1747-1761.
- [40] Li, X.N. Li, S.B. Nie, L.F. Li, H. Dong, C. and Jiang, X. 2010. "Preparation of amorphous Fe<sub>x</sub>Si<sub>(1-x)</sub> film using unbalanced magnetron sputtering.", *Thin Solid Films* 518 : 7390-7393.
- [41] Milosavljević, M. Wong, L. Lourenço, M. Valizadeh, R. Colligon, J. Sha, G. and Homewood, K.P. 2010. "Correlation of structural and optical properties of sputtered FeSi<sub>2</sub> thin films.", *Jpn. J Appl. Phys.* 49 : 081401.

- [42] Milosavljević, M., Shao G., Lourenço M.A., Gwilliam R.M., Homewood, K.P. Edwards, S.P. Valizadeh, R. and Colligon, J.S. 2005. "Transition from amorphous to crystalline beta phase in co-sputtered FeSi<sub>2</sub> films as a function of temperature.", J. Appl. Phys. 98 : 123506.
- [43] Shaban, M. Kondo, H. Nakashima, K. and Yoshitake, T. 2008. "Electrical and photovoltaic properties of n-type nanocrystalline-FeSi<sub>2</sub>/p-type Si heterojunctions prepared by facing-targets direct-current sputtering at room temperature.", Jpn. J. Appl. Phys. 47 : 5420-5422.
- [44] Yoshitake, T. Yatabe, M. Itakura, M. Kuwano, N. Tomokiyo, Y. and Nagayama, K. 2003. "Semiconducting nanocrystalline iron disilicide thin films prepared by pulsed-laser ablation.", Appl. Phys. Lett. 83 : 3057-3059.
- [45] Promros, N. Yamashita, K. Li, C. Kawai, K. Shaban, M., Okajima, T., and Yoshitake, T. 2012. "n-Type nanocrystalline FeSi<sub>2</sub>/intrinsic Si/p-type Si heterojunction photodiodes fabricated by facing-target direct-current sputtering.", Jpn. J. Appl. Phys. 51 : 021301.
- [46] Takarabe, K. Doi, H. Mori, Y. Fukui, K. Shim, Y. Yamamoto, N. Yoshitake, T., and Nagayama, K. 2006. "Optical properties of nanocrystalline FeSi<sub>2</sub> and the effects of hydrogenation.", Appl. Phys. Lett. 88 : 061911.
- [47] Shaban, M. Kawai, K. Promros, N. and Yoshitake, T. 2010. "n-Type nanocrystalline-FeSi<sub>2</sub>/p-Type Si heterojunction photodiodes prepared at room temperature.", IEEE Electron Device Lett. 31 : 1428-1430.
- [48] Nakamura, S. Aoki, T. Kittaka, T. Hakamata, R. Tabuchi, H. Kunitsugu, S. and Takarabe, K.I. 2007. "Facing target sputtered iron-silicide thin film.", Thin Solid Films 515 : 8205-8209.
- [49] Yoshitake, T., Inokuchi, Y., Yuri, A. and Nagayama, K. 2006. "Direct epitaxial growth of semiconducting  $\beta$ -FeSi<sub>2</sub> thin films on Si(111) by facing targets direct-current sputtering.", Appl. Phys. Lett. 88 : 182104.
- [50] Kelly, P.J and Arnell, R.D. 2000. "Magnetron sputtering: a review of recent developments and applications.", Vacuum 56 : 159-172.
- [51] Hashmi, S. 2015. "Handbook of manufacturing engineering and technology.", London : Springer-Verlag.
- [52] Gudmundsson, J.T. 2020. "Physics and technology of magnetron sputtering discharges.", Plasma Sources Sci. Technol. 29 : 113001.

- [53] Wasa, K., Kanno, I. and Kotera H. 2012. "Handbook of sputter deposition technology fundamentals and applications for functional thin films, nanomaterials, and MEMS, 2<sup>nd</sup> edition.", Waltham : William Andrew (Imprint of Elsevier).
- [54] Swann, S. 1988. "Magnetron sputtering", Phys. Technol. 19 : 67-75.
- [55] Mattox, D.M. 2010. "Handbook of physical vapor deposition (PVD) processing.", Burlington : William Andrew (Imprint of Elsevier).
- [56] Panjan, M. 2019. "Self-organizing plasma behavior in RF magnetron sputtering discharges.", J. Appl. Phys. 125 : 203303.
- [57] Lin, C., Sun, D. C., Ming, S. L., Jiang, E. Y., and Liu, Y. G. 1996. "Magnetron facing target sputtering system for fabricating single-crystal films.", Thin Solid Films 279 : 49-52.
- [58] Maurya, D. K., Sardarinejad, A. and Alameh, K. 2014. "Recent developments in RF Magnetron sputtered thin films for pH sensing applications-an overview.", Coatings 4 : 756-771.
- [59] Chapman, B. 1980. "Glow discharge processes sputtering and plasma etching.", New Jersey : John Wiley & Sons.
- [60] Shaban, M., Nomoto, K., Izumi, S. and Yoshitake, T. 2009. "Characterization of near-infrared *n*-type  $\beta$ -FeSi<sub>2</sub>/*p*-type Si heterojunction photodiodes at room temperature.", Appl. Phys. Lett. 94 : 222113.
- [61] Kolesnikov, N. and Borisenko, E. 2012. "Modern aspects of bulk crystal and thin film preparation.", Rijeka : InTech.
- [62] Seshan K. and Schepis D. 2018. "Handbook of Thin Film Deposition, 4<sup>th</sup> edition" Cambridge : William Andrew (Imprint of Elsevier).
- [63] Bunaciu, A.A., Udriștioiu, E.G., and Aboul-Enein, H.Y. 2015. "X-ray diffraction: instrumentation and applications.", Crit. Rev. Anal. Chem. 45 : 289-299.
- [64] Downes, A. and Elfick A. 2010. "Raman spectroscopy and related techniques in biomedicine.", Sensors 10 : 1871-1889.
- [65] Joy, D.C., Bradbury, S. and Ford, B.J. 2019. **Scanning electron microscope.** [Online]. Available : <https://www.britannica.com/technology/scanning-electron-microscope>.
- [66] Zeng, C., Vitale-Sullivan, C. and Ma, X. 2017. "In situ atomic force microscopy studies on nucleation and self-assembly of biogenic and bio-inspired

- materials.”, *Minerals* 7 : 158.
- [67] Drelich, J., Chibowski, E., Meng, D.D. and Terpilowski, K. 2011. “Hydrophilic and superhydrophilic surfaces and materials.”, *Soft. Matter.* 7 : 9804-9828.
- [68] Krasowska, M., Zawala, J. and Malysa, K. 2009. “Air at hydrophobic surfaces and kinetics of three phase contact formation.”, *Adv. Colloid Interface Sci.* 147–148 : 155-169.
- [69] Mohamed, A.M.A, Abdullah, A.M. and Younan, N.A. 2015. “Corrosion behavior of superhydrophobic surfaces : A review.”, *Arab. J. Chem.* 8 : 749-765.
- [70] Zhai, L., Cebeci, F.C., Cohen, R.E. and Rubner, M.F. 2004. “Stable superhydrophobic coatings from polyelectrolyte multilayers.”, *Nano Lett.* 4 : 1349-1353.
- [71] Sun, X., Li, L., Guo, Y., Zhao, H., Zhang, S., Yu, Y., Wu, D., Liu, H., Yu, M., Shi, D., Liu, Z., Zhou, M., Ren, L. and Fu, L. 2018. “Influences of organic component on mechanical property of cortical bone with different water content by nanoindentation.”, *AIP Advances* 8 : 035003.
- [72] Yang, L. Zhang, M. Shi, S. Lv, J. Song, X. He, G. and Sun, Z. 2014. “Effect of annealing temperature on wettability of TiO<sub>2</sub> nanotube array films.”, *Nanoscale Research Letters* 9 : 621-1-621-6.
- [73] Terai, Y., Yamaguchi, H., Tsukamoto, H., Murakoso, N. and Hoshida, H. 2018. “Polarized Raman spectra of  $\beta$ -FeSi<sub>2</sub> epitaxial film grown by molecular beam epitaxy.”, *AIP Adv.* 8 : 105028.
- [74] Lefki, K., Muret, P., Bustarret, E., Boutarek, N., Madar, R., Chevrier, J., Derrien, J. and Brunel, M. 1991. “Infrared and Raman characterization of beta iron silicide.”, *Solid State Commun.* 80 : 791-795.
- [75] Maeda, Y., Umezawa, K., Hayashi, Y. and Miyake, K. 2001. “Raman spectroscopic study of ion-beam synthesized polycrystalline  $\beta$ -FeSi<sub>2</sub> on Si(100).”, *Thin Solid Films* 381 : 219-224.
- [76] Cassie, A.B.D. and Baxter, S. 1944. “Wettability of porous surfaces.”, *Trans. Faraday Soc.* 40 : 546-551.
- [77] Tian, Y., Su, B. and Jiang, L. 2014. “Interfacial material system exhibiting superwettability.”, *Adv. Mater.* 26 : 6872-6897.
- [78] Erbil, H.Y. and Cansoy, C.E. 2009. “Range of applicability of the Wenzel and Cassie-Baxter equations for superhydrophobic surfaces.”, *Langmuir* 25 : 14135-

14145.

- [79] Cha, S.C., Her, E.K., Ko, T.J., Kim, S.J., Roh, H., Lee, K.R., Oh, K.H. and Moon, M.W. 2013. "Thermal stability of superhydrophobic, nanostructured surfaces.", *J. Colloid Interface Sci.* 391 : 152-157.
- [80] Lafuma, A. and Quéré, D. 2009. "Superhydrophobic states.", *Nat. Mater.* 2 : 457-460.
- [81] Quéré, D. 2008 "Wetting and roughness.", *Ann. Rev. Mater. Res.* 38 : 71-99.
- [82] Schiøtz, J., Vegge, T., Di Tolla, F.D. and Jacobsen, K.W. 1999. "Atomic-scale simulations of the mechanical deformation of nanocrystalline metals.", *Phys. Rev. B* 60 : 11971-11983.
- [83] Li, X., Nie, D., Dong, C., Xu, L. and Zhang, Z. 2004. "Structure characterization and photon absorption analysis of carbon-doped  $\beta$ -FeSi<sub>2</sub> film.", *J. Vac. Sci. Technol. A* 22 : 2473-2478.
- [84] Van Swygenhoven, H. 2002. "Grain boundaries and dislocations.", *Science* 296 : 66-67.
- [85] Chen, J., Wang, W., Qian, L.H. and Lu, K. 2003. "Critical shear stress for onset of plasticity in a nanocrystalline Cu determined by using nanoindentation.", *Scr. Mater.* 49 : 645-650.
- [86] Liu, H.F., Huang, A. and Chi, D.Z. 2011. "Anomalous temperature-dependency of phonon line widths probed by Raman scattering from  $\beta$ -FeSi<sub>2</sub> thin films.", *J. Appl. Phys.* 109 : 083538.
- [87] Terai, Y., Haruki, Y., Hiroaki, T., Tetsu, H. and Takahiko, H. 2015. "Effects of lattice deformations on Raman spectra in  $\beta$ -FeSi<sub>2</sub> epitaxial films.", *JJAP Conf. Proc.* 3 : 011109.
- [88] Charoenyuenyao, P., Promros, N., Chaleawpong, R., Borwornpornmetee, N., Sittisart, P., Tanaka, Y. and Yoshitake, T. 2020. "Impact of annealing temperature and carbon doping on the wetting and surface morphology of semiconducting iron disilicide formed via radio frequency magnetron sputtering.", *Thin Solid Films* 709 : 138248.
- [89] Muslim, N., Soon, Y.W., Lim, C.M., Voo and N.Y. 2016. "Properties of nickel films growth by radio frequency magnetron sputtering at elevated substrate temperatures.", *Thin Solid Films* 612 : 82-86.
- [90] Murakami, D., Jinnai, H. and Takahara, A. 2014. "Wetting transition from the

Cassie-Baxter state to the Wenzel state on textured polymer surfaces.”, *Langmuir* 30 : 2061-2067.

- [91] Wu, B., Zhou, M., Li, J., Ye, X., Li, G. and Cai, L. 2009. “Superhydrophobic surfaces fabricated by microstructuring of stainless steel using a femtosecond laser.”, *Appl. Surf. Sci.* 256 : 61-66.
- [92] Ng, Z.N., Chan, K.Y. and Tohsophon, T. 2012. “Effects of annealing temperature on ZnO and AZO films prepared by sol-gel technique.”, *Appl. Surf. Sci.* 258 : 9604-9609.
- [93] Li, X., Nie, D., Dong, C., Xu, L. and Zhang, Z. 2004. “Structure characterization and photon absorption analysis of carbon-doped  $\beta$ -FeSi<sub>2</sub> film.”, *J. Vac. Sci. Technol. A* 22 : 2473-2478.
- [94] Ren, W., Ai, Z., Jia, F., Zhang, L., Fan, X. and Zou, Z. 2007. “Low temperature preparation and visible light photocatalytic activity of mesoporous carbon-doped crystalline TiO<sub>2</sub>.”, *Appl. Catal. B* 69 : 138-144.
- [95] Perumal, A., Ko, H.-S. and Shin S.-C. 2003. “Perpendicular thin films of carbon-doped FePt for ultrahigh-density magnetic recording media.”, *IEEE Trans. Magn.* 39 : 2320-2322.
- [96] Cho, Y.C., Cha, S.-Y., Shin, J.M., Park, J.H., Park, S.E., Cho, C.R., Park, S., Pak, H.K., Jeong, S.-Y. and Lim. A.-R. 2009. “The conversion of wettability in transparent conducting Al-doped ZnO thin film.”, *Solid State Commun.* 149 : 609-611.



This material is reserved for educational use only, not allowed for commercial use.  
Forbidden to modify the content, and cite the document when use.

# Author Biography

**Name** Mr. Peerasil Charoenyuenyao  
**Date of Birth** March 4, 1994  
**Address** Department of Physics, School of Science,  
King Mongkut's Institute of Technology Ladkrabang, Thailand  
**Education** (2016) Bachelor of Science in Physics GPA 2.33  
King Mongkut's Institute of Technology Ladkrabang  
(2018) Master of Science in Physics GPA 3.50  
King Mongkut's Institute of Technology Ladkrabang

## Academic Publications (as 1<sup>st</sup> and Co-author)

- [1] **Peerasil Charoenyuenyao**, Nathaporn Promros, Rawiwan Chaleawpong, Nattakorn Borwornpornmetee, Pattarapol Sittisart, Yuki Tanaka, Tsuyoshi Yoshitake, Wettability, Morphological and Wetting Properties of Semiconducting Beta and Nanocrystalline Iron Disilicide Formed via Radio Frequency Magnetron Sputtering, Thin Solid Films, Vol. 709 (2020) Article No. 138248. (Impact factor 1.748) Indexed in Web of science.
- [2] **Peerasil Charoenyuenyao**, Nathaporn Promros, Rawiwan Chaleawpong, Pitoon Noymaliwan, Nattakorn Borwornpornmetee, Surachart Kamoldilok, Supanit Porntheeraphat, Bunpot Saekow, Tanapoj Chaikereee, Benjarong Samransuksamer, Peerapong Nuchuay, Chanunthorn Chananonnawathorn, Saksorn Limwichean, Mati Horprathum, Pitak Eiamchai, Viyapol Patthanasettakul, Influence of an Annealing Temperature in a Vacuum Atmosphere on the Physical Properties of Indium Tin Oxide Nanorod Films, Journal of Nanoscience and Nanotechnology, Vol. 20 (2020) 5006-5013. (Impact factor 1.483) Indexed in Web of science.
- [3] **Peerasil Charoenyuenyao**, Nathaporn Promros, Rawiwan Chaleawpong, Nattakorn Borwornpornmetee, Pattarapol Sittisart, Yuki Tanaka, Tsuyoshi Yoshitake, Wettability, Surface Morphology and Structural Properties of  $\beta$ -FeSi<sub>2</sub> Films Manufactured through Usage of Radio-Frequency Magnetron Sputtering, Journal of Nanoscience and Nanotechnology, Vol. 20 (2020) 5075-5081. (Impact

- factor 1.483) Indexed in Web of science.
- [4] **Peerasil Charoenyuenyao**, Nathaporn Promros, Rawiwan Chaleawpong, Bunpot Saekow, Supanit Porntheeraphat, and Tsuyoshi Yoshitake, Influence of Annealing Temperature on Mechanical and Wetting Properties of  $\beta$ -FeSi<sub>2</sub> Films Built Using Facing-Targets Direct-Current Sputtering, *Journal of Nanoscience and Nanotechnology*, Vol. 20 (2020) 621-628. (Impact factor 1.483) Indexed in Web of science.
- [5] Rawiwan Chaleawpong, Nathaporn Promros, **Peerasil Charoenyuenyao**, Phongsaphak Sittimart, Pattarapol Sittisart, Nattakorn Borwornpornmetee, Yuki Tanaka, Tsuyoshi Yoshitake, Photovoltaic, Capacitance-Voltage, Conductance-Voltage, and Electrical Impedance Characteristics of p-Type Silicon/Intrinsic-Silicon/n-Type Semiconducting Iron Disilicide Heterostructures Built via Facing Target Direct-Current Sputtering, *Thin Solid Films*, Vol. 709 (2020) Article No. 138229. (Impact factor 1.748) Indexed in Web of science.
- [6] Rawiwan Chaleawpong, Nathaporn Promros, Abdelrahman Zkria, **Peerasil Charoenyuenyao**, Eslam Abubakr, Tsuyoshi Yoshitake, Diode parameters and ultraviolet light detection characteristics of n-type silicon/p-type nanocrystalline diamond heterojunctions at different temperatures, *Thin Solid Films*, Vol. 709 (2020) Article No. 138222. (Impact factor 1.748) Indexed in Web of science.
- [7] Rawiwan Chaleawpong, Nathaporn Promros, **Peerasil Charoenyuenyao**, Phongsaphak Sittimart, Satoshi Takeichi, Yuki Katamune, Abdelrahman Zkria, Eslam Abubakr, Mohamed Egiza, Ali M. Ali, and Tsuyoshi Yoshitake, Diode Parameters and Equivalent Electrical Circuit Model of n-Type Silicon/B-Doped p-Type Ultrananocrystalline Diamond Heterojunctions Manufactured Through Coaxial Arc Plasma Deposition, *Journal of Nanoscience and Nanotechnology*, Vol. 20 (2020) 4884-4891. (Impact factor 1.483) Indexed in Web of science.
- [8] Pattarapol Sittisart, Nathaporn Promros, Rawiwan Chaleawpong, **Peerasil Charoenyuenyao**, Nattakorn Borwornpornmetee, Yuki Tanaka, Tsuyoshi Yoshitake, Light Detection and Carrier Transportation Mechanism in p-Type Si/n-Type Nanocrystalline FeSi<sub>2</sub> Heterojunctions produced via Radio-Frequency Magnetron Sputtering, *Journal of Nanoscience and Nanotechnology*, Vol. 20 (2020) 5082-5088. (Impact factor 1.483) Indexed in Web of science.
- [9] Rawiwan Chaleawpong, Nathaporn Promros, **Peerasil Charoenyuenyao**, Kenji

Hanada, Li Chen, and Tsuyoshi Yoshitake, Extraction of  $I-V$ ,  $G-V-f$  and  $C-V-f$  Characteristics for p-Type Silicon/Intrinsic Ultrananocrystalline Diamond/n-Type Nanocrystalline Iron Disilicide Heterojunction Photodiodes, *Journal of Nanoscience and Nanotechnology*, Vol. 20 (2020) 433-441. (Impact factor 1.483) Indexed in Web of science.

- [10] Rawiwan Chaleawpong, Nathaporn Promros, **Peerasil Charoenyuenyao**, Takanori Hanada, Shinya Ohmagari, and Tsuyoshi Yoshitake, Temperature Dependence of Alternating Current Impedance in n-Type Si/B-doped p-Type Ultrananocrystalline Diamond Heterojunctions produced through Pulsed Laser Deposition, *Journal of Nanoscience and Nanotechnology*, Vol. 20 (2020) 331-337. (Impact factor 1.483) Indexed in Web of science.
- [11] **Peerasil Charoenyuenyao**, Nathaporn Promros, Rawiwan Chaleawpong, Bunpot Saekow, Supanit Porntheeraphat, and Tsuyoshi Yoshitake, Effect of Annealing on Surface Morphology and Wettability of NC-FeSi<sub>2</sub> Films Produced via Facing-Target Direct-Current Sputtering, *Journal of Nanoscience and Nanotechnology*, Vol. 19 (2019) 6834-6840. (Impact factor 1.483) Indexed in Web of science.
- [12] Rawiwan Chaleawpong, Nathaporn Promros, **Peerasil Charoenyuenyao**, Adison Nopparuchikun, Takanori Hanada, Shinya Ohmagari, and Tsuyoshi Yoshitake,  $C-V-f$ ,  $G-V-f$  and  $Z''-Z'$  Characteristics of n-Type Si/B-Doped p-Type Ultrananocrystalline Diamond Heterojunctions Formed via Pulsed Laser Deposition, *Journal of Nanoscience and Nanotechnology*, Vol. 19 (2019) 6812-6820. (Impact factor 1.483) Indexed in Web of science.
- [13] Nathaporn Promros, Pitoon Noymaliwan, **Peerasil Charoenyuenyao**, Rawiwan Chaleawpong, Supanit Porntheeraphat, Bunpot Saekow, Tanapoj Chaikereee, Benjarong Samransuksamer, Peerapong Nuchuay, Chanunthorn Chananonnawathorn, Saksorn Limwichean, Mati Horprathum, Pitak Eiamchai, and Viyapol Patthanasettakul, Study of Annealing Influence on Basic Properties of Indium Tin Oxide Nanorod Films Deposited Using Glancing Angle Ion-Assisted Electron Beam Evaporation, *Journal of Nanoscience and Nanotechnology*, Vol. 19 (2019) 1432-1438. (Impact factor 1.483) Indexed in Web of science.
- [14] Rawiwan Chaleawpong, Nathaporn Promros, **Peerasil Charoenyuenyao**, Takanori Hanada, Shinya Ohmagari, Abdelrahman Zkria, and Tsuyoshi Yoshitake, Junction parameters of boron-doped p-type ultrananocrystalline

- diamond/hydrogenated amorphous carbon composite/n-type silicon heterojunctions formed by pulsed laser deposition, *Journal of Nanoscience and Nanotechnology*, *Journal of Nanoscience and Nanotechnology*, Vol. 19 (2019) 1567-1573. (Impact factor 1.483) Indexed in Web of science.
- [15] Weerasaruth Kaenrai, Nathaporn Promros, Phongsaphak Sittimart, Rawiwan Chaleawpong, **Peerasil Charoenyuenyao**, Thanachai Changcharoen, Adison Nopparuchikun, Tomohiro Nogami, and Tsuyoshi Yoshitake, Photovoltaic Properties and Series Resistance of p-Type Si/Intrinsic Si/n-Type Nanocrystalline FeSi<sub>2</sub> Heterojunctions Created by Utilizing Facing-Targets Direct-Current Sputtering, *Journal of Nanoscience and Nanotechnology*, *Journal of Nanoscience and Nanotechnology*, Vol. 19 (2019) 1445-1450. (Impact factor 1.483) Indexed in Web of science.
- [16] **Peerasil Charoenyuenyao**, Nathaporn Promros, Rawiwan Chaleawpong, and Tsuyoshi Yoshitake, Surface Morphology and Wettability for Thin Films of Beta-Iron Disilicide Produced through Direct-Current Sputtering Utilizing a Pair of Facing Targets, *MATEC Web of Conferences* Vol. 192, (2018) 01054. Indexed in SCOPUS.
- [17] Rawiwan Chaleawpong, Nathaporn Promros, **Peerasil Charoenyuenyao**, Adison Nopparuchikun, Phongsaphak Sittimart, Tomohiro Nogami, and Tsuyoshi Yoshitake, Production of p-Type Si/n-Type  $\beta$ -FeSi<sub>2</sub> Heterojunctions Using Facing-Targets Direct-Current Sputtering and Evaluation of Their Resistance and Interface State Density, *Phys. Status Solidi A*, Vol. 215 (2018) Article No. 1701022. (Impact factor 1.795) Indexed in Web of science.
- [18] Nathaporn Promros, Pitoon Noy maliwan, **Peerasil Charoenyuenyao**, Rawiwan Chaleawpong, Supanit Porntheeraphat, Bunpot Saekow, Tanapoj Chaikereee, Benjarong Samransuksamer, Peerapong Nuchuay, Chanunthorn Chananonawathorn, Saksorn Limwichean, Mati Horprathum, Pitak Eiamchai, and Viyapol Patthanasettakul, Impact of Annealing Temperature on the Physical Properties of Indium Tin Oxide Nanorod Films Grown by Glancing-Angle Ion-Assisted Electron-Beam Evaporation, (1<sup>st</sup> MRS Thailand International Conference, (2017) 382-387.

### Academic Awards

Years	Awards	Organizations
2019	Best Poster Award	The 5th International Conference on Advanced Electromaterials: <b>ICAE 2019</b> Ramada Plaza Jeju Hotel, Jeju, Korea, November 5-8, 2019
2019	Best Poster Award	The 30th International Conference on Molecular Electronics and Devices: <b>30th IC ME&amp;D</b> Busan, Korea May 9-10,2019
2018	Best Poster Paper Award	The 5th International Conference on Electronic Materials and Nanotechnology for Green Environment: <b>ENGE 2018</b> Ramada Plaza Jeju Hotel, Jeju, Korea, November 11-14, 2018
2018	The Best Poster Award	The 7th International Conference on Microelectronics and Plasma Technology: <b>ICMAP 2018</b> Songdo Convensia, Incheon, Korea July 24-28, 2018